

Characterisation of three-phase fluid distributions in a porous rock using micro computed tomography

Author:

Feali, Mostafa

Publication Date:

2013

DOI:

<https://doi.org/10.26190/unsworks/16514>

License:

<https://creativecommons.org/licenses/by-nc-nd/3.0/au/>

Link to license to see what you are allowed to do with this resource.

Downloaded from <http://hdl.handle.net/1959.4/53078> in <https://unsworks.unsw.edu.au> on 2024-04-27



UNSW
THE UNIVERSITY OF NEW SOUTH WALES

Characterisation of Three-Phase Fluid Distributions in a Porous Rock Using Micro Computed Tomography

Mostafa Feali

BSc (Chemical Engineering)

MSc (Reservoir Engineering)

A thesis submitted for the degree of Doctor of Philosophy in Petroleum Engineering

Supervisor: Dr. Yildiray Cinar

Co-Supervisor: Professor Val Pinczewski

School of Petroleum Engineering
The University of New South Wales
March 2013

ORIGINALITY STATEMENT

I hereby declare that this submission is my own work and to the best of my knowledge it contains no materials previously published or written by another person, or substantial proportions of material which have been accepted for the award of any other degree or diploma at UNSW or any other educational institution, except where due acknowledgement is made in the thesis. Any contribution made to the research by others, with whom I have worked at UNSW or elsewhere, is explicitly acknowledged in the thesis. I also declare that the intellectual content of this thesis is the product of my own work, except to the extent that assistance from others in the project's design and conception or in style, presentation and linguistic expression is acknowledged.'

Mostafa Feali

March 2013

COPYRIGHT STATEMENT

'I hereby grant the University of New South Wales or its agents the right to archive and to make available my thesis or dissertation in whole or part in the University libraries in all forms of media, now or here after known, subject to the provisions of the Copyright Act 1968. I retain all proprietary rights, such as patent rights. I also retain the right to use in future works (such as articles or books) all or part of this thesis or dissertation.

I also authorise University Microfilms to use the 350 word abstract of my thesis in Dissertation Abstract International (this is applicable to doctoral theses only).

I have either used no substantial portions of copyright material in my thesis or I have obtained permission to use copyright material; where permission has not been granted I have applied/will apply for a partial restriction of the digital copy of my thesis or dissertation.'

Signed 

Date 2013, 12, 16

AUTHENTICITY STATEMENT

'I certify that the Library deposit digital copy is a direct equivalent of the final officially approved version of my thesis. No emendation of content has occurred and if there are any minor variations in formatting, they are the result of the conversion to digital format.'

Signed 

Date 2013, 12, 16

PLEASE TYPE

THE UNIVERSITY OF NEW SOUTH WALES
Thesis/Dissertation Sheet

Surname or Family name: **Feali**

First name: **Mostafa**

Other name/s:

Abbreviation for degree as given in the University calendar: **PHD**

School: **Petroleum School**

Faculty: **Engineering**

Title: **Characterisation of Three-Phase Fluid Distributions in a Porous Rock Using Micro Computed Tomography**

Abstract 350 words maximum: (PLEASE TYPE)

Understanding the physics of three-phase (gas, oil and water) displacements in porous rocks is crucial for predicting petroleum recovery and the migration of non-aqueous phase liquids contaminated in soils. Topological properties of porous rocks and interactions of fluids within these rocks control how three fluid phases flow together in pore space. The effort made in the 1990s using 2D glass micro models of simplistic porous system helped significantly understand the physics and mechanisms of three-phase fluid interactions in porous media. However, no study has been reported so far to examine the effect of the three-dimensional topological properties of a porous rock on characteristics of three-phase fluids.

This thesis presents a study that combines the 3D imaging and 3D computational analysis to characterise qualitatively and quantitatively the three-phase fluids (oil, water and gas) at different spreading conditions in a porous rock. It attempts to answer whether or not the intermediate oil phase in a gas-oil-water system is spatially connected within an actual porous rock through oil films. An innovative experimental approach was used to visualise 3D distributions of three-phase (gas, oil and water) using a high resolution micro-CT. A methodology used to align and subtract two sets of tomograms of the same rock being dry and partially saturated is presented. This methodology allows extracting and delineating 3D information of oil, water and gas in a porous rock which provides a qualitative description of the configurations and distributions of three phases regardless of the uncertainty associated to pores topology.

A sophisticated segmentation algorithm was used to perform a quantitative analysis of the gas-oil-water distributions obtained from the micro-CT images. The spatial connectivity of each of the phases at the end of the tertiary gas flooding was analysed and discussed using quantitative measures obtained from the Euler characteristics method. This study provides a confirmation of the presence and continuity of oil spreading films for positive spreading systems in real porous media and the absence of spreading films for negative spreading systems.

Declaration relating to disposition of project thesis/dissertation

I hereby grant to the University of New South Wales or its agents the right to archive and to make available my thesis or dissertation in whole or in part in the University libraries in all forms of media, now or here after known, subject to the provisions of the Copyright Act 1968. I retain all property rights, such as patent rights. I also retain the right to use in future works (such as articles or books) all or part of this thesis or dissertation.

I also authorise University Microfilms to use the 350 word abstract of my thesis in Dissertation Abstracts International (this is applicable to doctoral theses only).


Signature


Witness

2013, 12, 16
Date

The University recognises that there may be exceptional circumstances requiring restrictions on copying or conditions on use. Requests for restriction for a period of up to 2 years must be made in writing. Requests for a longer period of restriction may be considered in exceptional circumstances and require the approval of the Dean of Graduate Research.

FOR OFFICE USE ONLY

Date of completion of requirements for Award:

THIS SHEET IS TO BE GLUED TO THE INSIDE FRONT COVER OF THE THESIS

Publications from This Thesis:

- **M. Feali, W.V. Pinczewski, Y. Cinar, C.H. Arns, J.Y. ArnsM.Turner, T. Senden N. Francois and M. Knackstedt:** “Qualitative and Quantitative Analyses of the Three-Phase Distribution of Oil, Water and Gas in Bentheimer Sandstone by Use of Micro-CT Imaging”- Published in SPE Reservoir Evaluation and Engineering, Vol.15(4), 706-711.
- **M. Feali, W.V. Pinczewski, Y. Cinar, C.H. Arns, J.Y. ArnsM.Turner, T. Senden N. Francois and M. Knackstedt:** “Qualitative and Quantitative Analysis of Three-Phase Distribution of Oil, Water and Gas in Bentheimer Sandstone Using Micro-CT Imaging”- proceeding at the Society of Petroleum Engineers (SPE) Latin America and Caribbean Petroleum Engineering Conference, 16-18 April 2012, Mexico City, Mexico, SPE-151609.

Acknowledgments

Pursuing this Ph.D. has been a uniquely challenging and equally enjoyable experience. At times I could compare it to navigating through a crowded city with no signposts and having to singlehandedly bear the bitterness, hardship and frustration of the never-ending journey. I was quite fortunate to have loving support, trust and encouragement from some outstanding people. When I reached my destination and tasted the fruits of my accomplishment, I knew this was a real testimony to the attentive support I had received. While words alone do not adequately convey my heartfelt gratitude to those who have supported me in this path, I have dedicated this section to acknowledging my appreciation and admiration.

I am very thankful of my supervisor Dr. Yildiray Cinar and Professor Val Pinczewski who without their trust, guidance, dedication and inspiration, this research would simply not have been possible. They were increasingly patient and understanding of my mistakes and showed me new insights. Special thanks to Associate Professor Christoph Arns for his assistance in this project and Nino Zajackowski, our laboratory supervisor who was always tremendously helpful to me no matter the circumstances of the task.

I am very appreciative of Professor Mark Knacktedt, Associate Professor Tim Senden, Dr. Adrian Sheppard, Dr. Michael Turner, Dr. Nicolas Francois, Dr. Andrew Knigston, Dr. Mohammad Saadatfar and Jill Middleton from the Department of Applied Mathematics at the Australian National University. They generously offered their time and assisted me in conducting X-ray imaging experiments and computational analysis. I am grateful of all my friends from the School of Petroleum Engineering at the University of New South Wales, who have not only provided me with many valuable discussions for my

research but who also sustained our motivation and lively energy through some particularly challenging times. Saeed Norouzi, Ahmad Khalili, Jafar Qajar, EhsanAzizi, Amin Gholami, Fatemeh Kamali, Mohammad Al-hamdan, Sefer Yenici, Furqan Hussain, Tareq Alghamdi, Mohammad Fahadand Nurul Ismail. Special thanks to my good mate, Naeem Hashemi who assisted with some grammatical revisions. I am also appreciative of my friends back home, Hesam Darani, Mohsen Dabiri, Kambiz Kouhi, Belal Heidari, Vahid Feali, Saeed Rouzbahani who have always been by my side all these years through the best and some of the less favourable times. I am reminded now that “truly great friends are hard to find, difficult to leave and impossible to forget”.

I am profoundly thankful of my dear wife, Solmaz. She has shown me endless support, encouragement, unwavering love and enduring patience. Her sense of humour has brought me happiness and she has managed to solve all concerns and challenges. Her acceptance of my occasional brash moods is a testament in itself of her unyielding devotion and love.

My heartfelt thanks to my dearest Mum and Dad, Maryam and Heshmat, for everything they have done for me. Their firm and kind-heartedness has made me steadfast and never let me yield to difficulty. They have always let me know that they are proud of me, which has motivated me to always work harder and never feel tired. Without their endless support, love, encouragement and sacrifices I have finished well before I have started. I deeply appreciate their understanding and emotional support. Thank you for being there for me. I give my deepest thanks to my younger sister, Parisa for her limitless love, support, kindness and understanding. My life has been much happier and enjoyable having you beside me. Special thanks are to my dearest grandma, Malek, for her love and prayers.

“This work is dedicated to my family who have always given me love”

Abstract

Understanding the physics of three-phase (gas, oil and water) displacements in porous rocks is crucial for predicting petroleum recovery and the migration of non-aqueous phase liquids contaminated in soils. Topological properties of porous rocks and interactions of fluids within these rocks control how three fluid phases flow together in pore space. The effort made in the 1990s using 2D glass micro models of simplistic porous system helped significantly understand the physics and mechanisms of three-phase fluid interactions in porous media. However, no study has been reported so far to examine the effect of the three-dimensional topological properties of a porous rock on characteristics of three-phase fluids.

This thesis presents a study that combines the 3D imaging and 3D computational analysis to characterise qualitatively and quantitatively the three-phase fluids (oil, water and gas) at different spreading conditions in a porous rock. It attempts to answer whether or not the intermediate oil phase in a gas-oil-water system is spatially connected within an actual porous rock through oil films. An innovative experimental approach was used to visualise 3D distributions of three-phase (gas, oil and water) using a high resolution micro-CT. A methodology used to align and subtract two sets of tomograms of the same rock being dry and partially saturated is presented. This methodology allows extracting and delineating 3D information of oil, water and gas in a porous rock which provides a qualitative description of the configurations and distributions of three phases regardless of the uncertainty associated to pores topology.

A sophisticated segmentation algorithm was used to perform a quantitative analysis of the gas-oil-water distributions obtained from the micro-CT images. The spatial connectivity of each of the phases at the end of the tertiary gas flooding was analysed and discussed using quantitative measures obtained from the Euler characteristics method. This study provides a confirmation of the presence and continuity of oil spreading films for positive spreading systems in real porous media and the absence of spreading films for negative spreading systems.

Table of Contents

Publications From This Thesis:	i
Acknowledgments	ii
Abstract	iv
List of Figures	vii
List of Tables	xiii
Chapter 1 Introduction	1
Chapter 2 Literature Review	5
2.1. Three-Phase Flow in Porous Media.....	6
2.2. Spreading Behaviour in Porous Media	10
2.3. Oil Films in Real Porous Media.....	15
Chapter 3 Experimental and Computational Methodologies	21
3.1. Workflow	22
3.2. Experimental Methodology.....	24
3.2.1. Porous Medium	24
3.2.2. Three-phase Fluids	29
3.2.3. Core Flooding	39
3.2.4. X-ray Micro-CT Computed Tomography	41
3.3. Micro-CT Image Analysis.....	47
3.3.1. Image Enhancement and Optimisation	47
3.3.2. Image Registration.....	53
3.3.3. Image Subtraction and Renormalisation	57
3.3.4. Image Segmentation.....	64
3.3.5. Porosity, Fluid Saturation and Distribution.....	80
3.4. Spatial Characterisation of Distribution and Connectivity	80
3.4.1. Generation of Pore-scale Network of Three-phase Fluids	80

3.4.2.	Spatial Connectivity Using the Euler Characteristic Method.....	83
3.5.	Three-dimensional Visualisation.....	83
Chapter 4	Results and Discussion	86
4.1.	Analysis of Films for Positive and Negative Systems.....	93
4.1.1.	Spreading System.....	93
4.1.2.	Non-Spreading System	98
4.2.	Characterisation of Three-Phase Fluids.....	103
4.2.1.	Quantification of Spreading and Non-Spreading Systems	103
4.2.2.	Three-dimensional Visualisation of Three-Phase Fluids	108
4.2.3.	Analysis of Spatial Distribution of Fluids Using Network Model	111
4.3.	Computational Analysis of Connectivity for Three-Phase Fluids	115
Chapter 5	Conclusions and Recommendations	120
References		122

List of Figures

Fig. 2-1 , Three-phase fluid distributions in a strongly water-wet glass micromodel (a) Positive spreading coefficient, $C_s = +17.7 \text{ mNm}^{-1}$ (b) Negative spreading coefficient, $C_s = -8.1 \text{ mNm}^{-1}$, (1-gas, 2-oil and 3-water), Acquired by Øren and Pinczewski (1995).....	9
Fig. 2-2 , Three-phase in a corner with half angle β (a) A stable oil layer between gas and water (b) An unstable oil layer when oil-water and gas-oil interface intersect at point B....	12
Fig. 2-3 , Three-phase configuration for a single corner. Acquired from (Helland and Skjæveland, 2006).	14
Fig. 2-4 , Cross section from wet tomogram showing water in white, benzyl alcohol in black, decane in light grey and grain in dark grey (b) X-ray intensity value of the phases (Acquired by Alvarado et al. (2004)).....	19
Fig. 2-5 , (a) Cross section from wet tomogram showing air in black, water in dark grey, immiscible organic liquid in white and solid in dark grey. (b) Corresponding partitioned image where organic liquid is denoted by red, water in blue, air in black and solid in light grey. Acquired by Schnaar and Brusseau (2006).....	20
Fig. 3-1 , A workflow diagram showing the procedural steps taken from experiments to image analysis and quantitative computations.....	23
Fig. 3-2 , Bentheimer sandstone core plugs used.....	27
Fig. 3-3 , Mercury injected capillary pressure showing the pore throat radius distributions of B1 and B2.	27
Fig. 3-4 , A photo of coated core plug, the post and lid used to hold on the rotation stage of micro-CT facility and seal the sample.....	28
Fig. 3-5 , Plasma cleaning equipment at Australian National University.	28
Fig. 3-6 , X-ray intensity attenuation value for a range of energy per length scale of $100\mu\text{m}$	33
Fig. 3-7 , X-ray images of water doped with 0.1 and 0.5 mole of Caesium Iodide (CsI) and n-Dodecane doped with 10%, 40%,50% and 100% by weight of Iodododecane (IDD). ..	33

Fig. 3-8 , An example of 2D slice from wet tomogram saturated with Iodododecane, 0.1M CsI and air. High density of Iodododecane caused beam-hardening artifact and resulted in a low quality image.	37
Fig. 3-9 , Pendant drop experimental setup.....	37
Fig. 3-10 , Three-phase fluids distributions in a strongly water-wet glass micromodel for (a) the positive spreading system ($S=+5.9 \text{ mNm}^{-1}$) and (b) the negative spreading system ($S=-8.7 \text{ mNm}^{-1}$).....	38
Fig.3-11 , Schematic of Flooding Set-up	40
Fig. 3-12 , Helical micro-CT system at the Australian National University (ANU). Both detector and sample stage can be positioned independently. The X-ray source is fitted with external cooling to avoid differential heating of the sample during very short sample-distance experiments.	42
Fig. 3-13 , Acquisition geometry for helical cone-beam micro-CT, L is camera length and P is pitch. H and W represent the height and width dimensions of the detector. The diagram taken from (Varslot et al., 2011b)	42
Fig. 3-14 , Comparison of phase contrast fringes (a) Imaging at 80Kev and filtering with 1.2mm Al (b) Imaging at 100Kev and filtering with 1.5mm Al. The halos are reduced significantly using higher energy and thicker filter.	51
Fig. 3-15 , Sections from a wet tomogram of Bentheimer sandstone (a) without the AD filter (b) with the AD filter.....	54
Fig. 3-16 , Examples of registered 2D slices of Bentheimer sandstone (a) dry image (b) wet image containing water, oil and air (c) – (d) magnified view of registered dry and wet images. The oil is shown in bright, water in dark grey and gas in black.....	56
Fig. 3-17 , A schematic of the coefficient value of dry and wet tomograms and the subtraction result. In the difference tomogram, the solid and air regions (marked with a striped pattern) represent a zero intensity value. The intensity value of the oil and water regions (marked in red and blue) remains constant as shown in the subtracted tomogram. The clay in the wet tomogram is saturated with water. After subtraction, the water value remains unchanged, while the clay value becomes zero.	61
Fig. 3-18 , (a) An example of registered grey-scale slice of dry tomogram containing pore (black) and grey (solid) and (b) Corresponding intensity histogram (c) Registered grey-scale	

slice of wet tomogram containing air (dark), solid (grey), water (dark grey) and oil (bright) and (d) Corresponding intensity distribution 62

Fig. 3-19, (a) An example of dry slice showing pore(black) and solid (grey) (b) Wet slice containing water (dark grey), oil (bright), solid (grey) and air (black) (c) Subtraction containing water (dark grey) and oil (bright). (d) Intensity distribution of original dry (red), wet (blue) and normalised dry (green) images. The entire intensity histogram of dry image is shifted to right according to NF and C factors. (e) Subtraction without renormalisation of dry image..... 63

Fig. 3-20, Optimal workflow for segmentation of partially saturated Bentheimer sandstone containing three-phase fluids (water, oil and gas)..... 68

Fig.3-21, (a) a 2D registered slice of dry with resolution of 3.46 μm and (b) a 2D registered slice of wet with resolution of 3.97 μm from 3D tomograms. The wet image contains three-phase fluids under positive spreading conditions ($C_s = +5.9\text{mNm}^{-1}$). Grey, dark grey, bright, and black are solid, water, oil and gas, respectively. 71

Fig. 3-22, (a) An example of a 2D slice from the segmented dry tomogram (sample B1) where pore is black, solid is khaki and clay is green. (b) An intensity histogram of the dry tomogram shown with a thick solid black line; Intensity distributions of pore (yellow), clay (green) and solid (black) after segmentation of dry tomogram. 71

Fig. 3-23, Comparison between measured mercury injection (MICP) and corresponding computations on the dry segmented image. The comparison shows the high quality of the dry image resolved pore space. 73

Fig. 3-24, (a) 2D slice of segmented dry image from B1 tomogram where pore is black, clay is green and solid is khaki, (b) 2D slice of wet image where oil, water, gas and solid are bright, dark grey, black and grey, respectively. (c) Solid (khaki) and gas (black) are separated but oil and water are undecided (blue) yet, (d) Final segmented 2D slice showing gas with black, oil with red, water with blue and clay with green. (e) Intensity histogram of original wet tomogram shown with thick black solid and Gaussian fit of intensity values of pore (yellow), water(blue), oil(red), clay(orange) and solid (green) after finalising segmentation of wet tomogram. Spreading coefficient is $C_s = +5.9\text{mNm}^{-1}$ 75

Fig. 3-25, Intensity histogram of dry tomogram (sample B2) displaying with thick solid black line; Gaussian Intensity fits of pore (yellow), clay (green) and solid (red line) after segmentation of dry tomogram. 78

Fig. 3-26, (a) 2D slice of segmented dry tomogram where the pore, solid and clay are denoted by black, khaki and green, respectively. (b) Comparison between measured mercury injection (MICP) and corresponding computations on the dry segmented image. 78

Fig. 3-27, (a) 2D slice of segmented dry image from B2 tomogram where pore is black, clay is green and solid is khaki, (b) 2D slice of wet image where oil, water, gas and solid are bright, dark grey, black and grey, respectively. (c) Solid (khaki) and oil (red) are separated but gas and water are undecided (black) yet, (b) final segmented 2D slice showing gas with black, oil with red, water with blue and clay with green. (e) Intensity histogram of original wet tomogram shown with thick black solid and Gaussian fit of intensity values of pore (yellow), water(blue), oil(red) ,clay(orange) and solid (green) after finalising segmentation of wet tomogram. Spreading coefficient is $C_s = -8.7\text{mNm}^{-1}$ 79

Fig. 3-28, Illustration of pore interconnections and partitioning algorithm (a) segmented pore-throat, pore-white and solid-black (b) calculated Euclidean Distance Map (c) Calculated covering sphere radius, the centre is calculated from maximum covering radius (d) The medial axis junction (e-g) Illustration of generation of the medial axis on a small 3D subset of a porous image by Jones et al. (2009). 82

Fig. 4-1, Registered 2D slices from (a) dry tomogram of B1 where pore and solid are black and grey and (b) wet tomogram of B1 containing positive spreading fluids system($C_s = +5.9\text{mNm}^{-1}$), (c) – (d) Magnified sections from wet tomogram where air, oil, water and solid are black, bright, dark grey and grey..... 88

Fig. 4-2, Registered 2D slices from (a) dry tomogram of B2 where pore and solid are black and grey, (b) wet tomogram of B2 containing negative spreading fluids system($C_s = -8.7\text{mNm}^{-1}$), (c) - (d) Magnified sections from wet tomograms where air, oil, water and solid are black, bright, dark grey and grey. 90

Fig. 4-3, Section from the positive spreading system tomograph showing gas-oil redistribution during the scanning period..... 92

Fig. 4-4, Sections from positive spreading tomograms of core plug B1, $200 \times 200 \times 200$ voxels³ (a) dry, (b) wet. Solid, air, water and oil are grey, black, dark grey and bright, respectively. (c) Section representing subtraction of dry and wet images where oil shown in bright ,water in grey and solid-air in black , (d) Segmented subset shows water in blue, air in black, oil in red and solid in khaki. 96

Fig. 4-5, Sections from positive spreading tomograms of core plug B1, $200 \times 200 \times 200$ voxels³ (a) dry, (b) wet. Solid, air, water and oil are grey, black, dark grey and bright, respectively. (c) Section representing subtraction of dry and wet images where oil shown in bright, water in grey and solid-air in black, (d) Segmented subset shows water in blue, air in black, oil in red and solid in khaki. 97

Fig.4-6, Sections from negative spreading tomograms of core plug B2, $200 \times 200 \times 200$ voxels³ (a) dry, (b) wet. Solid, air, water and oil are grey, black, dark grey and bright, respectively. (c) Section representing subtraction of dry and wet images where oil shown in bright, water in grey and solid-air in black, (d) Segmented subset shows water in blue, air in black, oil in red and solid in khaki. 99

Fig. 4-7, Sections from negative spreading tomograms of core plug B2, $200 \times 200 \times 200$ voxels³ (a) dry, (b) wet. Solid, air, water and oil are grey, black, dark grey and bright, respectively. (c) Section representing subtraction of dry and wet images where oil shown in bright, water in grey and solid-air in black, (d) Segmented subset shows water in blue, air in black, oil in red and solid in khaki. 102

Fig. 4-8, A measure is made of the saturation of the oil, water and gas across the imaged volume. The oil phase is denoted in a red colour, gas shown in black and water in blue. The spreading coefficient was $+5.9 \text{ mNm}^{-1}$ 106

Fig. 4-9, A measure is made of the saturation of the oil, water and gas across the imaged volume. The oil phase is denoted by red colour and the gas and water are demonstrated by black and blue, respectively. The spreading coefficient was of -8.9 mNm^{-1} 107

Fig. 4-10, Three-dimensional visualisation of oil (red), water (blue) and gas (yellow) for positive spreading system. 109

Fig. 4-11, Three-dimensional visualisation of oil (red), water (blue) and gas (yellow) for negative spreading system. 110

Fig. 4-12, Quantitative characteristics of water, gas and oil spatial distributions across 3D imaged volume of B1: pore radius and pore volume equivalent radius distributions of (a)-(b): water, (c)-(d): gas, and (e)-(f): oil. The fluids displayed a positive spreading coefficient ($C_s = +5.9 \text{ mNm}^{-1}$) 112

Fig. 4-13, Quantitative characteristics of water, gas and oil spatial distributions across 3D imaged volume of B2: pore radius and pore volume equivalent radius distributions of (a)-

(b): water, (c)-(d): gas, and (e)-(f): oil. The fluids displayed a negative spreading coefficient ($C_s = -8.7 \text{ mNm}^{-1}$)..... 114

List of Tables

Table 3-1, X-ray attenuation value.....	34
Table 3-2, Physicochemical properties of the fluids used in the experiment.....	38
Table 3-3, X-ray imaging parameters used for dry and wet B1 and B2 samples	46
Table 3-4, Acquisition data for dry and wet X-ray imaging.....	46
Table 4-1, The list of samples used in this study and their properties.	104
Table 4-2, Euler Characteristics (μm^{-3})	117
Table 4-3, Euler Characteristics (μm^{-3})	117

Chapter 1

Introduction

The distribution of fluids in porous media during three-phase displacements is important to the development of an improved understanding of oil recovery in a number of gas flooding processes including tertiary gas flooding to recover waterflood residual oil (Chatzis et al., 1988, Kantzas et al., 1988a). A considerable body of work, both experimental and theoretical, has shown that the recovery of oil in the presence of water and gas under strongly water-wet conditions depends on the spreading characteristics of the oil phase (Øren and Pinczewski, 1994). Observations in simple glass micromodels (Øren and Pinczewski, 1995) clearly show that, for positive spreading systems, oil phase is distributed as a continuous film spreading between the water and gas phases. Øren and Pinczewski (1995) showed that the recovery of waterflood residual oil through tertiary gas flooding was considerably higher for positive spreading systems than for negative spreading systems where the oil was distributed as isolated lenses. These observations have prompted the development of a number of two- and three-dimensional three-phase network models which are now used to estimate three-phase relative permeabilities, residual saturations and the pore-scale distribution of fluids (Pereira et al., 1996, Lerdahl et al., 2000, Piri and Blunt, 2005).

Although continuous oil spreading films are readily observed in simple glass micromodel experiments, it has not been possible to confirm the presence of these films in actual porous media. Hence, visualisation of three fluids in actual porous media has long

stayed one of the existing obstacles in assessing the capability of three-phase network models derived from simple micromodel observations to predict three-phase flow behaviour. For this purpose, Vizika et al. (1998) used Cryo-SEM to observe the pore-scale distribution of oil, water and gas in Fontainebleau sandstone for spreading and non-spreading conditions. Their observations were consistent with the earlier glass micromodel observations. However, the two-dimensional nature of their observations and the limited field of view made it impossible to comment on the spatial connectivity and continuity of the oil phase for positive spreading systems and to compare this with the corresponding behaviour for negative spreading systems.

Recent advances in imaging technologies and image analysis techniques have provided the opportunity to observe directly the distribution of the fluids at pore-scale in actual porous rocks with greater clarity than previous studies (Alvarado et al., 2004, Schnaar and Brusseau, 2005, Culligan et al., 2006, Kumar et al., 2009a, Karpyn et al., 2010, Youssef et al., 2010, Landry et al., 2011). However, majority of these studies attempted to visualise two phases in porous media. There are only two studies reported in the literature that employed micro computed tomography (Micro-CT) to visualise three immiscible fluids in unconsolidated porous media (Alvarado et al., 2004, Schnaar and Brusseau, 2006). Both studies reported positive spreading coefficient which suggests the existence of spreading films. Note that Alvarado et al. (2004) used three immiscible liquids whereas Schnaar and Brusseau (2006) used oil, water and air. Although the fluids used in the studies were doped to improve contrast between the phases and the image resolution was approximately 10 microns, it was only possible to resolve the thickest films and no attempt was made to determine their spatial distribution or continuity.

The objectives of this thesis are to:

1. Image, using high-resolution micro-CT, the distribution of oil, water and air in Bentheimer sandstone for positive and negative spreading systems under strongly water-wet conditions.
2. Confirm the presence and continuity of oil spreading films for positive spreading systems in real porous media and the absence of spreading films for negative spreading systems.

The thesis is organised as follows:

Chapter 2 — Background and Literature Review

This chapter provides a review of the current understanding of the pore-scale fluid distribution and displacement mechanisms for three-phase flow in porous media and the role of oil spreading films in the recovery of waterflood residual oil. This is followed by a critical discussion of previous studies and attempts to visualise the distribution of immiscible fluids in real porous media.

Chapter 3 — Experimental Methodology

This chapter presents in three subsections the methodology followed to qualify and quantify accurately three-phase fluids in Bentheimer sandstone. The first section describes how the fluids were selected. The X-ray tomography facility is then described. In the second section, the experimental methods for sample preparation and plasma treatment, experimental setup and flooding procedure are given. In the third section, the image processing techniques used to enhance the quality and analysis of X-ray images are

documented. Basically, it includes the registration and segmentation methods, three-phase segmentation workflow, the generation of pore network models, and the assessment of phases' spatial connectivity using the Euler-Characteristics method and a 3D quantification technique.

Chapter 4 — Results and Discussions

This chapter presents the 3D visualisation images of three phases in Bentheimer sandstone and compares three-phase fluid distributions in the rock sample for both positive and negative spreading systems. The presence of oil films and their continuity within the rock sample are discussed for positive and negative spreading systems using the differential imaging technique. The fluid saturations determined from segmented images and implications are discussed for systems that exhibit various spreading conditions. Quantitative maps of three-dimensional occupancy of each phase in the segmented images were generated and compared for positive and negative spreading systems. The spatial connectivity of each of the phases at the end of the tertiary gas flooding is analysed and discussed using quantitative measures obtained from the Euler Characteristics method.

Chapter 5 — Conclusions and Recommendations

This chapter presents thesis conclusions and future recommendations.

Chapter 2

Literature Review

An understanding of three-phase flow in porous media is important in the engineering design and operation of many significant industrial processes. Particularly important examples in the present context are improved oil recovery processes where a gas phase is injected into reservoirs containing oil and water. Gas injection is thought to increase ultimate oil recovery because the oil phase, in the presence of water and gas, remains connected down to lower saturations than in the presence of water alone (Dumore and Schols, 1974, Chatzis et al., 1988, Kantzas et al., 1988a, Vizika, 1993). The higher oil recoveries from gas injection projects are attributed to the presence of continuous oil films between the non-wetting gas and wetting water phases, a process which is commonly referred to as 'film drainage'. The presence of oil films between gas and water has been confirmed by direct observation in two-dimensional glass micromodels (Kantzas et al., 1988b, Kalaydjian, 1992, Oren et al., 1992, Øren and Pinczewski, 1992, Soll et al., 1993).

Although continuous oil spreading films are clearly present in simple two-dimensional glass micromodel experiments, the existence of oil films in actual porous media is yet to be confirmed. Vizika et al. (1998) used Cryo-SEM to observe the pore-scale distribution of oil, water and gas in Fontainebleau sandstone. They reported observations consistent with the earlier observations in glass micro models, however, the two-dimensional nature of the observations and the limited field of view made it impossible to comment on the connectivity and continuity of the films. Alvarado et al. (2004) and

Schnaar and Brusseau (2006) used X-ray micro computed tomography to image the distribution of three immiscible fluids in sand packs. Although the fluids used in the studies were doped to improve contrast between the phases and the image resolution was approximately 10 microns, it was only possible to resolve the thickest films and no attempt was made to determine their spatial distribution or continuity.

This chapter presents a detailed review of previous visualisation studies of oil films in three phase systems under strongly wetting conditions. The review includes studies in model systems and in actual porous media together with theoretical studies of capillary stabilised films in three fluid phase systems.

2.1. Three-Phase Flow in Porous Media

Dumore and Schols (1974) reported measurements of residual oil saturations for gas displacements in the presence of connate water. The displacements for Bentheimer cores used the porous plate method and glass bead packs were used for vertical gravity drainage tests. They observed very low residual oil saturations for both experiments and suggested that this was due to oil spreading on the surface of the connate water in the presence of gas. They performed experiments with spreading and non-spreading oils and observed similarly low residual oil saturations. They suggested that the low residual oil saturations were due to film flow and that the low saturations were independent of whether oil was spreading or non-spreading.

Kantzas et al. (1988a, 1988b) conducted vertical gravity drainage displacement experiments in water-wet systems where gas was injected to displace waterflood residual oil. The experiments were carried out in glass bead packs, Berea sandstone and two-dimensional glass micromodels using soltrol, water and air as the fluids. Like previous

studies (Dumore and Schols, 1974, Hagoort, 1980), they attributed the high oil recoveries for the bead packs and Berea cores to gravity drainage of oil through continuous oil films, which spread between the water and gas phases, observed in their micromodel experiments. They described the displacement of oil and water by gas as a sequence of two drainage processes in which gas displaces oil which in turn displaces water. Further, Kantzas et al. (1988b) showed that the presence of oil films in water-wet glass micromodels was dependent on pore geometry and capillary pressure (fluid curvatures).

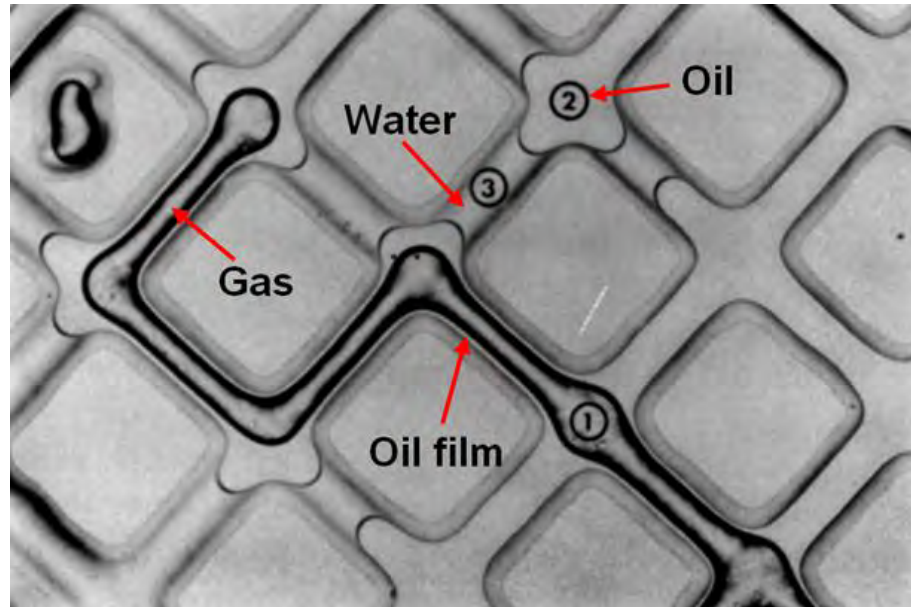
Kalaydjian (1992), Øren et al. (1992), Øren and Pinczewski (1992), Vizika (1993) and Soll et al. (1993) used strongly water-wet glass micromodels with regular networks to investigate the mechanisms by which waterflood residual oil is recovered during tertiary gas flooding. Øren et al. (1992) and Øren and Pinczewski (1992) performed their displacements in horizontal micromodels using fluid systems with positive and negative spreading coefficients. The spreading coefficient for an oil-water-gas system is defined as:

$$C_s = \delta_{gw} - (\delta_{ow} + \delta_{go}) \quad \text{Eq. 2.1}$$

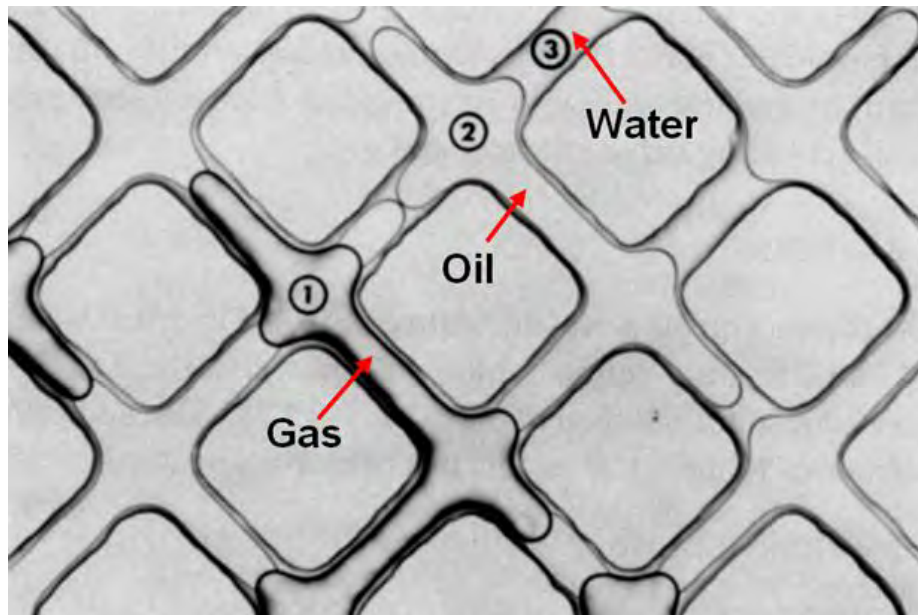
where δ_{gw} , δ_{go} and δ_{ow} are the two-phase gas-water, gas-oil and oil-water interfacial tensions, respectively. The spreading coefficient defined by the above equation is *the initial* spreading coefficient and is a measure of the tendency of oil to form spreading films on water in the presence of gas (Adamson, 1990). Øren and Pinczewski (1992) observed the presence of oil spreading films for the positive spreading system and the absence of oil films for the negative spreading system. Reproductions of their observations are shown in **Fig. 2-1**. They also reported considerably higher tertiary gasflood oil recoveries for the positive spreading than for the negative spreading system. They also attributed this higher recovery to flow through continuous oil films. Consistent with the earlier observations of

Kantzas et al. (1988a, 1988b), they showed that the gas-oil displacements occurred by a 'double drainage' mechanism in which gas preferentially displaces oil and the displaced oil in turn displaces water. They noted that oil displaced in the first drainage process could flow through films to displace water at a site remote from the site of the first displacement. Pereira et al. (1996) developed a dynamic network model based on these observations which accounted for flow through oil spreading films and water wetting films. The computed displacement behaviour and oil recoveries were in good agreement with the observations and measurements reported by Øren et al. (1992) and Øren and Pinczewski (1994).

Vizika and Lombard (1996) reported the results of gravity assisted inert gas injection experiments in water-wet, oil-wet and fractionally-wet unconsolidated sand-packs with positive and negative spreading fluid systems. Their results show that the highest oil recoveries were obtained with water-wet systems and fluids with positive spreading coefficients. The lowest oil recoveries were obtained with oil-wet systems and negative spreading coefficients. They suggest that the higher oil recoveries were due to the existence of continuous oil spreading films in water-wet and partially-wet media and the absence of such films for negative spreading fluid systems. They conclude that spreading coefficient is a crucial parameter in determining oil recovery in three-phase oil-water-gas systems.



(a)



(b)

Fig. 2-1, Three-phase fluid distributions in a strongly water-wet glass micromodel (a) Positive spreading coefficient, $C_s = +17.7 \text{ mNm}^{-1}$ (b) Negative spreading coefficient, $C_s = -8.1 \text{ mNm}^{-1}$, (1-gas, 2-oil and 3-water), acquired from Øren and Pinczewski (1995).

2.2. Spreading Behaviour in Porous Media

The studies discussed above clearly establish the importance of flow through continuous oil films in the recovery of oil by gas injection in the presence of water. However, the conditions for the existence of oil films are not clear. Kalaydjian (1992), Øren et al. (1992), Øren and Pinczewski (1992) and Vizika (1993) amongst others observed spreading films in glass micromodels when the initial spreading coefficient was positive. No spreading films were observed when the spreading coefficient was negative. Blunt et al. (1994) pointed out that this simple criterion was not consistent with the experimental findings of Dumore and Schols (1974) who observed similarly high oil recoveries in gravity assisted tertiary gas floods for both positive and negative spreading systems. This suggests that oil films are present for both positive and negative initial spreading coefficients.

The above apparent inconsistency was resolved by Dong et al. (1995) who, using a free energy analysis, showed that oil films can form between water and gas in corners of the pore-space for both positive and negative spreading systems. Kantzas et al. (1988b) suggested a similar result by considering the curvatures of oil-water and gas-oil interfaces in corners of capillaries. Keller et al. (1997) and Fenwick and Blunt (1998) considered gas-oil and oil-water interfaces in a corner with half angle of crevice (β) shown in Fig. 2-2. Following Kantzas et al. (1988b), they argued that a stable oil layer will exist between wetting water film in the corner and the non-wetting gas in the pore if the ratio of the oil-water radius, r_{ow} , to the gas-oil radius, r_{go} , is smaller than a critical radius, R_c , which is given by:

$$R_c = \frac{r_{ow}}{r_{go}} = \frac{\delta_{ow} P_{cgo}}{\delta_{go} P_{cow}} = \frac{\cos(\theta_{go} + \beta)}{\cos(\theta_{ow} + \beta)} \quad \text{Eq.2.2}$$

The oil layer would become unstable and disappear when the oil-water-solid and gas-oil three-phase-solid contact lines meet which is shown in **Fig. 2-2**. For a completely water-wet medium $\theta_{go} = \theta_{ow} = 0$ and we can write (Kalaydjian, 1992):

$$\cos\theta_{go} = 1 + \frac{C_s^e}{\delta_{go}} \quad \text{Eq. 2.3}$$

where θ_{go} and δ_{go} are the contact angle and interfacial tension between water and gas, respectively. The spreading coefficient C_s^e in **Eq. 2.3** is referred to as the *equilibrium* spreading coefficient defined as:

$$C_s^e = \delta_{gw}^e - (\delta_{ow}^e + \delta_{og}^e) \quad \text{Eq. 2.4}$$

C_s^e occurs when three phases are in thermodynamic equilibrium and gas-oil and oil-water interfacial tensions are modified by mass transfer across the interfaces (Adamson, 1990, Hirasaki, 1993). **Eq. 2.4** shows that the presence of oil films between water and gas in corners depends on the individual equilibrium interfacial tensions or the equilibrium spreading coefficient, the contact angles, the corner half-angles and capillary pressures. Keller et al. (1997) showed that their criterion for the presence of oil films in corners is consistent with the glass micromodel observations of Øren et al. (1992) where the equilibrium spreading coefficient for the positive spreading oil system with initial spreading coefficient $C_s = +17.7 \text{mMm}^{-1}$ was $C_s^e = 0 \text{mMm}^{-1}$ and for the negative spreading system with initial spreading coefficient $C_s = -8.1 \text{mMm}^{-1}$ was $C_s^e = -8.1 \text{mMm}^{-1}$.

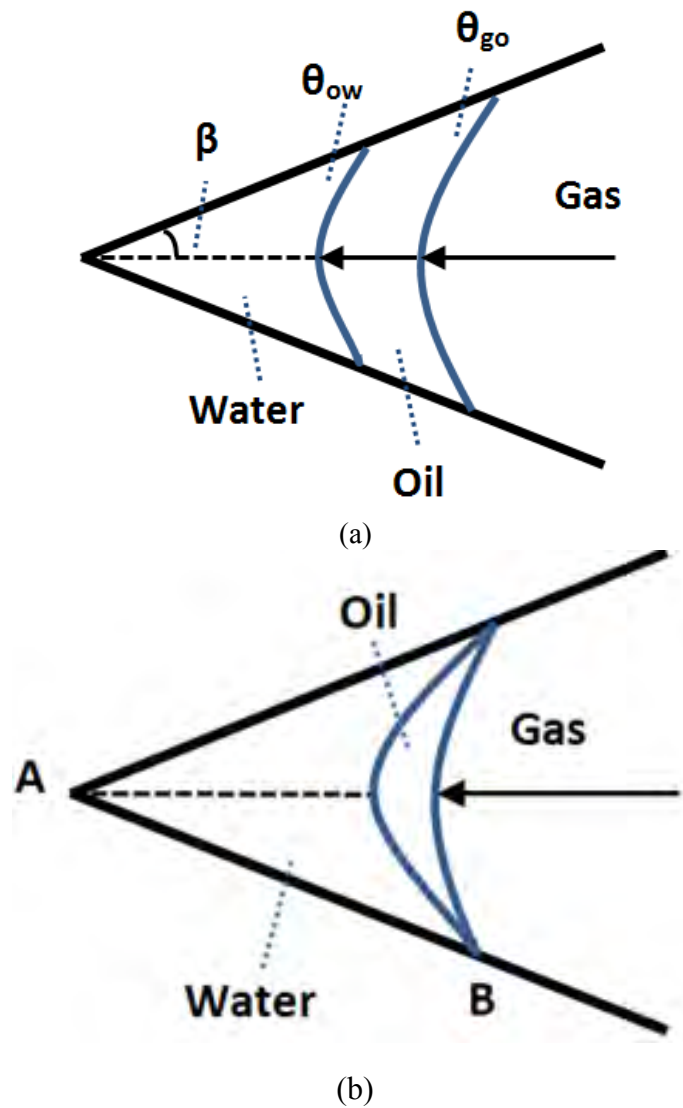


Fig. 2-2, Three phases in a corner with half angle β (a) A stable oil layer between gas and water (b) An unstable oil layer when oil-water and gas-oil interface intersect at point B. θ_{go} is the gas-oil contact angle and θ_{ow} is the water-oil contact angle (Fenwick and Blunt, 1998).

Eq. 2.4 shows that oil films can be present in corners for non-spreading systems when the initial spreading coefficient is only slightly negative, when the porous medium is not completely water-wet and when the corner half-angle is small. These conditions are likely to be met in laboratory sand pack floods and in real porous media.

The above analysis for capillaries with angular cross-sections has been extended to a wide range of wettabilities, interfacial tensions, contact angles, capillary pressures and saturation histories. Using geometric and free energy arguments Piri and Blunt (2002, 2003, 2004) and Helland and Skjæveland (2006) have shown that oil films may exist for a wide range of conditions and pore occupancies. Fig. 2-3, reproduced from Helland and Skjæveland (2006), shows a range of possible pore occupancies and fluid configurations with systems displaying mixed wettability. Configurations **E**, **F**, **G** and **O** show oil films between water and water. **E** and **G** show oil films between water in corners and water in the bulk of the pore while **F** shows an oil film between water in corners and water in films in the bulk of the pore with the pore primarily occupied by oil. **O** shows a similar configuration to **F** with the pore primarily occupied by gas. Configurations **M**, **N** and **P** show oil films between water and gas. **M** and **N** show oil films between water in corners and gas in the bulk of the pore and **P** shows oil films between water in corners and gas in films in the the bulk of the pore with the pore occupied primarily by water. It is interesting to note that the only configurations commonly observed in the previously discussed glass micromodel and angular capillary studies are similar to **M** and **N**; oil films between water in corners and gas in the bulk of the pore.

Piri and Blunt (2005) and Valvatne et al. (2005) developed quasi-static network models incorporating the above three-phase fluid configurations and used the model to predict oil relative permeabilities in the presence of water and gas.

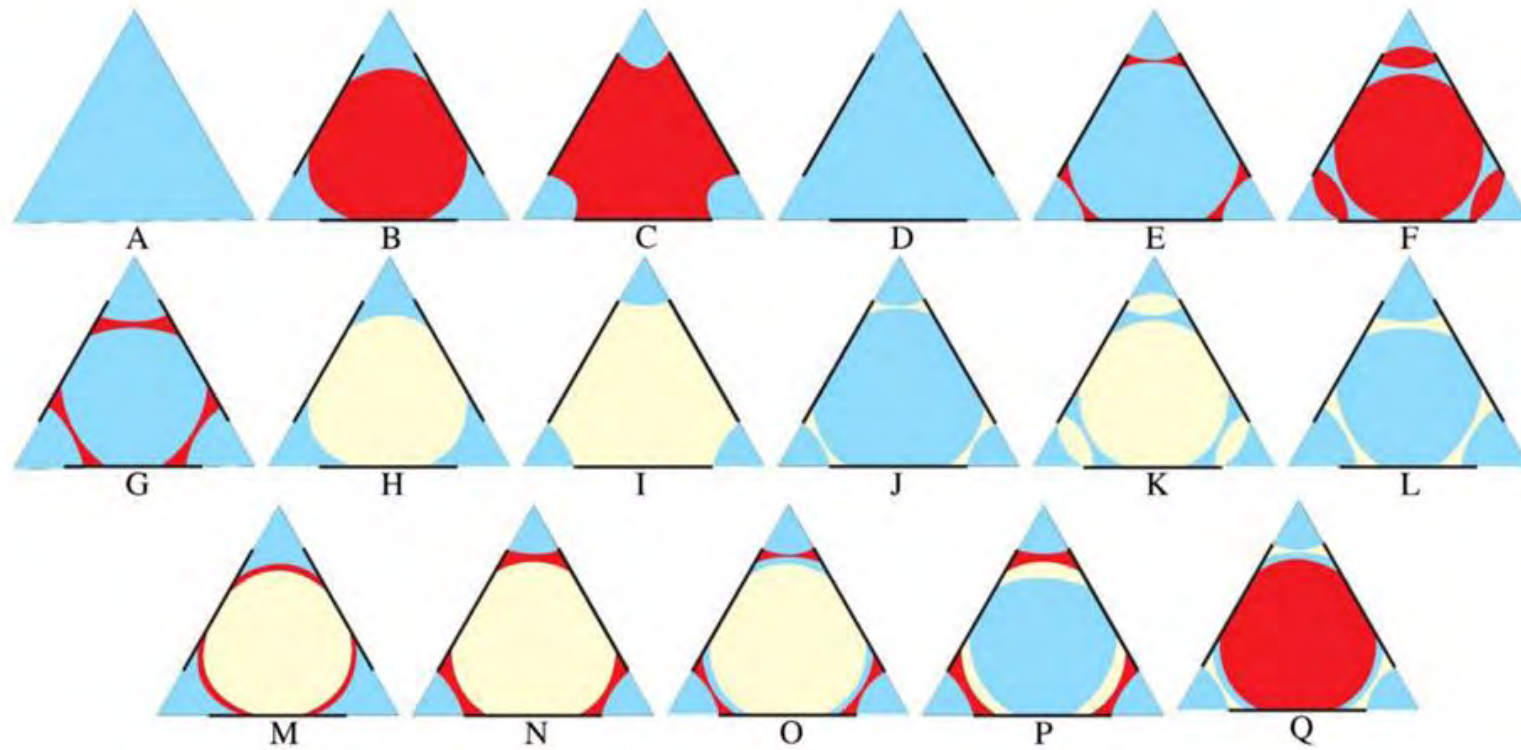


Fig. 2-3, Three-phase configuration for a single corner, acquired from Helland and Skjæveland (2006).

Valvatne et al. (2005) found that the network models overpredicted oil relative permeabilities and suggested that this may be due to the models over estimating the conductivity and/or the thickness of the films. In an earlier study, Pereira et al.(1996) developed a dynamic two-dimensional network model for strongly water-wet conditions where oil films were only present between water in corners and gas in the bulk of the pore as shown in Fig. 2-2. They compared their model for tertiary oil recoveries with the experimentally measured recoveries from glass micromodel reported by Øren et al. (1992) and found a good agreement.

2.3. Oil Films in Real Porous Media

The vast body of experimental and theoretical work discussed above suggests that the recovery of oil in the presence of water and gas depends on the presence of continuous oil films and that this is related to the spreading characteristics of the oil phase (three-phase interfacial tensions), the geometry of the pore-space, the wettability of the solid and capillary pressure. Although continuous oil spreading films are readily observed in simple glass micromodel and angular capillary tube experiments, it has not yet been possible to confirm the presence and continuity of these films in actual porous media.

Vizika et al. (1998) used Cryo-SEM to observe the pore-scale distribution of oil, water and gas in small 6 mm diameter plugs of Fontainebleau sandstone under strongly water-wet conditions. They used two water-oil-gas systems with positive and negative initial spreading coefficients of $+11 \text{ mNm}^{-1}$ and -1.5 mNm^{-1} . They reported the presence of oil films for the positive spreading system and the absence of oil films for the negative spreading system. The oil formed disconnected droplets or rivulets resulting in larger residual oil saturations for the non-spreading system than for the spreading system. These

observations are consistent with the earlier glass micromodel observations. However, the two-dimensional nature of the observations and the limited field of view (order of microns) made it impossible to comment on the connectivity and continuity of oil films for the positive spreading system.

Alvarado et al. (2004) reported the use of X-ray micro computed tomography (micro-CT) to image the distribution of three immiscible fluids in loosely packed quartz sand-packs at the pore scale level. **Fig. 2-4(a)** shows a cross section of three-phase distributions in the loose sand pack and **Fig. 2-4(b)** shows the phases X-ray intensity values obtained by Alvarado et al. (2004). The imaging was done at a single incident energy level and the image resolution was reported to be 9 microns. The sand-packs were 7 mm in diameter with an average grain size of 1 mm. The fluids used were water, benzyl alcohol and decane. The water was doped with sodium iodide and the decane with iodododecane to increase the contrast between the phases. The sand-pack was imaged both in the dry state and with the fluids in the pore-space (wet state). The dry image was partitioned using simple thresholding and subtracted from the wet image to reduce the problem of identifying the three fluid phases to partitioning of the doped high attenuating water and low attenuating benzyl alcohol phases. Although the authors suggested that the three-fluids used produced a spreading system, it was not possible to identify intermediate phase spreading films or water wetting films.

Schnaar and Brusseau (2006) also used synchrotron micro-CT to image the distribution of three immiscible fluids in coarse sand and sandy soil packs. The sand packs were approximately 5 mm in diameter and the fluids used were water, air and tetrachloroethane. The water was doped with caesium iodide and the tetrochloroethane with iodobenzene to enhance image contrast. To further improve contrast images were obtained at three different incident energies to take advantage of the different X-ray

adsorption characteristics of the doping compounds used. Image resolution was estimated to be approximately 9 microns. Image subtraction was used to produce images wherein only voxels comprising the fluid of interest displayed an attenuation level above background. **Fig. 2-5** shows a 2D section of the wet tomogram displaying three-phase fluids and its corresponding segmented image. Although the authors suggested that a significant portion of the organic liquid existed as lenses and films in contact with air, these could not be fully resolved because of image signal noise. The image smoothing required to reduce noise to acceptable levels effectively removed small features at phase boundaries and interfaces such as films.

Iglauer et al. (2013) reported the use of synchrotron radiation to image sandstone core (Clashach sandstone) at residual gas saturation in a core containing initial water and oil followed by a waterflood (gw) and a waterflooded core followed by another waterflood (w gw). They used brine doped with potassium iodide (KI) as water phase, Bromododecane as oil phase and N₂ as the gas phase. The fluid system produced a spreading coefficient value of -11.05 mNm^{-1} . Image resolution was estimated to be approximately 9 microns. Although three-phase fluids used produced a negative spreading system, the authors reported the existence of oil films with a thickness ranging from 1 to 2 μm only in the gw system. They however did not comment on two- or three-dimensional connectivity and continuity of the oil films in the sandstone. It was not also possible to fully differentiate between oil films and phase contrast artifact in reported images due to high level of noise to signal and low quality of images.

More advances in micro-CT imaging techniques and image analysis technologies now make it possible to image fluids in the pore-space of actual porous rocks with greater clarity than in previous studies (Kumar et al., 2009a, Kumar et al., 2009b). Kumar (2009) used high resolution micro-CT together with a three-dimensional image registration

technique (Latham et al., 2008) that produces a voxel to voxel alignment of dry and partially saturated images of the same rock to visualise the distribution of water and air in Fontainebleau sandstone and carbonate rocks at a number of well-defined wettability states. The image registration technique used by Kumar et al. (2009b) reduces uncertainties in phase separation at interfaces when subtracting images at different saturations - dry images from the partially saturated images. This reduces the effective signal to noise ratio at the solid-fluid boundary making it possible to identify smaller features at the boundary, possibly films.

The aim of the present study is to extend the two-phase visualisation to three phases and, for the first time, show the three-dimensional distribution and connectivity of the intermediate oil phase in a three-phase water, oil and gas system in an actual porous rock under strongly water-wet conditions for positive and negative spreading conditions.

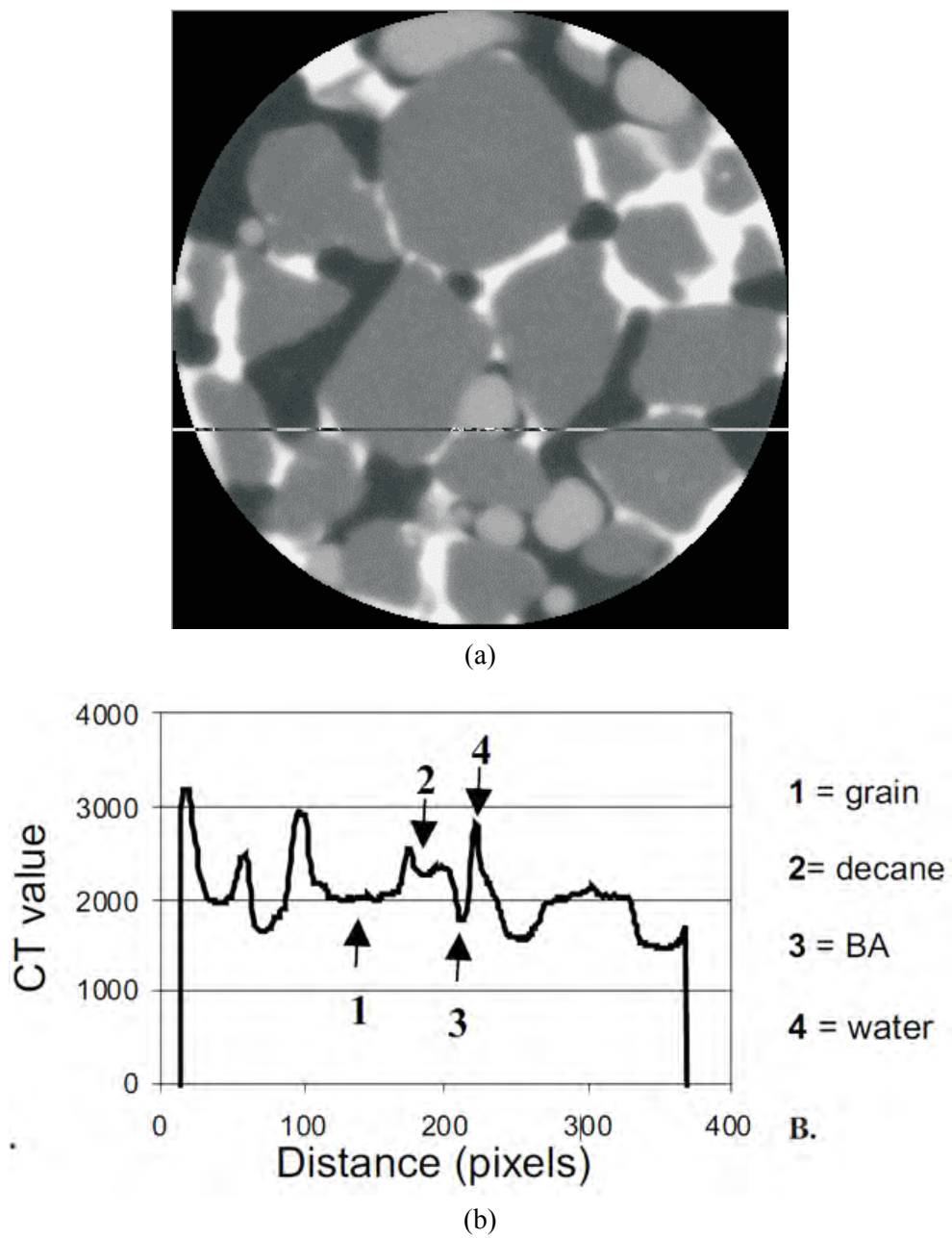
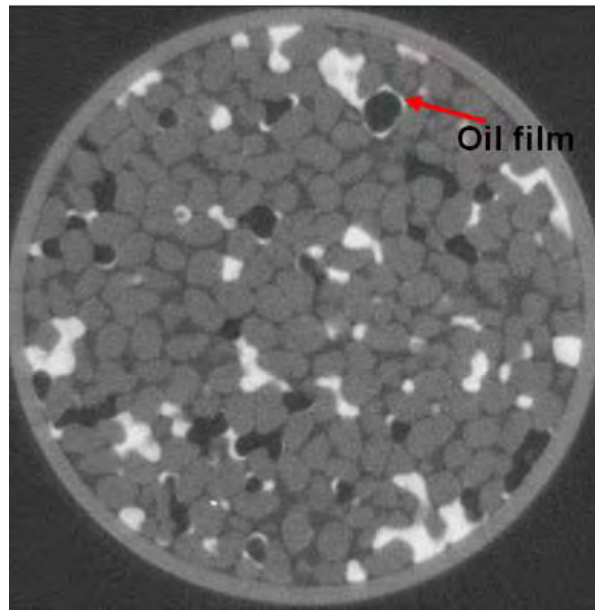
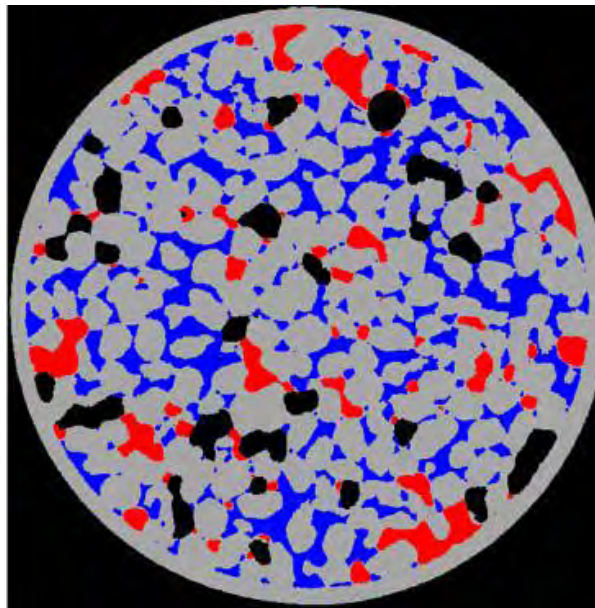


Fig. 2-4, Cross section from wet tomogram showing water in white, benzyl alcohol in black, decane in light grey and grain in dark grey (b) X-ray intensity value of the phases (Acquired from Alvarado et al., 2004)



(a)



(b)

Fig. 2-5, (a) Cross section from wet tomogram showing air in black, water in dark grey, immiscible organic liquid in white and solid in dark grey. (b) Corresponding partitioned image where organic liquid is denoted by red, water in blue, air in black and solid in light grey. Acquired from Schnaar and Brusseau (2006).

Chapter 3

Experimental and Computational Methodologies

This chapter provides a detailed description of:

- the three-phase fluid systems and porous media used in the experiments,
- the micro-CT facility and data acquisition and reconstruction process used to acquire images,
- the procedures followed for sample preparation, flooding experiments and X-ray imaging, and
- the image analysis and statistical method used to examine the spatial distribution and connectivity of the phases.

3.1. Workflow

Fig. 3-1 illustrates briefly the workflow adapted in this thesis. There are basically three parts: the experimental, image analysis and characterisation of spatial distribution and connectivity of three immiscible phases (oil-water-gas) in a porous medium which was a rock sample from Bentheimer sandstone.

The experimental part includes porous rock sample preparation, establishment of the strong water-wetness of the rock sample (plasma treatment), mercury intrusion capillary pressure (MICP), fluid selection for better contrast between the phases in X-ray imaging, core flooding to obtain spatial distribution of three phases in the rock sample and X-ray micro-CT imaging.

First, dry rock sample was imaged. Then the same rock sample was saturated with the wetting phase (doped water) completely and flooded first by injecting doped oil followed by air injection. Two sets of oil-water-gas systems were used in this thesis: one with a positive spreading coefficient and the other with a negative spreading coefficient. The air-flooded rock sample was then imaged which completes the experimental part. The image analysis part started with filtering the image followed by registering the dry and wet images. Then renormalisation and subtraction were applied to the registered dry and wet images. This part ends with the segmentation of the images to quantify the phase distributions.

Phase distributions and connectivity within rock sample werethen investigated in the last part of the workflow. Three methods were applied. The Euler Characteristics method was used to analyse the spatial connectivity of each of the phases at the end of the

air flooding. The pore-network analysis was used to quantify the phase distribution while 3D visualisation helped to visualise the phase distributions.

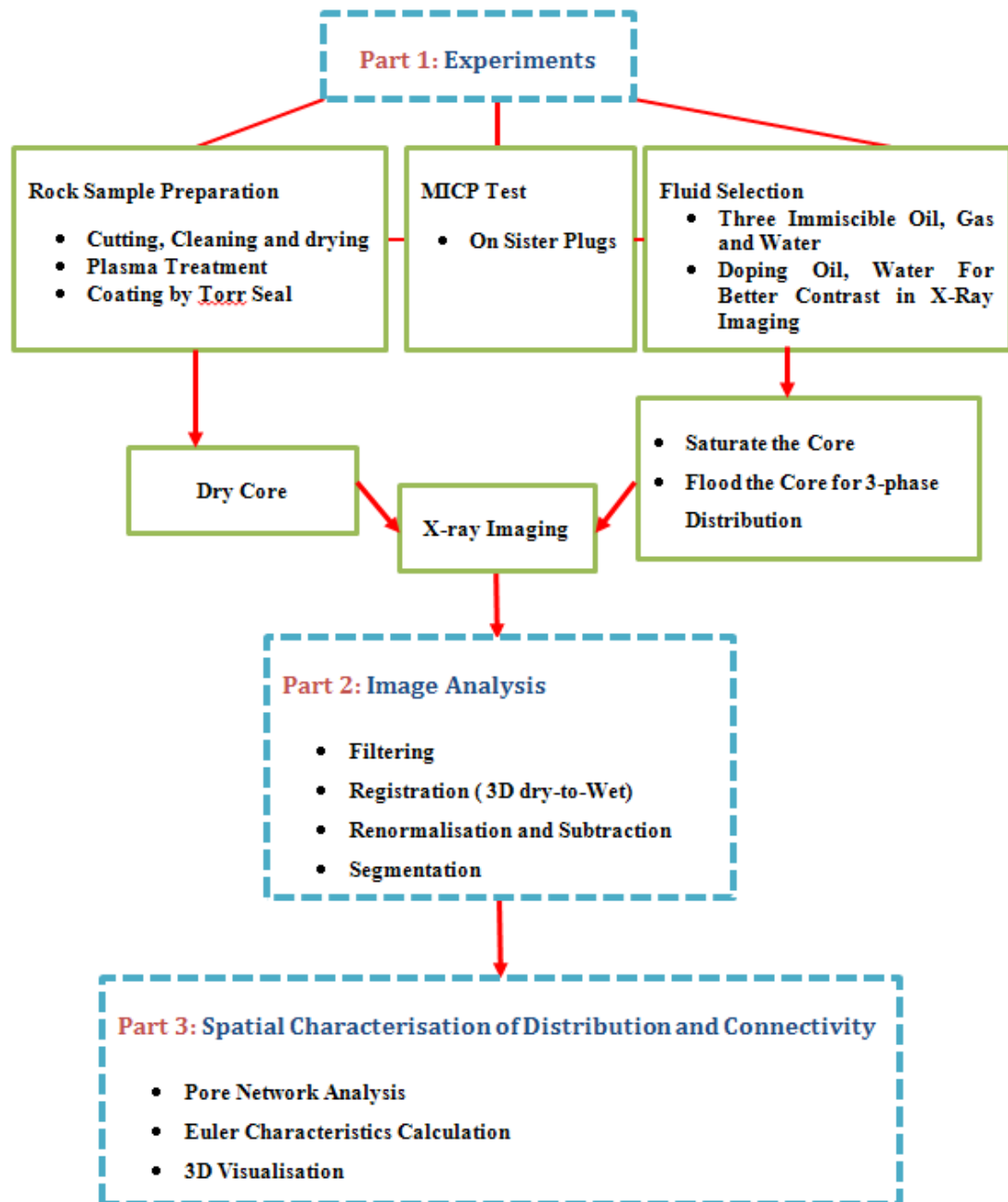


Fig. 3-1, A workflow diagram showing the procedural steps taken from experiments to image analysis and quantitative computations.

3.2. Experimental Methodology

3.2.1. Porous Medium

Bentheimer sandstone was used in this thesis. In order to avoid any effect of doped fluids of positive and negative spreading on porous medium, it was decided to use two sister plugs in the experiments. **Fig. 3-2** shows two small cylindrical core plugs, named B1 and B2, each with 5mm in diameter and about 50mm in length. These plugs were cut from a large Bentheimer block. The core plugs (B1 and B2) were cleaned in a Soxhlet extractor using a mixture of distilled water and Iso-propanol for 12hrs. They were then dried in an oven at 60°C for 24hrs.

Before proceeding with the experiments and undertaking micro-CT imaging, it was decided to run MICP tests on B1 and B2. The aim was to ensure that the cores (B1 and B2) follow the same trend of pore throat size distribution which would potentially avoid unexpected dissimilarities between the two porous rocks. The MICP data offers a wide range of information, e.g., the pore size distribution, the total pore volume or porosity, the skeletal and apparent density and the specific surface area of the sample (Chatzis and Dullien, 1985). In an MICP test, mercury as the non-wetting phase is injected into a porous rock and, in incremental pressure steps, both pressure and injected volume of mercury are measured. The modified Young-Laplace equation (**Eq. 3.1**), also referred to as the Washburn model, is used to relate the pressure difference across the curved mercury interface to the corresponding pore size.

$$\Delta P = \frac{2\gamma \cos\theta}{r_{pore}} \quad \text{Eq. 3.1}$$

where P is the pressure, γ is the interfacial tension, Θ is the contact angle and r_{pore} is the pore radius. Two MICP tests were carried out on the 10-mm sister plugs of the cores (see marked red parts in Fig. 3-2). The MICP curves shown in Fig. 3-3 indicate the similarity of the pore throat size distributions of both core plugs. The micro-CT imaging acquired in this thesis can give images with a resolution of about $3\mu\text{m}$. The MICP curves reveal that about 95% of the pores are in the range of 3 to $20\mu\text{m}$, suggesting that majority of the pore space can be resolved. The experimental porosities of the samples based on the MICP experiments are 21.3% for plug B1 and 21.0% for plug B2.

3.2.1.1. Preparation of Core Plugs

Once the core plugs had been dried and cleaned, the plugs were coated and cured using a very viscous insensitive seal, Torr Seal (See Fig. 3-4). Torr Seal is a resin seal vacuum leak that can be bond to a variety of materials such as rock, metal and glass. The objective of this coating was to prevent the fluids from bypassing through the rock walls during core flooding. Note that Torr Seal is transparent in the micro-CT imaging.

3.2.1.2. Making Core Plugs Strongly Water-Wet Using Plasma Cleaning

Once the core plugs coated, they were treated by the plasma cleaning for strong and uniform water wettability (Kumar and Fogden, 2009). The treatment subjects the core plug to the cold electric plasma of water vapour. This process removes monolayers and creates a strong hydrophilic surface and improves water-wetness (Kumar, 2009). The core plug is subjected to plasma treating over three 5-min sessions, with a 1-min cooling period in between to avoid any heat build-up on the core plug. The plasma cleaning device is shown in Fig. 3-5. It essentially consists of a vacuum chamber with a radio frequency (RF)

transmitter wrapped around the exterior. Typical operation involves placing a sample within the chamber and evacuating the interior to a pressure of 0.1 Torr. Next, water vapour is admitted into the chamber where the pressure reaches about 0.15 Torr. At this stage, the RF generator is energized; it typically transmits 125 kHz at about 1 kV into the evacuated space (Kumar, 2009).

Kumar (2009) found experimentally that a plasma treated chalk piece became highly water-wet and saturated spontaneous water imbibition to a degree of $\sim 250\%$ higher than before treatment.. Note that the impact of plasma cleaning diminishes in several hours¹, so, for this reason, the coated core plugs were treated just before the actual flooding experiments.

¹Personal Communication with Dr. Michael Turner, Australian National University.

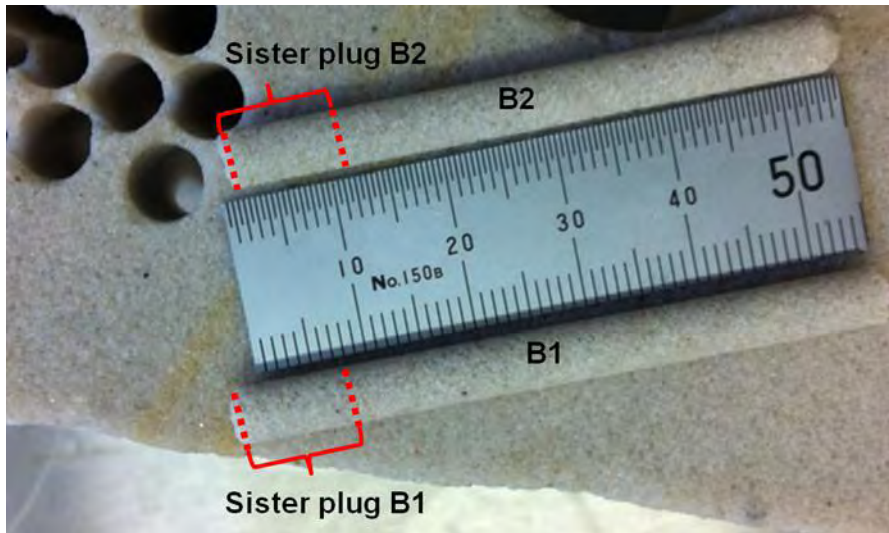


Fig. 3-2, Bentheimer sandstone core plugs used.

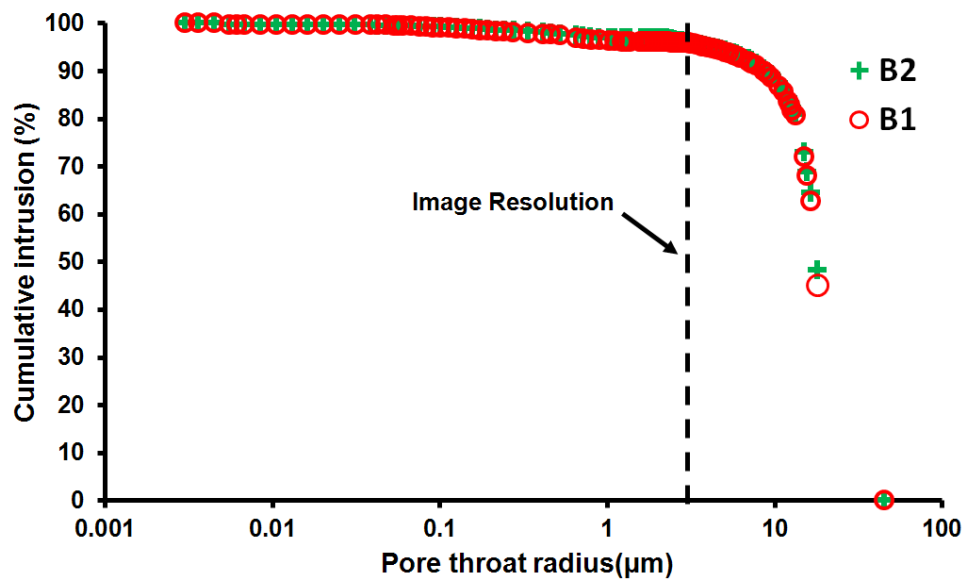


Fig. 3-3, Mercury injection capillary pressure showing the pore throat radius distributions of B1 and B2.

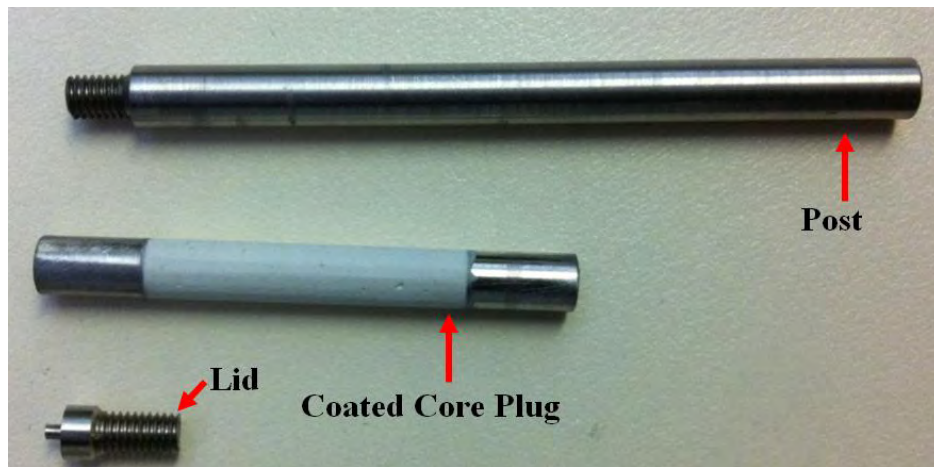


Fig. 3-4, A photo of coated core plug, the post and lid used to hold on the rotation stage of micro-CT facility and seal the sample.

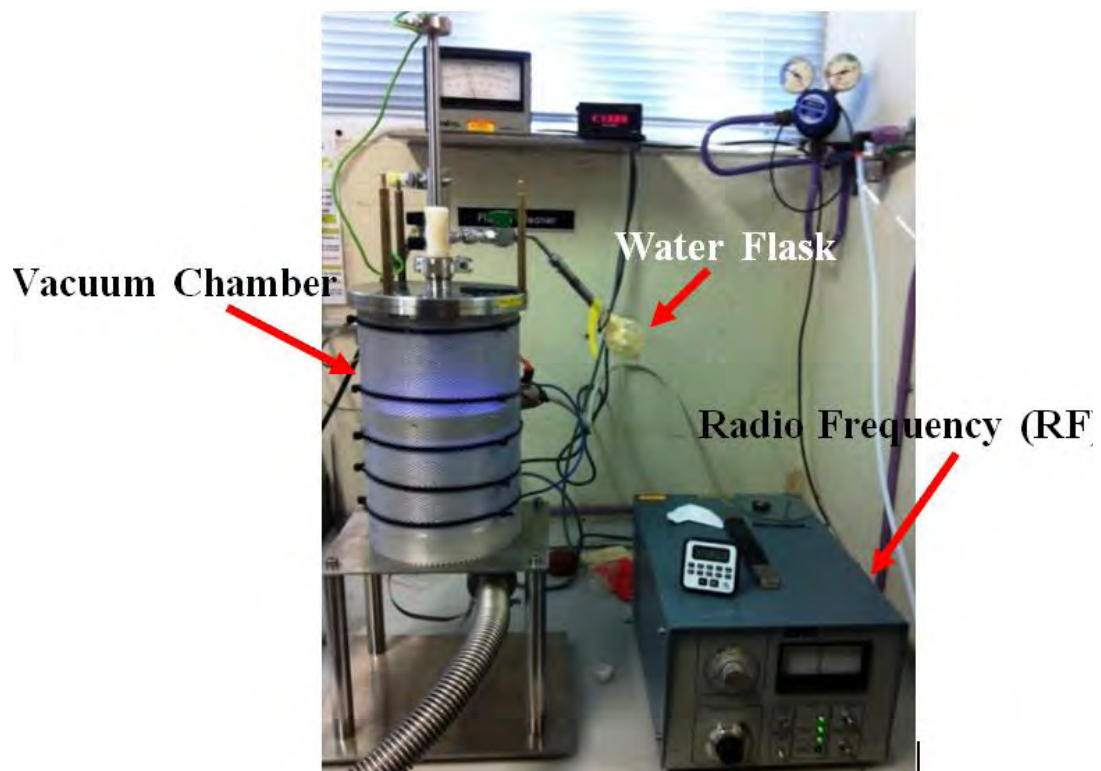


Fig. 3-5, Plasma cleaning equipment at Australian National University, Canberra.

3.2.2. Three-phase Fluids

Air, distilled water and dodecane were used in this study for an immiscible three-phase system. These three-fluid systems were required to provide sufficient X-ray intensity contrast for the phases to be resolved at the limits of image resolution and display positive and negative spreading behaviour. Past work suggests that doping water or oil or both helps to improve X-ray intensity contrast. So, a preliminary study was conducted in order to find out the most appropriate doping chemicals and their optimised ratios for water and oil.

3.2.2.1. X-ray Intensity and Contrast

Caesium Iodide (CsI) and Iodododecane (IDD) were used to increase the contrast between the water and oil phases. The water phase was doped with 0.1 and 0.5M CsI and the oil was doped with 10%, 40%, 50% and 100% by weight of IDD and their attenuation values were measured and compared. The X-ray attenuation coefficient of a pure component (component i) is given by:

$$\left(\frac{\mu}{\rho}\right)_i = x^{-1} \ln\left(\frac{I_0}{I}\right) \quad \text{Eq. 3.2}$$

where μ is the attenuation coefficient, I_0 is the mono-energetic photon density of the incident beam, x is the mass thickness (mass per unit area), ρ is the component density, I is the photon density of the attenuated beam. $\frac{\mu}{\rho}$ (mass attenuation coefficient) values for numerous components have been measured and tabulated by Creagh and Hubbell (1990). The X-ray attenuation values of the doped water and oil phases were calculated using:

$$\left(\frac{\mu}{\rho}\right)_c(E) = \sum_{i=1}^N w_i \left(\frac{\mu}{\rho}\right)_i(E) \quad \text{Eq. 3.3}$$

where w_i is the fraction by weight of the i^{th} component, N is the number of components in the mixture, E is the energy in polychromatic X-ray and $\left(\frac{\mu}{\rho}\right)_c$ is the mass attenuation of the compound. **Fig. 3-6** shows measured X-ray attenuations as a function of X-ray source energies. Pure Iodododecane exhibits the greatest attenuation values over the range of energy while 10% IDD doped oil (IDD-10) displays the lowest value. The CsI doped water mixtures display intermediate attenuation values. The largest contrast in attenuation values between the phases is provided by pure IDD and water doped with 0.1M of CsI.

In order to demonstrate the intensity of each doped fluid, different mixtures of oil and water in small plastic sample tubes were imaged. The results shown in **Fig. 3-7** confirm that IDD and water doped with 0.1M CsI provide the strongest contrast between the phases. The X-ray attenuation values of each mixture obtained from the radiograph are given in **Table 3-1**. The linear attenuation coefficient is an absorption measurement and it is dependent on the thickness and density of a material, atomic number and photon energy. A change in fluid density results in a change of a linear attenuation coefficient even if the same structure is being imaged. From the table, it can be seen that the highest contrast (the highest difference between linear attenuation coefficients) can be achieved using the IDD and 0.1M CsI water.

To determine the best combination of fluids considering the study aim, in a preliminary experiment, a Bentheimer sandstone core plug saturated with pure IDD, 0.1M CsI water and air was imaged. Using pure IDD (the oil phase) caused a beam-hardening artifact in X-ray images due to its high density (see **Fig. 3-8**), although IDD provided the highest contrast. Beam-hardening artifacts occur when the low energy photons are

absorbed leaving the high-energy photons to strike the detectors. When X-ray strikes a high density material such as very high-dense doped oil, lower energy photons are absorbed which results in further hardening of the beam. As the beam becomes harder, the rate at which it is attenuated decreases, so the beam becomes more intense when it reaches the detectors than would be expected if it had not been hardened. Therefore, the resultant attenuation profile differs from the ideal profile that would be obtained without beam hardening. As seen in Fig. **3-8**, it is very difficult to distinguish between the fluids (oil-water-gas) in the image.

Conducting a number of imaging of Bentheimer with different fluids revealed that the best set of three-phase fluids, suitable for the study aims, was 0.1 M CsI water, oil doped with 40% (Dodecane-IDD-40) by weight IDD and air. The CsI in the water phase and Iodododecane in the oil phase improved remarkably the contrast between the fluid phases. In all remaining experimental descriptions, the “water phase” refers to the distilled water doped with 0.1M CsI and the “oil phase” refers to n-Dodecane doped with 40% by weight Iodododecane.

3.2.2.2. Interfacial Tensions and Spreading Coefficient

A pendant drop cell model IFT-10 (Temco Inc., USA) was used to measure the interfacial tensions (IFT) between the three phases. **Fig. 3-9** shows the pendant drop experimental set-up. The cell is a stainless steel cylindrical chamber with two injection orifices (one at the top and another at the bottom of the chamber) where a stainless steel needle is placed for generating a fluid drop or gas bubble. The cell is filled with the heavier fluid of each pair (oil-air, oil-water or water-air) and a droplet of the lighter fluid is dispensed using the needle located in the chamber. The chamber is equipped with sealed borosilicate glass

windows which allow visualisation of the inner space during operation. The camera model G5 (Cannon Corp., Japan) is connected to a microscope (model M420, 1.25 x, Switzerland) located at one side of the visualisation cell and also to a personal notebook to record the inner side of the visual cell using a Cannon remote capture software. Using the camera the image of the hanging drop is captured and then analysed.

The temperature and pressure of the cell were held constant at room conditions (~ 22 °C and atmospheric pressure). A pycnometer, a glass vessel of known volume at a given temperature, was used to measure the density of water (0.1M CsI) and oil phases (n-dodecane-IDD-40). The procedure includes measuring the weight of the dry empty pycnometer, filling the pycnometer with the water-oil phase and measuring its weight again. The weight difference and the given volume are then used to determine the density. The error incurred to density measurements was calculated to be 4.2×10^{-6} using the precision of the weight measurement of 0.0001g (see **Table 3-2**).

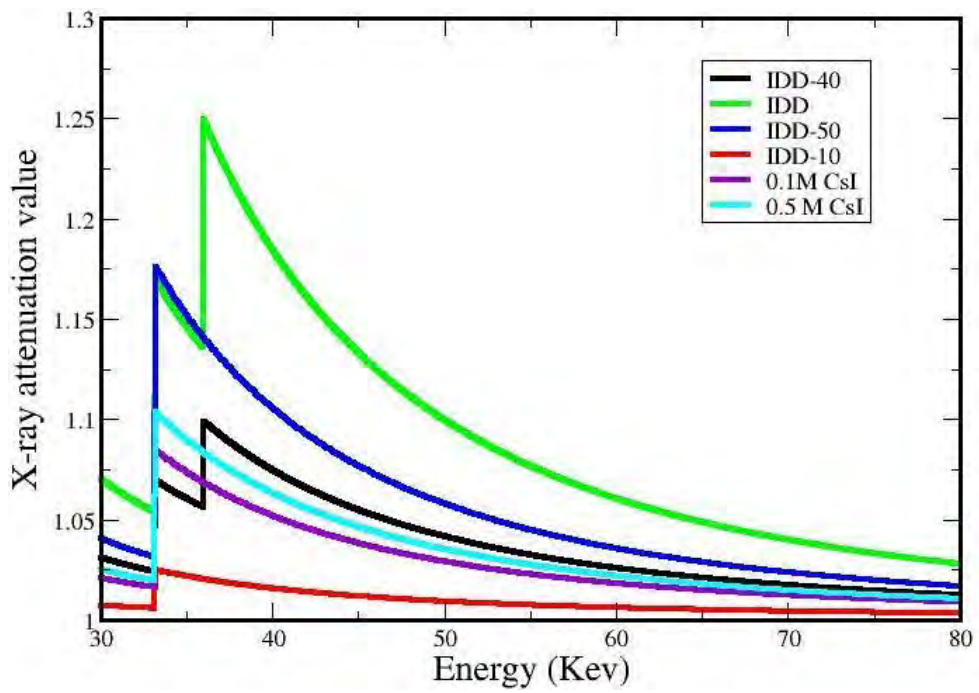


Fig. 3-6, X-ray intensity attenuation value for a range of energy per length scale of 100 μ m.

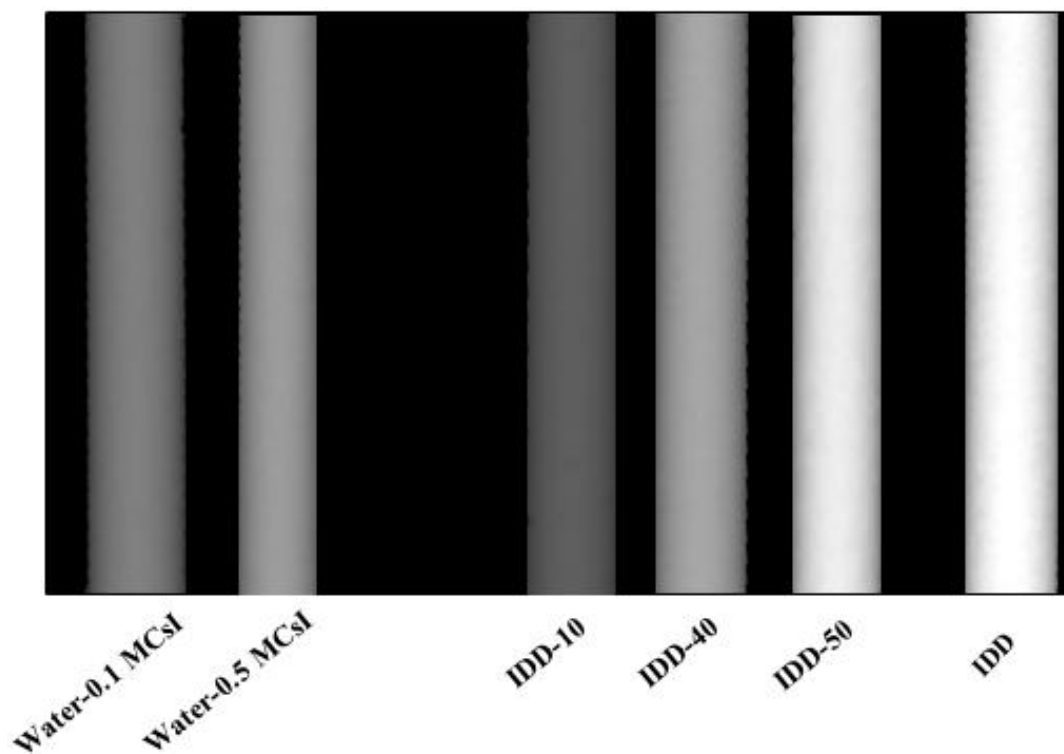


Fig. 3-7, X-ray images of water doped with 0.1 and 0.5 mole of Caesium Iodide (CsI) and n-Dodecane doped with 10%, 40%, 50% and 100% by weight of Iodododecane (IDD).

Table 3-1, X-ray attenuation value

Mixture	Attenuation Coefficient Value
Water-0.1 M CsI	0.8
Water-0.25 M CsI	1
Water-0.5 M CsI	1.4
IDD-10	0.4
IDD-40	1.7
IDD-50	1.9
IDD	2.6

Table **3-2** shows the measured interfacial tensions, densities, experimental errors and the corresponding spreading coefficient of each three-phase system. The higher the density difference between each pair of fluids, the higher experimental error was obtained. The initial spreading coefficient was measured to be $+5.9\text{mNm}^{-1}$. An addition of 10% by volume of n-Butanol to the water phase produced a negative spreading system with a measured spreading coefficient of -8.7mNm^{-1} . Note that the effect of adding this n-Butanol to the doped water phase on the attenuation intensity contrast was not investigated. However, the images of the rocks with negative spreading coefficient presented in Fig. **3-27** demonstrate that the effect, if any, was negligible.

3.2.2.3. *Confirming the Spreading Characteristic of the Fluids using a Glass Micromodel*

Two three-phase fluid systems selected before, were used to perform displacement experiments in strongly water-wet two-dimensional glass micro-models similar to those described by Øren and Pinczewski (1995). The aim was to confirm that the positive spreading system produces oil spreading films and that the negative spreading system does not. The experiments were performed at the ambient pressure and temperature. The experimental procedure for both positive and negative spreading fluid systems was as follows:

The micromodel was first flushed by chromic acid and then rinsed by water to achieve a strong water-wet condition. Strong water-wettability was verified by the visualisation of water and oil interface in the micromodel. The micromodel was flushed with CO_2 to displace the air from the pores and then fully saturated with water. Next, the oil phase was injected into the micromodel at $0.3\text{ cm}^3/\text{min}$ until residual water saturation

was established. Finally, air was introduced into the model until the air breakthrough. A stereo-microscope was used to visualise the three-phase (oil-water-air) distribution in the micromodel. Images shown in **Fig. 3-10** demonstrate clearly the presence of oil spreading films for the positive spreading system and the absence of spreading films for the negative spreading system.

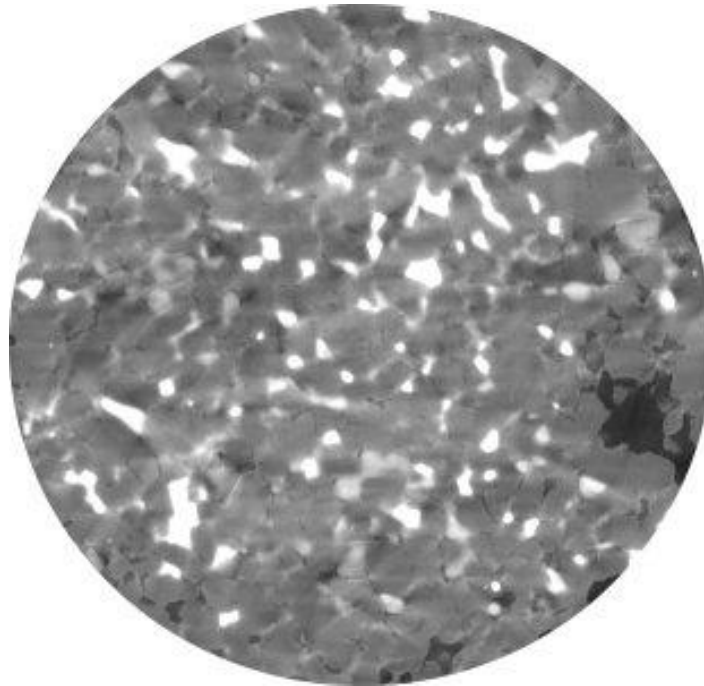


Fig. 3-8, An example of 2D slice from wet tomogram saturated with Iodododecane, 0.1M CsI and air. High density of Iodododecane caused beam-hardening artifact and resulted in a low quality image.

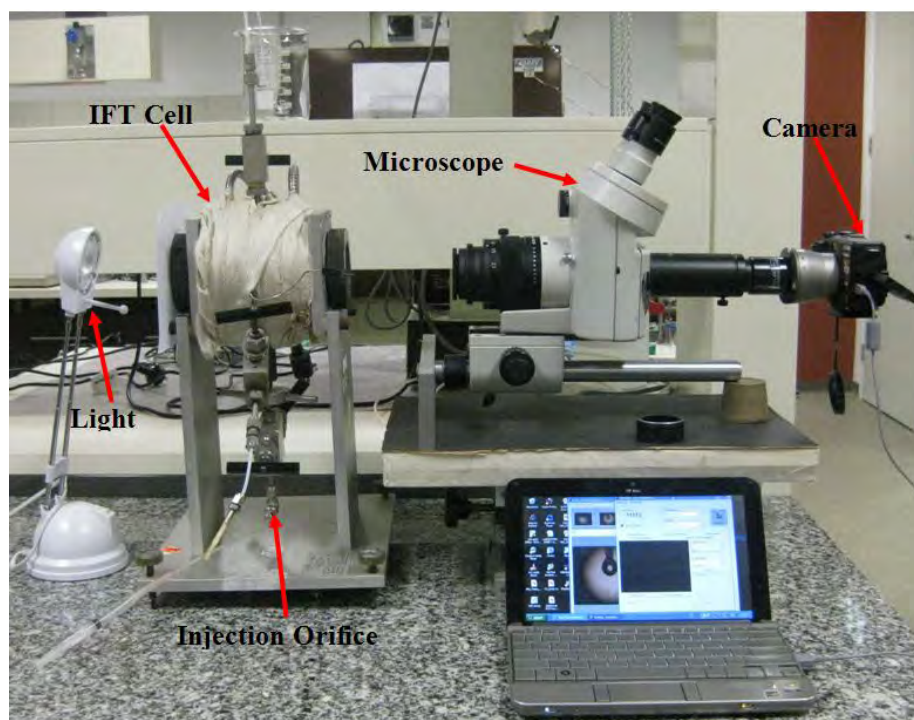


Fig. 3-9, Pendant drop experimental setup.

Table 3-2, Physicochemical properties of the fluids used in the experiment			
Fluid system	$\rho_w(\text{g/cm}^3)$	$\sigma_{wg}(\text{mNm}^{-1})$	$C_s(\text{mNm}^{-1})$
	ρ_o	σ_{og}	
	ρ_a	σ_{ow}	
Water (0.1MCsI)	$1.03 \pm 4.2\text{E-}6$	72.82 ± 3.26	+5.9
Dodecane-IDD-40	$0.87 \pm 4.2\text{E-}6$	31.78 ± 2.64	
Air	0.0012 ¹	35.16 ± 1.29	
Water (0.1MCsI, 10% Vol n-Butanol)	$0.98 \pm 4.2\text{E-}6$	29.41 ± 2.70	-8.7
Dodecane-IDD-40	$0.87 \pm 4.2\text{E-}6$	31.78 ± 2.66	
Air	0.0012 ¹	6.34 ± 0.45	

1: http://en.wikipedia.org/wiki/Density_of_air

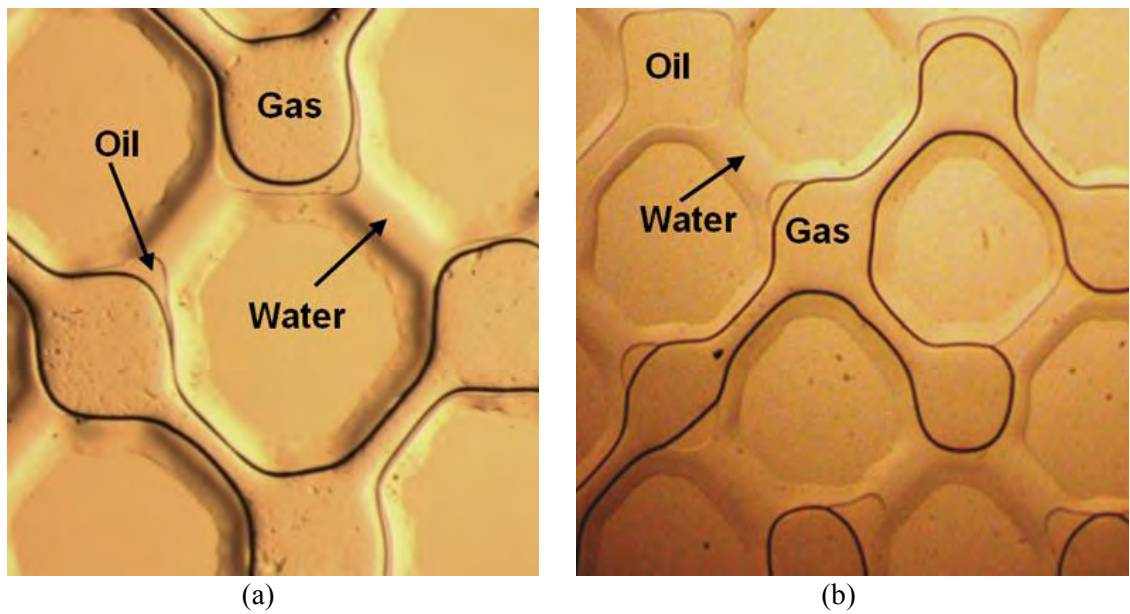


Fig. 3-10, Three-phase fluids distributions in a strongly water-wet glass micromodel for (a) the positive spreading system ($C_s = +5.9 \text{ mNm}^{-1}$) and (b) the negative spreading system ($C_s = -8.7 \text{ mNm}^{-1}$).

3.2.3. Core Flooding

The core flood experiments were performed using the apparatus shown schematically in **Fig.3-11**. The apparatus is composed of two syringe pumps, pressure transducers and a precise scale. The experiments were carried out at ambient pressure and temperature. As explained before, the core plugs were cleaned in the Soxhlet and dried in an oven. Then they were imaged. Just before saturating the cores, the core plugs were plasma treated for strong water-wetness. The saturation of the cores with the water solution (0.1MCsI) was conducted in a desiccator under vacuum. Afterwards, the core was mounted in the flooding system and the water solution was injected at a constant rate of $1 \text{ cm}^3/\text{min}$ into the core to ensure that the core was fully saturated. Next, 1 pore volume (PV) of the oil phase and 0.5 PV of the gas phase at a velocity of 28 cmh^{-1} (Corresponding to a capillary number of 10^{-6}) were injected. The weight of produced fluids was measured at the end of each flood to estimate the average saturation in the core plugs. After a few hours that took during the preparation of the imaging facility for the scanning, the core plug was scanned under the X-ray micro-CT facility.

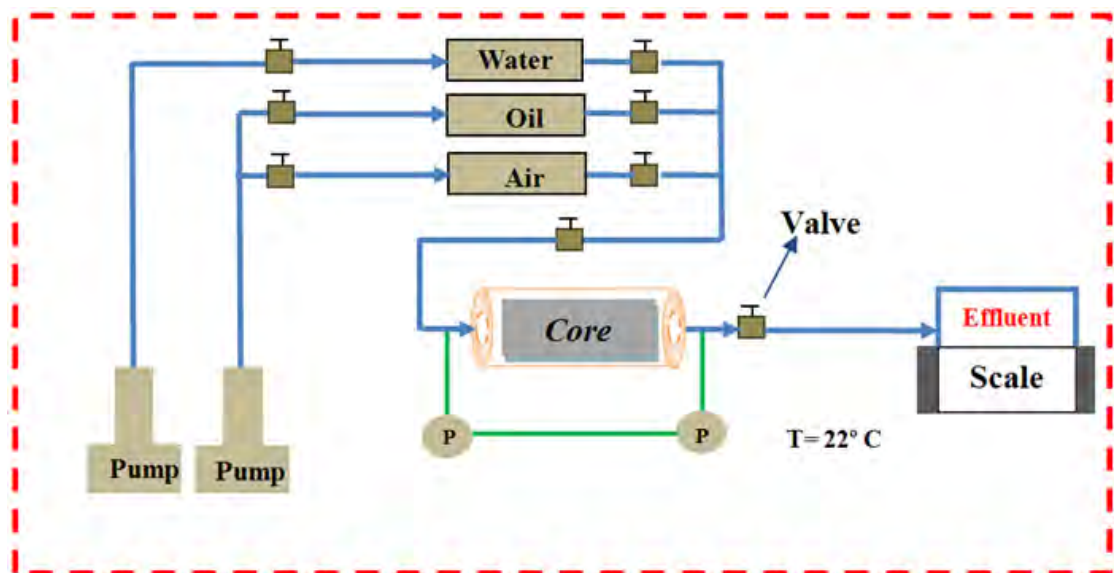


Fig.3-11, Schematic of Flooding Set-up in Lab (T=22° C, Atmospheric pressure)

3.2.4. X-ray Micro-CT Computed Tomography

3.2.4.1. Helical X-ray Imaging Description

The X-ray source, rotation stage and X-ray detector are three main parts of the X-ray instrument. **Fig. 3-12** shows photos of the X-ray instrument setup (at two different angles) used for this study. The X-ray source (GE-Phoenix-Xs160t) generates polychromatic X-rays with an energy ranges from 30 to 225 kV. The stage can rotate and move vertically in front of the source with an angular accuracy of one-thous degree. The detector records X-ray radiographs. The detector is a 400 × 300mm amorphous silicon flat panel with 2048×1536 pixels of size 194μm and a detective quantum efficiency (DQE) in excess of 60% (Varslot et al., 2011b). The rotation stage and the X-ray detector are mounted on a linear rail allowing them to move back and forth independently from the sample and source. This enables one to adjust the magnification and the X-ray image resolution. The instrument can image cylindrical specimens ranging from less than 1mm up to over 100mm in length and diameter.

The geometry of the acquisition of a cone-beam X-ray micro-CT with helical trajectory is depicted in **Fig. 3-13**, where the object is placed on the stage with rotational and vertical translation capabilities. Precision translation, rotation stages and material matching give sufficient mechanical accuracy and thermal stability for sub-micron control of the sample position. Detailed methodology of helical X-ray micro-CT and image processing has been presented elsewhere (Varslot et al., 2010, Varslot et al., 2011a, Varslot et al., 2011b). Four sets of imaging including two dry and 2 wet (saturated with fluids) were performed for two Bentheimer sister plugs (B1 and B2). Some of the main parameters of this X-ray imaging are given in **Table 3-3**.

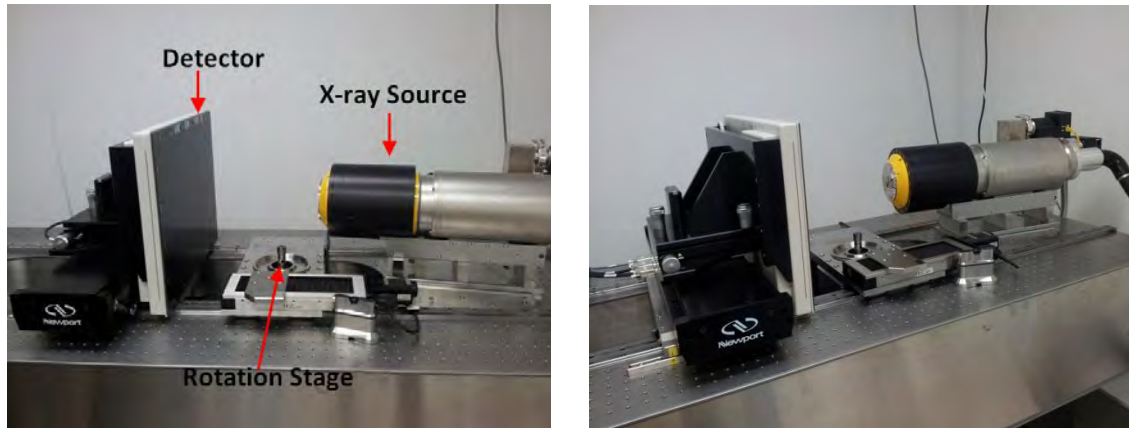


Fig. 3-12, Helical micro-CT system at the Australian National University (ANU). Both detector and sample stage can be positioned independently. The X-ray source is fitted with external cooling to avoid differential heating of the sample during very short sample-distance experiments.

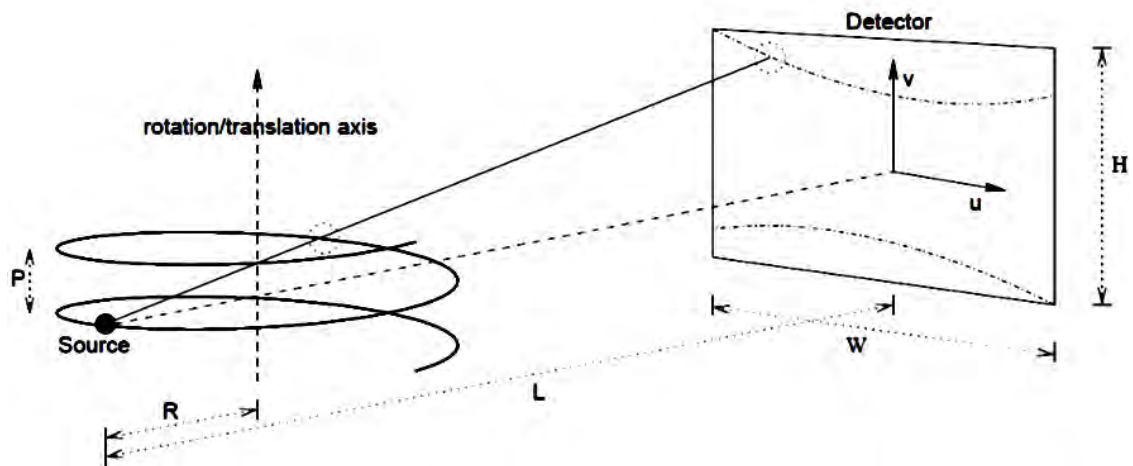


Fig. 3-13, Acquisition geometry for helical cone-beam micro-CT, L is camera length and P is pitch. H and W represent the height and width dimensions of the detector. The diagram taken from (Varslot et al., 2011b).

These parameters and methods were carefully selected after 12 X-ray imaging studies of the samples in order to find a compromise between the filter thickness and X-ray energy to satisfy the study aims (further details will be presented later in section 3.3.1.1). The objective for this exercise was to obtain the highest resolution and the best quality for each imaging which is inherently constrained by the equipment configurations and time restrictions. Imaging of dry B1 was taken with the X-ray source adjusted to 80Kev and 100 μ A. The image was composed of 2048³ voxels with a resolution of 3.46 μ m. Wet B1 was then scanned under a voltage of 100Kev and a current of 120 μ A. B1's wet tomogram was composed of 2048³ voxels with a resolution of 3.97 μ m. The X-ray energy of 100Kev and current of 120 μ A were set with an Aluminum (Al) filter of 1.5mm thickness to image B2 at wet state while it was imaged dry under X-ray energy of 80Kev and current of 100 μ A with Al filter of 1.2mm thickness. Both dry and wet images were composed of 2048³ voxels with resolutions of 3.96 μ m and 4.20 μ m, respectively.

3.2.4.2. Data Acquisition and Reconstruction

To generate dry and wet tomograms of 2048^3 voxels, the core plug was placed on the rotation stage and imaged through 360° in steps of 0.15° ($360^\circ/2,400$) and two revolution cycles. The acquisition time is dependent on many factors such as type and size of the filter used to reduce beam-hardening (Sakellariou et al., 2004a). The acquisition geometry is adjusted to obtain the maximum possible image resolution.

Table 3-4 presents the acquisition data used to acquire the images of the dry and wet samples. The central section (approximately 9 mm) of the sample was imaged using 2,400 projections per revolution. Imaging of the dry sample was taken with the X-ray source adjusted to 80Kev and $100\mu\text{A}$ while those for the wet sample were adjusted to 100Kev and $120\mu\text{A}$. To filter and reduce beam hardening artifact, a 1.2mm Aluminium (Al) rod for dry sample and a 1.5mm Al for wet sample was used.

A pre-processing step is normally carried out to filter cosmic rays, camera pixel defects, which may create ring artifacts, and camera distortions. The projections are then normalised by a clear field projection, different for each experimental run, which gives a projected X-ray absorbance through the material at each point on the detector. This removes malfunction of the detector and creates images of high quality. The projection data are then reconstructed using locally written software by Varslot et al. (2011b) based on the Katsevich technique (Katsevich, 2002a). The Katsevich algorithm can in principal enable reconstruction from data acquired with arbitrarily large cone angle (Varslot et al., 2010) which is the restriction in the Feldkamp-Davis-Kress (FDK) algorithm (Feldkamp et al., 1984) due to the limited cone angle to about $\sim \pm 5^\circ$. The Katsevich method is the first workable reconstruction method for helical cone-beam tomography (Wildenschild and Sheppard, 2013) that uses the theoretically exact inversion formula which is truly of the

filtered back projection type , in which “the data are first convolved with a filter and each view is successively superimposed over a square grid at an angle corresponding to its acquisition angle”(Ketcham and Carlson, 2001). This means that the formula can be numerically implemented in two steps including shift variant filtering of a derivative of the cone beam projections and then the result is back projected in order to form an image. The detail of reconstruction is outside the scope of this thesis and more detail can be found in references (Katsevich, 2002a, Katsevich, 2002b). All the data were processed at the Australian Partnership for Advanced Computing (APAC) national facility. It took 200-300 minutes on 128 CPUs to generate a 2048^3 voxel tomogram using 60 GB RAM.

Table 3-3, X-ray imaging parameters used for dry and wet B1 and B2 samples

Sample / State	E _v (Kev)	E _c (μA)	Filter/ Thickness	Resolution(μm)	Time(hrs)
B1-Dry	80	100	Al 1.2mm	3.46	21
B1-Wet	100	120	Al 1.5mm	3.97	17
B2-Dry	80	100	Al 1.2mm	3.96	21
B2-Wet	100	120	Al 1.5mm	4.20	17

Table 3-4, Acquisition data for dry and wet X-ray imaging

Sample	CL (mm)	SD(mm)	Energy (Kev)	Current (μA)	Filter (mm)
Dry	500	9	80	100	1.2 Al
Wet	400	8	100	120	1.5 Al

The resultant tomographic image is a cubic array of volumetric pixels termed voxels. Each voxel has a linear attenuation value in a 16-bit grey-scale. The reconstruction process reverses the relationship between grey-scale and X-ray absorption. This means that the higher the X-ray absorption, the brighter the components will appear. In other words, the reconstructed tomograms represent the density map of the sample. Therefore, the grey-scale values correspond to the density and composition of the imaged material.

3.3. Micro-CT Image Analysis

To investigate the three-phase (oil-water-gas) distribution and spreading films of oil and water using X-ray images, it is required to develop and optimise a specialised X-ray scanning procedure. The objective is to maximise the contrast between the phases (oil-water-air) to ensure the oil and water small features are detectable and resolvable while minimising or eliminating artifacts that can interfere with qualitative and quantitative analysis. The optimisation of X-ray imaging parameters according to the study aim is described. This in turn helps to enhance the qualification and quantification analysis of three-phase fluids using the X-ray images.

3.3.1. Image Enhancement and Optimisation

There are several characteristics that affect the quality of X-ray images. These are spatial resolution, contrast resolution, linearity, noise and artifacts. Enhancing or suppressing any of these characteristics depends upon the X-ray imaging aim and interest (Reddinger, 1998). Referring to the aim of study, there has to be a balance between these characteristics and parameters to produce the best possible X-ray image. There is, however, always a

trade-off when CT parameters are manipulated and there must be a goal-oriented approach to obtain the best X-ray image quality.

In this section, some of the important parameters affecting the quality of the X-ray images and how they control artifacts are discussed. The precautions taken to eliminate or mitigate those possible sources of error are presented. The enhancement step, after X-ray imaging, is also described.

3.3.1.1. Contrast Effects, Artifacts and Films

X-ray computed tomography uses the difference in X-ray attenuation to provide information about the component and structure of a material in a non-destructive way. The amount of attenuation (absorption contrast) depends on elemental composition of material, density and thickness of material. In an absorption contrast tomogram, the value associated with each voxel is proportional to its X-ray attenuation (Wildenschild and Sheppard, 2013). As described previously, the oil and water phases were doped with 40% by weight IDD and 0.1 M CsI that provided sufficient discrimination of X-ray intensity value. This strong absorption contrast is the reason behind the visualisation of oil and water features (films) at the length scale less than the resolution of the images (voxel-size). Although this effect can make X-ray images more problematic to interpret quantitatively due to subsequent artifacts, this also offers an opportunity to extract fine-scale features in the image. The water or oil films around the gas phase below the image resolution (voxel size) blur the sharp edge (“fuzzy”) at the interfaces of the air-rock or air-water and appear with contrast bright bands. This is the key to indicate the presence of spreading water and oil films in the images. Nevertheless, film signal-to-noise ratio (SNR) must be high enough so the films can be distinguishable.

Substances' properties including density, atomic number and the energy of the incident X-rays not only change the intensity attenuation of X-ray, but also alter the phase of the X-ray passing through the object, similar to a lens for visible light, (De Witte et al., 2009), leading to X-ray refraction. When going to high resolution, the contribution of this phase signal to projection image is no longer negligible and appears as bright (when X-ray converging) or dark (when X-ray diverging) fringes on the edge of features (Mayo et al., 2003, Wildenschild and Sheppard, 2013). This is termed "phase contrast". This artifact (bright fringes or contrast band) could be important here as it might affect the interpretation of films in the images as oil or water. In addition, it can make quantitative analysis (segmentation) of the image challenging.

To suppress or reduce this artifact which can be the source of error for image analysis, the parameters being imposed on the intensity of this artifact are manipulated. The propagation distance, X-ray energy and amount of filtering are three factors that affect the phase contrast fringes²(Arhatari et al., 2004, Arhatari et al., 2005):

1. The primary reason for the strong fringing artefacts is because the propagation speed (i.e. the phase speed) is lower in the doped-fluid than in the grain, yet there is more attenuation in the doped-fluid. So the speed causes the X-ray beam to move towards the doped-fluid, causes dark fringes near the edge of what is otherwise a bright region in the reconstructed tomogram.
2. Effective propagation distance (given in **Eq. 3.4**): Longer propagation distance results in more pronounced phase contrast fringes.

²Personal Communication with Dr. Andrew Kingston and Dr. Adrian Sheppard, from Australian National University.

$$PD = \frac{CL - SD}{M} \quad \text{Eq. 3.4}$$

where CL is the camera length (the distance between camera and X-ray source), SD is the specimen distance between the specimen and X-ray source and M is the magnification($M = CL/SD$).

3. Energy or wave number: Increasing the energy reduces the diffusion of the fringing effects perpendicular to the propagation direction and hence reduces their visibility for a given propagation distance.
4. Filter: Filtering can be effective in causing the broad polychromatic spectrum to approach a high energy monochromatic wavelength. So, in this case, the less polychromatic the radiation the less phase contrast fringing.

In this study, to obtain the finest image voxel size, the highest possible magnification was set which, in turn, the highest propagation distance was required. Increasing the energy reduces fringing effect and its visibility. The amount of filtering can increase the effective beam energy by removing low-energy. For example, higher X-ray energy and thicker filtering leads to reduced fringes (contrast band) at the edges on the X-ray images. However, this might result in losing the image resolution by reduction of amount of signal-to-noise ratio. **Fig. 3-14** shows a comparison of the effect of the X-ray energy and filtering on the image of Bentheimer core plug saturated with IDD-40. Fig. **3-14(a)** shows a section of the wet image taken with the X-ray source adjusted to 80Kev and a 1.2mm Al filter while the image in Fig. **3-14(b)** adjusted to 100Kev and a 1.5mm Al filter. As it is visually evident, the fringes reduced significantly when the energy and filtering increases from 80KeV to 100KeV and 1.2mm Al to 1.5mm in thickness, respectively.

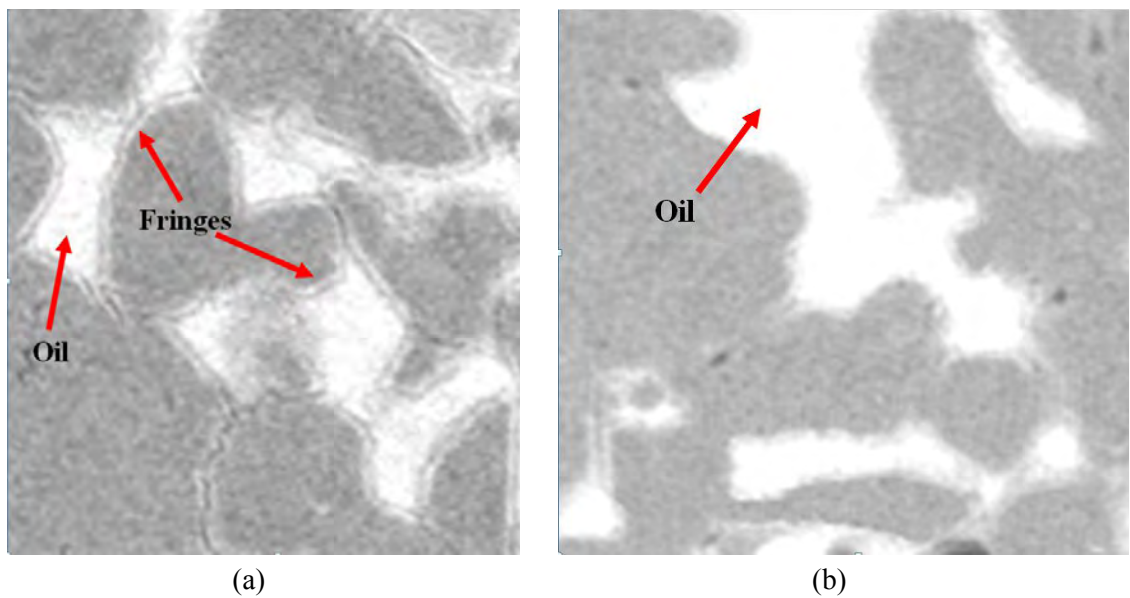


Fig. 3-14, Comparison of phase contrast fringes (a) Imaging at 80Kev and filtering with 1.2mm Al (b) Imaging at 100Kev and filtering with 1.5mm Al. The halos are reduced significantly using higher energy and thicker filter.

3.3.1.2. Anisotropic Diffusion Filter

There are always random signals that do not contain information superposed on actual data known as noises, created from different factors such as fluctuation in beam intensity, fluctuation in power and also insufficient photon flux from the X-ray source (Reddinger, 1998). Image noises degrade the image quality which consequently affects the resolution of the sense of the ability to observe separate features in an image. This concern makes it essential to reduce noise and enhance the image quality.

The anisotropic diffusion (AD) filter, an iterative edge-preserving noise reduction, has shown to improve the signal-to-noise ratio of tomographic images in a variety of contexts (Sheppard et al., 2004). Wavelet transform altering (Mallat, 1989) and nonlinear anisotropic diffusion (Perona and Malik, 1990) have emerged as the two most effective alternatives. Wavelet transforms are a very powerful tool for one-dimensional (1D) signal processing, but do not extend naturally to higher dimensions. Invariant wavelets (Coifman and Donoho, 1995) and curvelets (or ridgelets) (Candès and Donoho, 1999) have been proposed as extensions to 3D problems, but they have been found to be less effective than coherence-enhanced anisotropic diffusion (Weickert, 1999) for images where signal frequencies lie below half the Nyquist limit (Frangakis et al., 2001). The Nyquist limit is a theoretical limit showing at what rate a signal containing data is to be sampled with a certain maximum frequency. A signal sampled higher than the Nyquist limit results in a wave of lower frequency, which creates an aliasing artifact.

Using the AD filter is advantageous because it conserves the integrated image intensity and preserves the image's significant features and edges while removing most of the image noise (Sheppard et al., 2004). This technique smooths uniform regions representing homogeneous materials and enhances the boundaries with efficient noise

reduction while “persevering” signal. **Fig. 3-15** shows the same sections from the wet tomogram of Bentheimer sandstone before and after application of AD filter. The filter was carefully applied to remove image noise without changing the pore-solid boundaries. It is clear that the filter has significantly reduced the noise while having preserved the integrity amongst the phases.

3.3.2. Image Registration

The image registration technique allows aligning the geometry of the sample images before and after the invasion of fluids taken at different times. This enables to observe and discuss the fluids configuration in porous rock before and after flooding. It also prevents the overestimation which might be ended to an imperfect segmentation due to ambiguity at the boundaries of grain-fluids. The image registration technique also decreases the difficulty of the segmentation of a wet image containing oil, water and gas phases by reducing the ambiguity associated with the solid phase.

In this study, to describe qualitatively the fluid distributions and films and also to analyse quantitatively their spatial occupancy and connectivity, it was essential to differentiate amongst the fluids and solid. However, in the wet image, the fluids-solid boundaries were blurred due to the contrast reduction of high opaque fluids. This became more complicated when extra filtering was applied to avoid the phase contrast fringes and to reduce the beam hardening where the sample was saturated with high opaque fluids. This impediment could be overcome by a 3D voxel-to-voxel alignment of the dry and wet tomograms (partially-saturated tomogram) and then masking the flooded image with the solid phase obtained from the dry image (Latham et al., 2008).

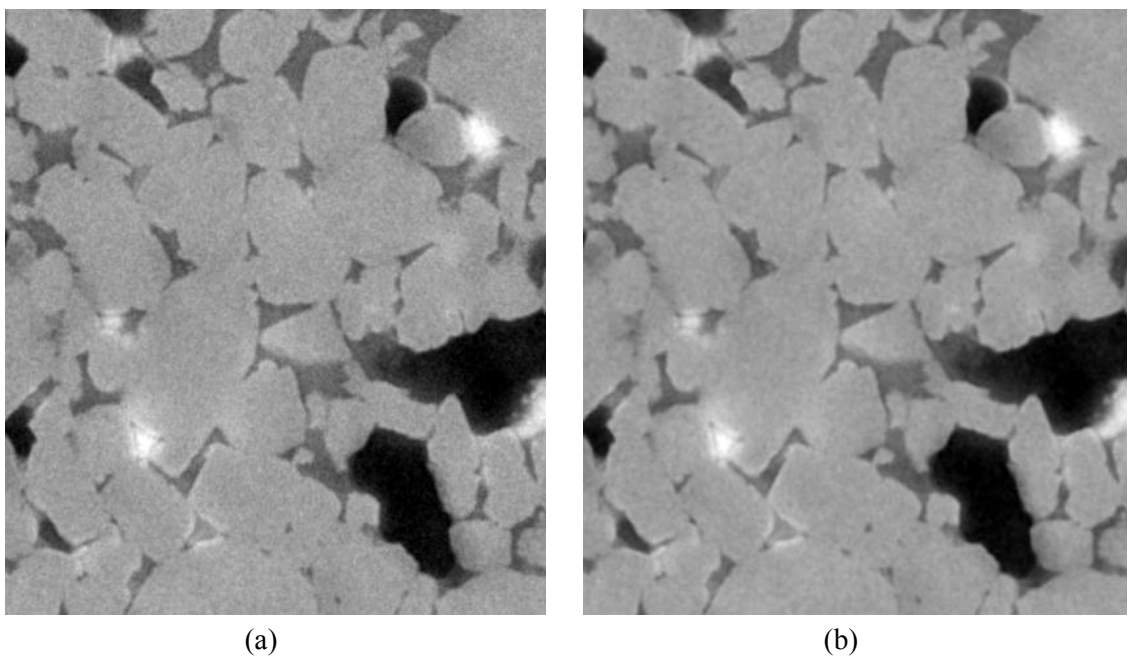


Fig. 3-15, Sections from a wet tomogram of Bentheimer sandstone (a) without the AD filter (b) with the AD filter.

The 3D dry-to-wet registration technique developed by Latham et al. (2008) was used and this assisted to align the spatial dry and wet images together so that corresponding features could overlap. This technique solves an optimisation problem with respect to several similar parameters including three translational, three rotational and one isotropic scaling (Latham et al., 2008). **Fig. 3-16** shows registered sections of dry and wet tomograms. As shown, from comparison of the registered dry and wet images, the fluids occupancy is distinguishable and therefore quantifiable. A comparison of dry and wet images demonstrates that the use of the 3D dry-to-wet registration technique allows pore-solid boundaries to be defined precisely. This technique (1) enables the porous system of the dry image to be used in place of the porous system of the wet image as well as (2) helps to clarify subtle changes in the porous system.

An extreme care was paid during the imaging of the core plugs in order to avoid any movement of the plug. This was important because even a slight voxel movement could cause serious issues with the quality of the reconstructed images and subsequent registration of the dry and wet images. A setup was built which holds the core plug rigidly throughout the X-ray scanning experiments without any detectable movement.

The top of the post was screwed into the bottom of the core plug and the bottom of the post was screwed into the centre of the rotation stage. The lid was also screwed into the top of the sample. This allowed for the free rotation of the entire setup preventing any shifting. The duration of the X-ray acquisitions was approximately 17-21hrs for both wet and dry images. It was essential to ensure a perfect sealing of the wet sample to avoid any evaporation. This requirement was met using the setup shown in **Fig. 3-4**.

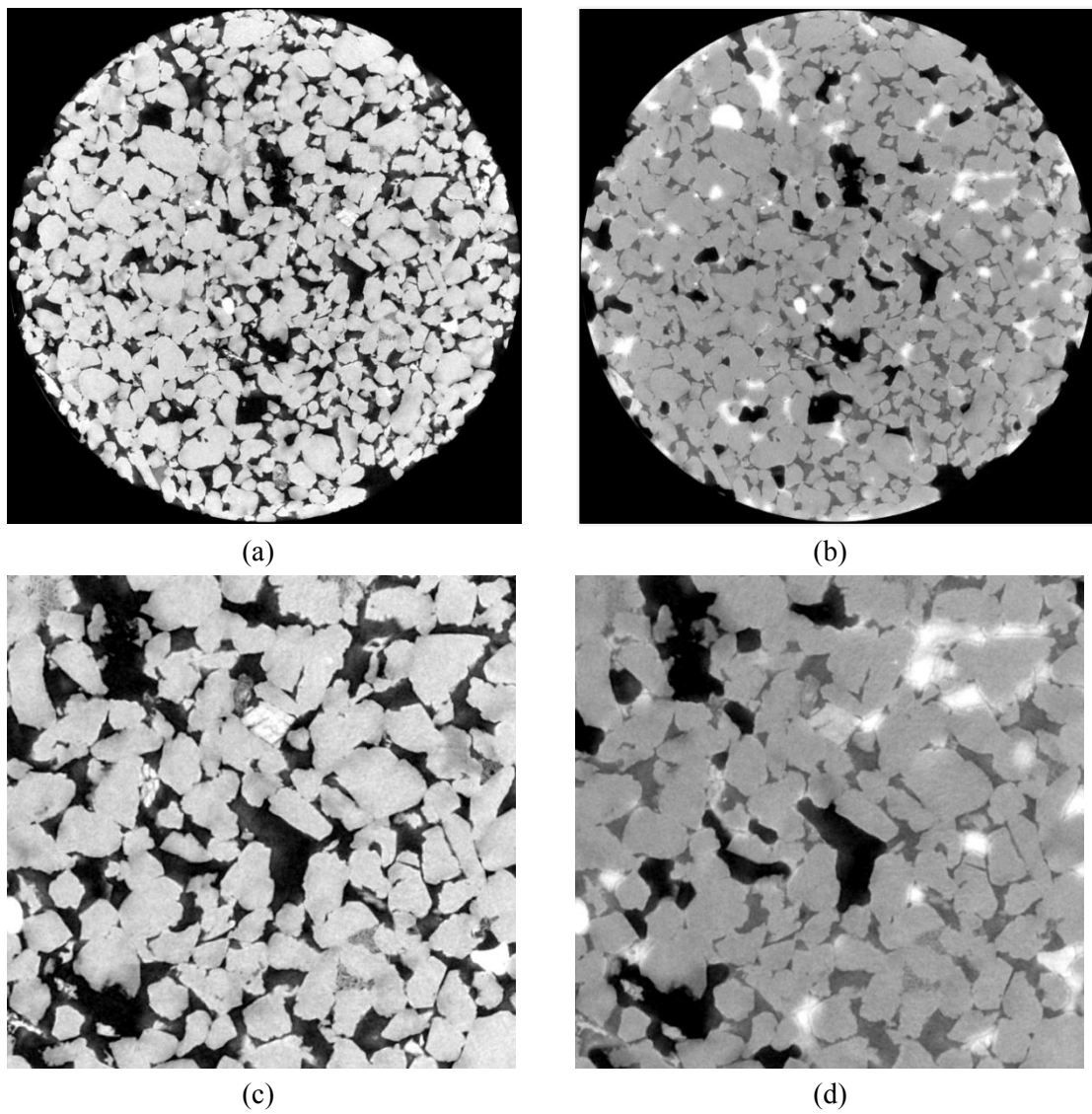


Fig. 3-16, Examples of registered 2D slices of Bentheimer sandstone (a) dry image (b) wet image containing water, oil and air (c) – (d) magnified view of registered dry and wet images. The oil is shown in bright, water in dark grey and gas in black.

Although extreme care was taken to scan the same location of the dry and wet core sample, there was always an inevitable slight vertical difference between the scanned areas. Uncommon slides in the images could not be registered and therefore masked out.

Given the voxel size or less voxel size of films (oil-water), registered images must be perfectly overlaid voxel-to-voxel. This means that even a voxel difference between the dry and wet sections can be interpreted as films, leading to a wrong interpretation and quantification error. To prevent this, registered sections that had such a slight difference (a voxel size difference) were masked out of the images. It was therefore not possible to use the global registration of the images and only small part of the overall images was registered and used for further analysis. This however did not cause any problem in the results considering aim of the study.

3.3.3. Image Subtraction and Renormalisation

To obtain the local pore occupancy of the oil and water phases and to determine whether or not the oil phase is presented and connected throughout the tomogram regardless to fringes artifact in the images, a technique of subtraction map of the dry and wet tomograms was developed and used. This was followed by the registration technique where one can visualise the difference of two tomograms before and after an invasion of fluids. A dry tomogram is composed of voxels which belong to pore, solid and clay. After the invasion of water, oil and air in the dry sample, the X-ray intensity value of voxels which belong to the solid area should remain constant because solids are insensitive to opaque fluids. But, the voxels which belong to the pores should now be composed of three different intensity values; water, oil and air. The subtraction map was achieved by subtracting the intensity value of the voxels of the dry tomogram from the intensity value

of the voxels of the wet tomogram. This should not fail since the experimental setup for imaging was designed to prevent even negligible movement of the sample. Further to this, the alignment related issues were adjusted during the reconstruction process. As a result, two tomograms share the same alignment parameters. **Fig. 3-17** shows a schematic of the intensity values for dry, wet and difference tomograms. In the dry tomogram, the yellow region represents only the intensity distribution of the pore. Having the dry sample saturated with three phases the same area represents the intensity distribution of the three phases; oil, water and air. As shown in the difference tomogram (**Fig. 3-17**), the region marked with a striped pattern indicates the intensity value of zero. Note that the solid and air remain unaffected by saturation. The regions with red and blue colours, after subtraction, change to orange and sky blue which illustrate the intensity variation in the difference tomogram.

The key point here is the relationship between the intensity value of the dry and wet tomograms which should be linear and relatively consistent. This failed due to various conditions of the experiments for dry and wet imaging or after the reconstruction process. As described in section 3.3.1.1, in order to reduce the phase contrast fringes, a higher range of X-ray energy was required to scan the wet sample which caused it to have a lower range of intensity distribution. This became more complicated when extra filtering was applied to avoid beam hardening and reduce fringes where the sample was saturated with highly doped-oil (see **Fig. 3-18**). To illustrate this, when the wet sample was imaged, X-ray energy of 100Kev and current of 120 μ A were set with an Aluminium (Al) filter of 1.5mm thickness. By contrast, when the dry sample was imaged, X-ray energy of 80Kev and current of 100 μ A were set with Al filter of 1.2mm thickness. The two configurations produced different intensity values for dry and wet images. Another possible explanation for this discrepancy is the result of the reconstruction process. Given the various materials

present in the tomogram, normalisation is achieved by the reconstruction process (Sakellariou et al., 2004a, Sakellariou et al., 2004b). This implies that the range of attenuation coefficient values assigned to a low density material would be suppressed when imaged in the presence of very high density material such as high doped-oil as opposed to when imaged alone. This is demonstrated in Fig. **3-18(a)** by a grey-scale slice through a 3D dry tomogram and its corresponding intensity histogram Fig. **3-18(b)**. The same grey-scale slice, shown in Fig. **3-18(c)**, is from a saturated tomogram containing oil, water and gas and its corresponding intensity histogram Fig. **3-18(d)**. The intensity distribution of air and solid in the wet tomogram shifted to the right when compared to the intensity distribution of air and solid in the dry tomogram. Under ideal circumstances, the solid and air intensity values should have been similar before and after the invasion of fluids.

The difference between the intensity distributions of dry and wet images for solid and air were observed for all experiments carried out in this study. The simple illustrative procedure shown in Fig. **3-17** suffers from the fact that the relationship between the intensity coefficient values of the dry and wet images are inconsistent and non-linear which results in a non-zero intensity value of solid and air in the difference tomogram. This, however, contradicts the objectives of the subtraction method in which mutual phases (solid and air) in the dry and wet tomograms are eliminated with oil and water remaining. This problem was solved using a rescaling technique where the intensity values of both pore and solid in the dry tomogram renormalised based on the values of air and solid in the wet tomogram. In this method, given the intensity histogram, the peak intensity values of the pore and solid in the dry tomogram are determined and labelled as I_p^d and I_s^d , respectively and the peak intensity values of air and solid in wet tomogram are also determined and labelled as I_a^w and I_s^w , respectively. Rescaling is performed using the following formula:

$$NF = \frac{I_s^w - I_a^w}{I_s^d - I_p^d} \quad \text{Eq. } \beta.5$$

and

$$C = \frac{I_a^w I_s^d - I_s^w I_p^d}{I_s^d (I_s^d - I_p^d)} \quad \text{Eq. } \beta.6$$

where NF is the normalisation factor and C is a constant obtained using the intensity values of the original data set. Then, these factors are applied to the original intensity values of the dry tomogram according to the formula below:

$$I_N = I_O \times NF + C \quad \text{Eq. } \beta.7$$

where I_N and I_O are the intensity distributions of the rescaled and original tomograms, respectively. This was done using a processing software developed at Australian National University, called as Qmango, which is capable of parallel processing on a super computer. The 2D slices of the dry and saturated data sets are shown in **Fig. 3-19**; (a) dry image (b) and saturated image. Using the above methodology, the difference slice achieved is shown in (c). As can be seen evidently, the solid, pore and air are removed in the difference slice as they shared similar intensity values. The intensity distributions of the original dry and wet images as well as the normalised dry image is shown in **Fig. 3-19(d)**. The method provided a good match between the intensity values of the pore and solid from dry image with the intensity values of air and solid from the wet image. **Fig. 3-19** confirms this methodology where oil (bright) and water (grey) in the subtraction slice correspond to the oil and water phases in the wet slice. This technique was used to provide qualitative descriptions of the data sets representing 3D tomograms of samples B1 and B2.

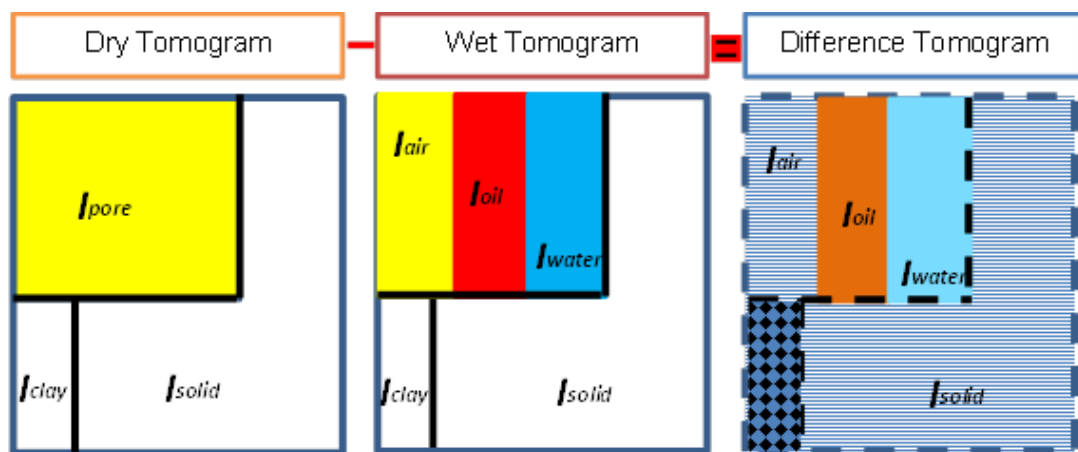
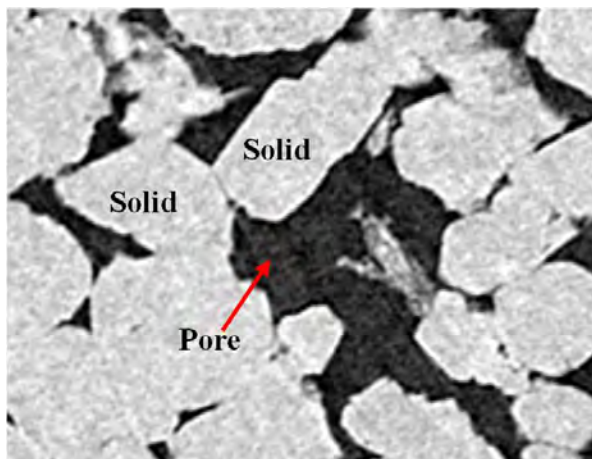
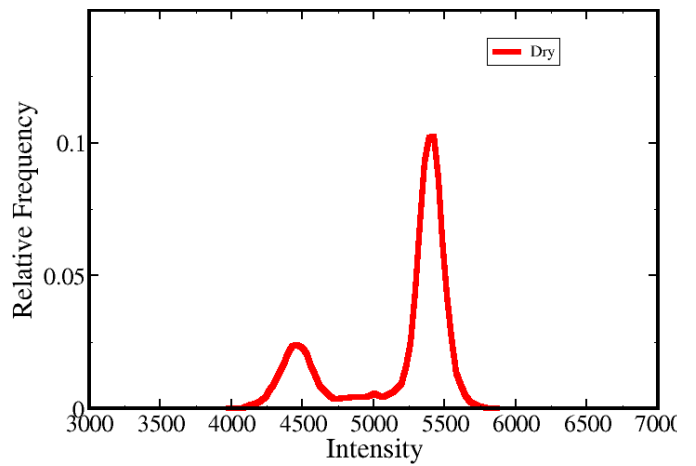


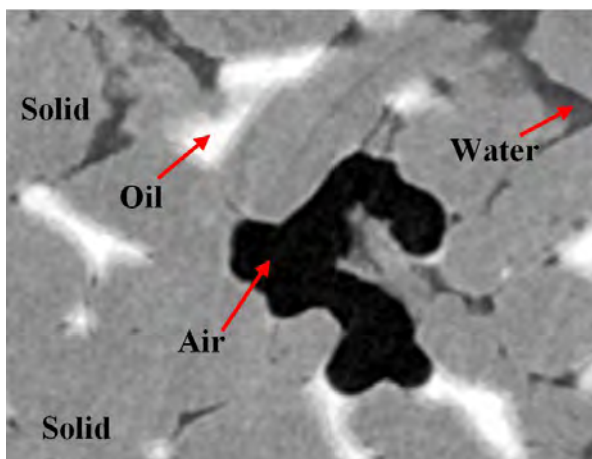
Fig. 3-17, A schematic of the coefficient value of dry and wet tomograms and the subtraction result. In the difference tomogram, the solid and air regions (marked with a striped pattern) represent a zero intensity value. The intensity value of the oil and water regions (marked in red and blue) remains constant as shown in the subtracted tomogram. The clay in the wet tomogram is saturated with water. After subtraction, the water value remains unchanged, while the clay value becomes zero.



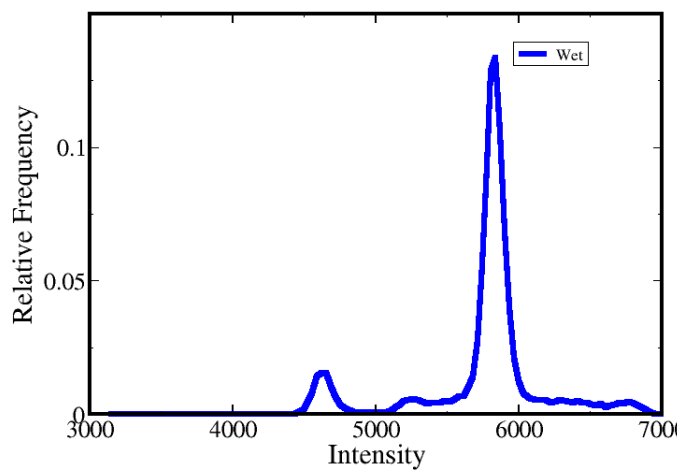
(a)



(b)



(c)



(d)

Fig. 3-18, (a) An example of registered grey-scale slice of dry tomogram containing pore (black) and grey (solid) and (b) Corresponding intensity histogram (c) Registered grey-scale slice of wet tomogram containing air (dark), solid (grey), water (dark grey) and oil (bright) and (d) Corresponding intensity distribution.

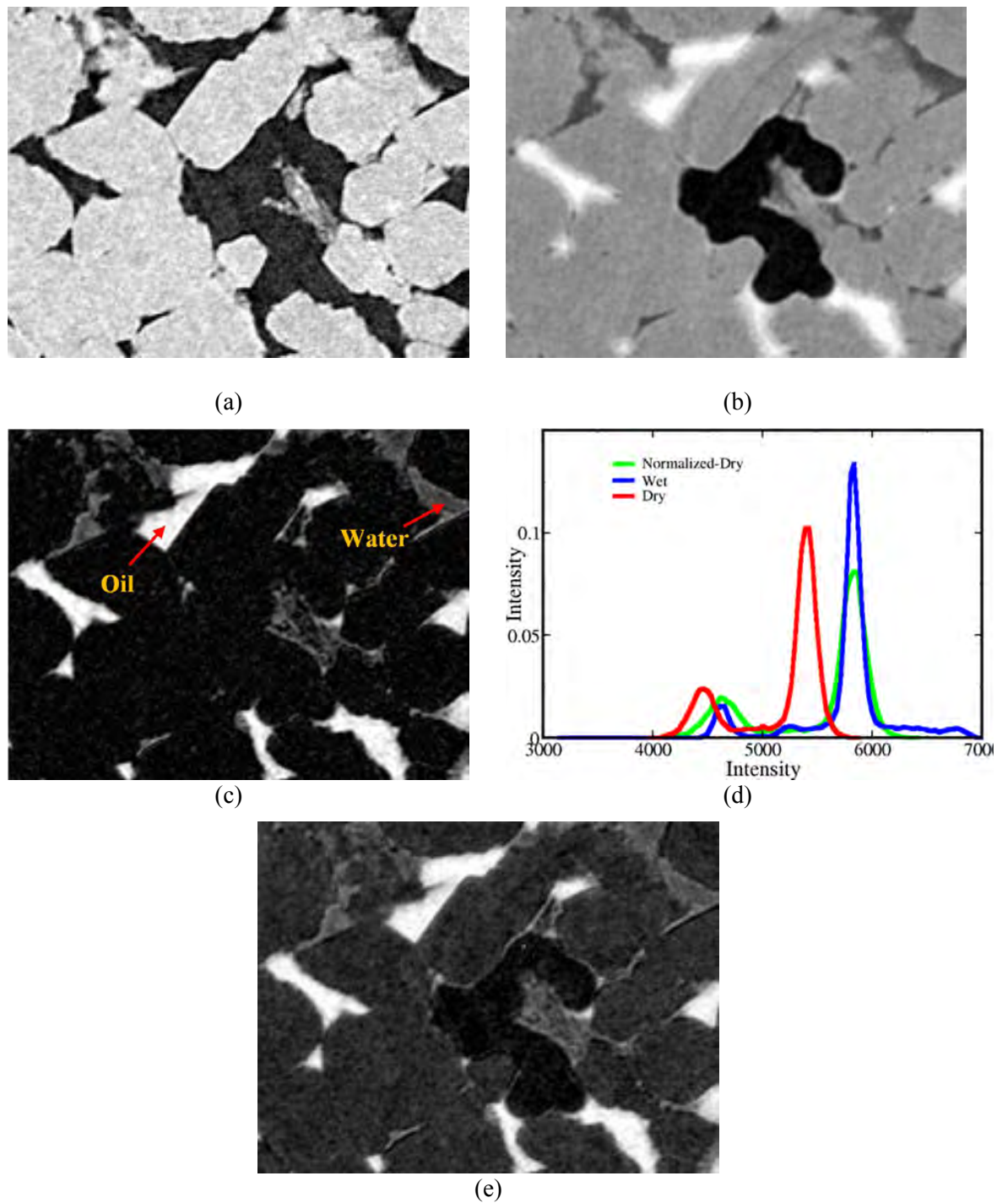


Fig. 3-19, (a) An example of dry slice showing pore(black) and solid (grey) (b) Wet slice containing water (dark grey), oil (bright), solid (grey) and air (black) (c) Subtraction containing water (dark grey) and oil (bright). (d) Intensity distribution of original dry (red), wet (blue) and normalised dry (green) images. The entire intensity histogram of dry image is shifted to right according to NF and C factors. (e) Subtraction without renormalisation of dry image.

Fig. **3-19** (e) shows the difference slice achieved without any implication of renormalisation on dry image. As can be seen, the solid is not removed and caused significant noise particularly at solid-pore boundaries which may be considered as films. Thus, in this case the amount of uncertainty has increased due to the presence of solid and air phases. This is not the case in a renormalised difference slide and the solid and air are no longer the problem and, as a consequence, the amount of the uncertainty in image analysis has significantly reduced.

3.3.4. Image Segmentation

A tomographic image is reconstructed from cubic array (voxels) of X-ray attenuation values of each component. Note that, here, different components in an image are termed as the phase. In general, segmentation means to divide an image into several regions according to some a number of consistent principal. This principal is voxels classification on the basis of three-dimensional attenuation profile of dissimilar objects in the images such as pore, grain and etc. As segmentation is a subjective process, it includes more likely uncertainty rather than other steps of image analysis. Thus, it is indispensable to have a well-defined and consistent method to segment an image. There can be, however, different segmentation strategies for different sets of image data. In this study, the CAC-Sheppard, which is a hybrid method developed by Sheppard et al. (2004) for 3D grey-scale images, was used to perform segmentation. This method utilise a combination of image enhancement, thresholding and converging active contour (Vincent and Soille, 1991, Caselles et al., 1997).

A special software, developed at Australian National University and called as Mango, was used for parallel segmentation, pre-processing, post-processing and analysis of

associated data (See Middleton et al., Mango User Guide for applied mathematics, Department of Applied Mathematics, available at <http://xct.anu.edu.au/mango/>)

3.3.4.1. Dry Image

The CAC-Sheppard method, the initial approach involves the choice of two low and high thresholds and this divides the regions into two classified and one unclassified regions. All voxels with values less than the low threshold are labelled as “pores” and all voxels with values above the high threshold are labelled as “solids”. Those with values in between these thresholds were classified as undecided voxels. After initial thresholding, converging active contour algorithm expands the decided regions within the undecided region towards one another. The final region boundary is automatically placed at the points where two contours touch (Iassonov et al., 2009).

There is often a good chance of overstating the pore-solid boundaries by the fact that the pore-solid edges appear with a higher intensity value, when compared to the rest of the pore and solid itself. To reduce this possible error in edges partitioning, the pore and solid gradient threshold were obtained from Sobel filter, an edge detector operator (Sheppard et al., 2004). This function reassigned entire voxels with intensity higher than the gradient value at the phases’ boundaries. The output of the segmentation algorithm for dry sample is phase0 (pore) and phase1 (solid). The clay intensity distribution lies between pore and solid which is part of pore at this step. In order to separate the clays, an additional segmentation algorithm needed to be applied with a similar procedure.

3.3.4.2. Wet Image

Segmentation of partially-saturated or wet tomographic images containing three-phase fluids is more complex and somewhat more arbitrary than the segmentation of dry images. Here, in order to visualise oil spreading films, a high level of doped-oil was used which provides a strong phase contrast. This, however, caused a fuzzy interface, particularly in the positive spreading tomogram due to the diffusion of strong oil signal into the grain and partial volume effect (see section 3.3.1.1). The presence of high level doped-oil below the image resolution causes the intensity histogram of the image to spread out rather than to form distinct peaks and ,hence, phase separation in the image becomes difficult. Considerable precaution and effort was taken to eliminate or to reduce the artifacts (phase contrast fringes) on the images, but not completely avoided. Hence, segmentation of solid regions from wet tomogram might have the risk of overestimation. The segmented solid region from dry image, therefore, was used as the solid region in the wet image through employing the 3D dry-to-wet registration technique. The problems were resolved using the registered, segmented dry image as a mask onto the saturated tomogram in this fashion. In the dry image the contrast amongst pore-solids was sufficient enough to be resolved accurately. In the saturated image the phase contrast fringes could no longer be a problem as the accurate solid map was resolved and used instead of the wet solid map.

In this work, before the segmentation of dry and wet images, a 3D wet-to-dry registration technique (Latham et al., 2008) was applied. The technique involves holding the dry tomogram as a fixed-image and then aligning and resampling the wet tomogram with the fixed-image (see 3.3.2). This generates a pair of images with identical dimensions and enables one to directly compare two sets of data. Thus, the registered dry image is segmented and then the segmented image is used to mask the saturated tomogram to

extract the fluid regions. In the wet images, the solid-pore and solid-liquid regions are precisely segmented and the changes within the pores are determined. The process is further explained through the employment of this method on samples B1 and B2. Note that, core plug B1 was saturated with positive spreading fluids and core plug B2 was saturated with negative spreading fluid system.

Fig. 3-20 shows the optimal workflow used to segment the wet image in this study.

The segmentation procedure basically consists of the following steps:

1. The dry image is registered with wet image and the anisotropic filtering is applied to remove noise and to enhance the quality of the images.
2. The registered dry image is segmented to pore, grain and clay.
3. The segmented dry image is used as a mask for segmenting the wet image.
4. The gas phase in the wet image is segmented. Higher contrast between the gas and other phases makes this a relatively simple segmentation.
5. The registered, segmented dry image and the segmented gas phase are used as masks to segment the wet image into oil and water voxels.

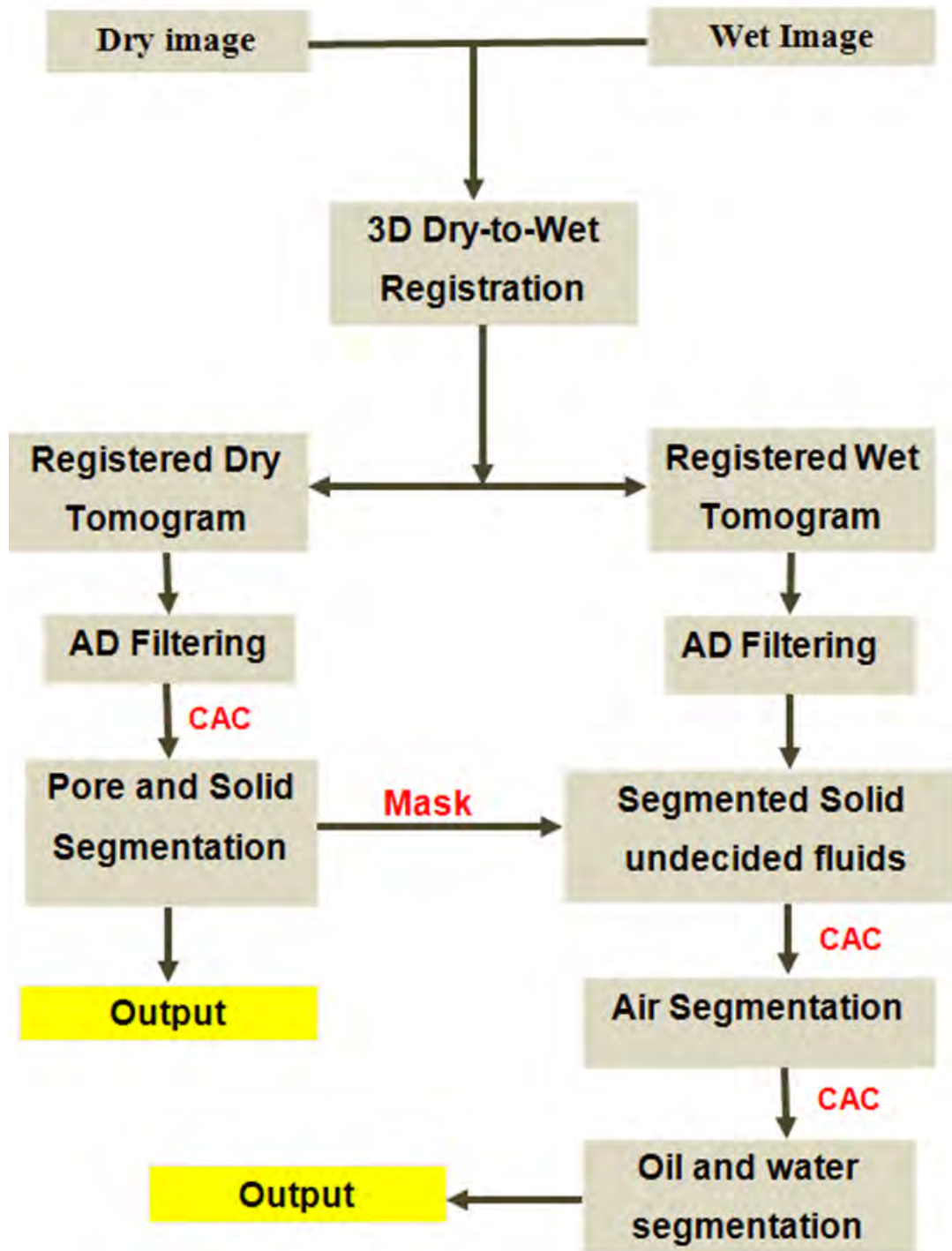


Fig. 3-20, Optimal workflow for segmentation of partially saturated Bentheimer sandstone containing three-phase fluids (water, oil and gas).

3.3.4.3. Segmentation of Sample B1

Followed by the registration of dry and wet images, a subset of $1,452 \times 1,454 \times 840$ voxels³ was taken from each of the registered dry and wet tomograms. **Fig. 3-21** shows a 2D slice from the same location of the dry and wet tomograms. To segment the dry image, values of 4,700 for pores and 5,650 for solids are selected as initial low and high threshold by user. The choice of appropriate thresholds for segmentation is made according to a visual inspection of the grey-scale histogram and the corresponding tomogram by use of *ncviewer*³ software. This software allowed us to observe the features in the wet and dry images while different thresholds are used. The results are further validated by comparison of the segmented tomogram with the grey-scale one. All voxels with values less than the low threshold were labeled as pores and all voxels with values above the high threshold were labeled as solids. The undecided voxels with values between these two thresholds are assigned to pore or grain phases by the CAC algorithm. The segmentation of the pore-solid boundaries was improved by applying the edge gradient threshold chosen using the Sobel filter, an edge detector filter. A grain gradient of 500 was chosen in order to replace the voxels allocated to solid with the voxels allocated to pores.

A visual inspection of dry images shows the presence of some minerals with a range of intensity values between solid and pore. The material is clay and some examples of them can be seen in the red circles shown in **Fig. 3-21(a)**. The voxels in place of clays were separated by the submission of an additional segmentation process (the CAC segmentation) where a low threshold of 5,770 and a high threshold of 5,870 were selected. These thresholds again were chosen according to a visual inspection of the grey-scale histogram and corresponding tomogram. **Fig. 3-22** shows the same section from the

³ A software to visualise X-ray images slice-by-slice

segmented dry tomogram where black, green and khaki represent pore, clay and solid, respectively. Fig. 3-22(b) shows the intensity histograms of the dry tomogram. The peak on the left represents the pore and the peak on the right represents the solid. The information obtained from this histogram was utilised for image segmentation. Gaussian fit of intensity values of pores in yellow, clay in green and solid in red are shown in Fig. 3-22(b). These individual histograms were obtained after the segmentation of the dry tomogram. As seen, there is a good match between the intensity variation of original and segmented tomograms.

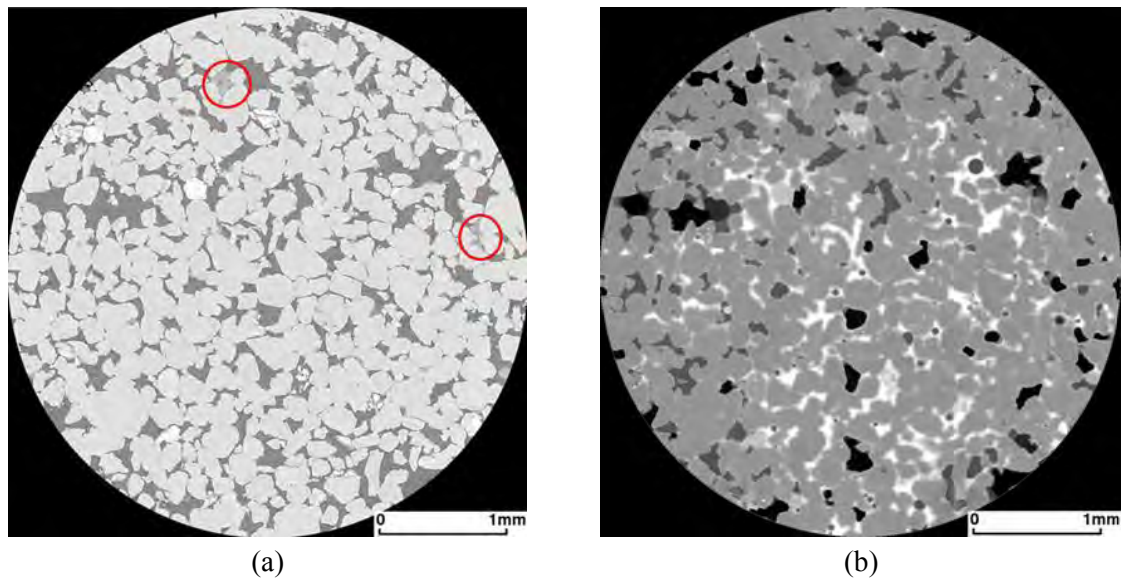


Fig.3-21, (a) a 2D registered slice of dry with resolution of $3.46\mu\text{m}$ and (b) a 2D registered slice of wet with resolution of $3.97\mu\text{m}$ from 3D tomograms. The wet image contains three-phase fluids under positive spreading conditions ($C_s = +5.9\text{mNm}^{-1}$). Grey, dark grey, bright, and black are solid, water, oil and gas, respectively.

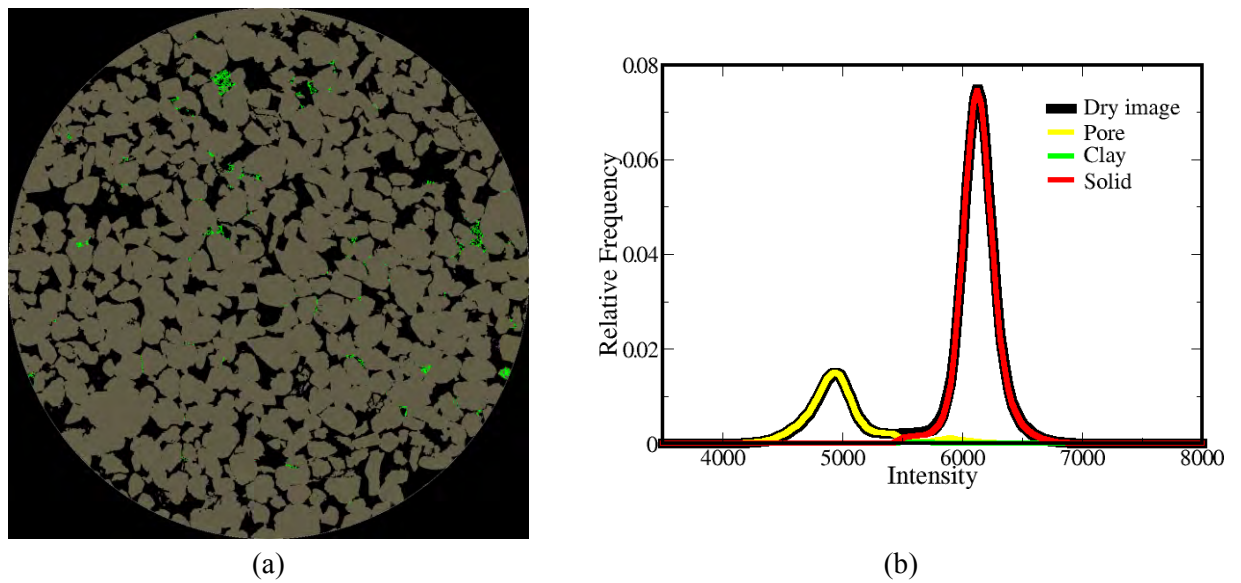


Fig. 3-22, (a) An example of a 2D slice from the segmented dry tomogram (sample B1) where pore is black, solid is khaki and clay is green. (b) An intensity histogram of the dry tomogram shown with a thick solid black line; Intensity distributions of pore (yellow), clay (green) and solid (black) after segmentation of dry tomogram.

Fig. 3-23 shows a comparison between the (MICP) and a numerical simulation on the segmented image using the capillary drainage transform described by Hilpert and Miller (2001). The only significant differences between the experimental measurements and the corresponding image based computations occur for pore sizes below the resolution of the image (~ 3.4 microns). The comparison shows the high quality of the image resolved pore space.

It is worth restating that the oil phase was doped with a large amount of doping chemical (IDD) to ensure its visibility at or below the image resolution. However, this caused fringes at the boundaries of the solid and pores filled by oil. From a visual comparison of the wet and dry images, one can tell that, in the dry image, the phase contrast fringes are either negligible or non-existent and the grain-pore borders are sharp enough to be segmented precisely (see Fig. 3-22). Thus, the problems were resolved using the registered segmented dry image as a mask onto the wet image resulting in eliminating any possible uncertainty due to phase contrast effect artifacts.

Through the application of three subsequent CAC segmentations, the gas, water and oil phases were then partitioned using the original saturated tomogram along with the segmented dry tomogram. A low threshold value of 8,200 and a high threshold value of 8,250 were chosen using the intensity histogram of the wet tomogram and by use of the *ncviewer* software. For the gas phase, the thresholds were easily chosen due to the high contrast amongst gas and the other phases. For the water phase, a threshold range of 8,700 to 8,750 was chosen.

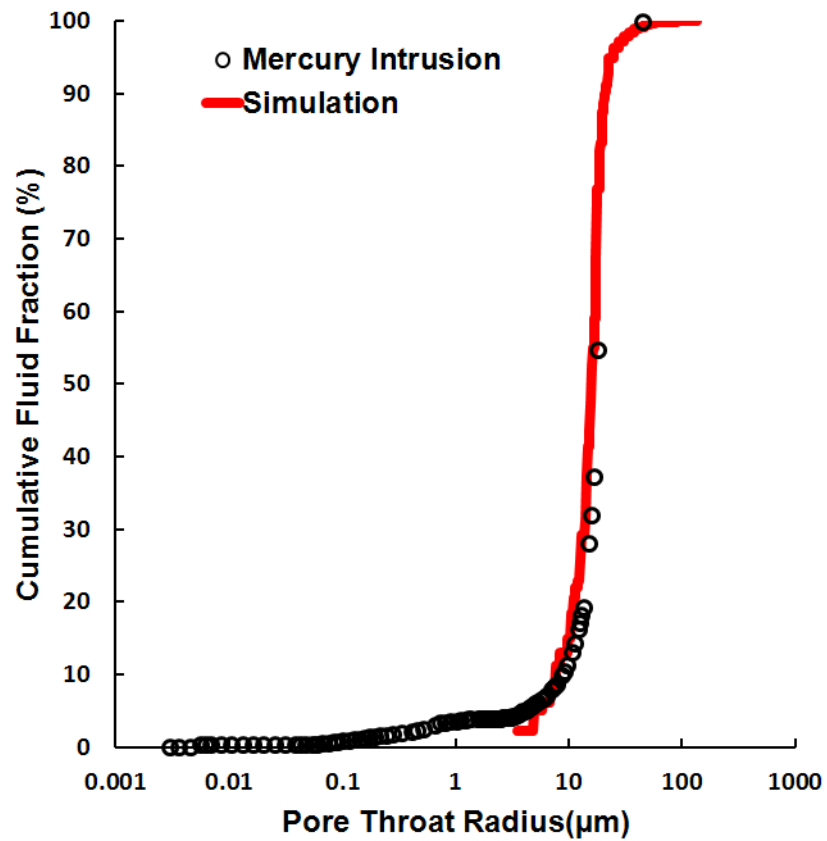


Fig. 3-23, Comparison between measured mercury injection (MICP) and corresponding computations on the dry segmented image. The comparison shows the high quality of the dry image resolved pore space.

Afterwards, a final additional partitioning was carried out using a low threshold of 9,000 and high threshold of 9,050 through which the ‘intermediate phase’ was separated. This phase was finally merged to the oil phase. Since the segmented data was the basis of any further 3D quantitative analyses, the quality of the segmentation was cross-checked visually (slice-by-slice) with caution. All threshold values were chosen based on an extensive comparison of many data values over the process of segmentation. The decisions were also made by the experience level of the user. **Fig. 3-24** demonstrates examples of 2D slices over successive steps of the segmentation process of the saturated tomogram (B1) in the order described above. It is visually evident that the submitted segmentation workflow produced high quality and accurate results.

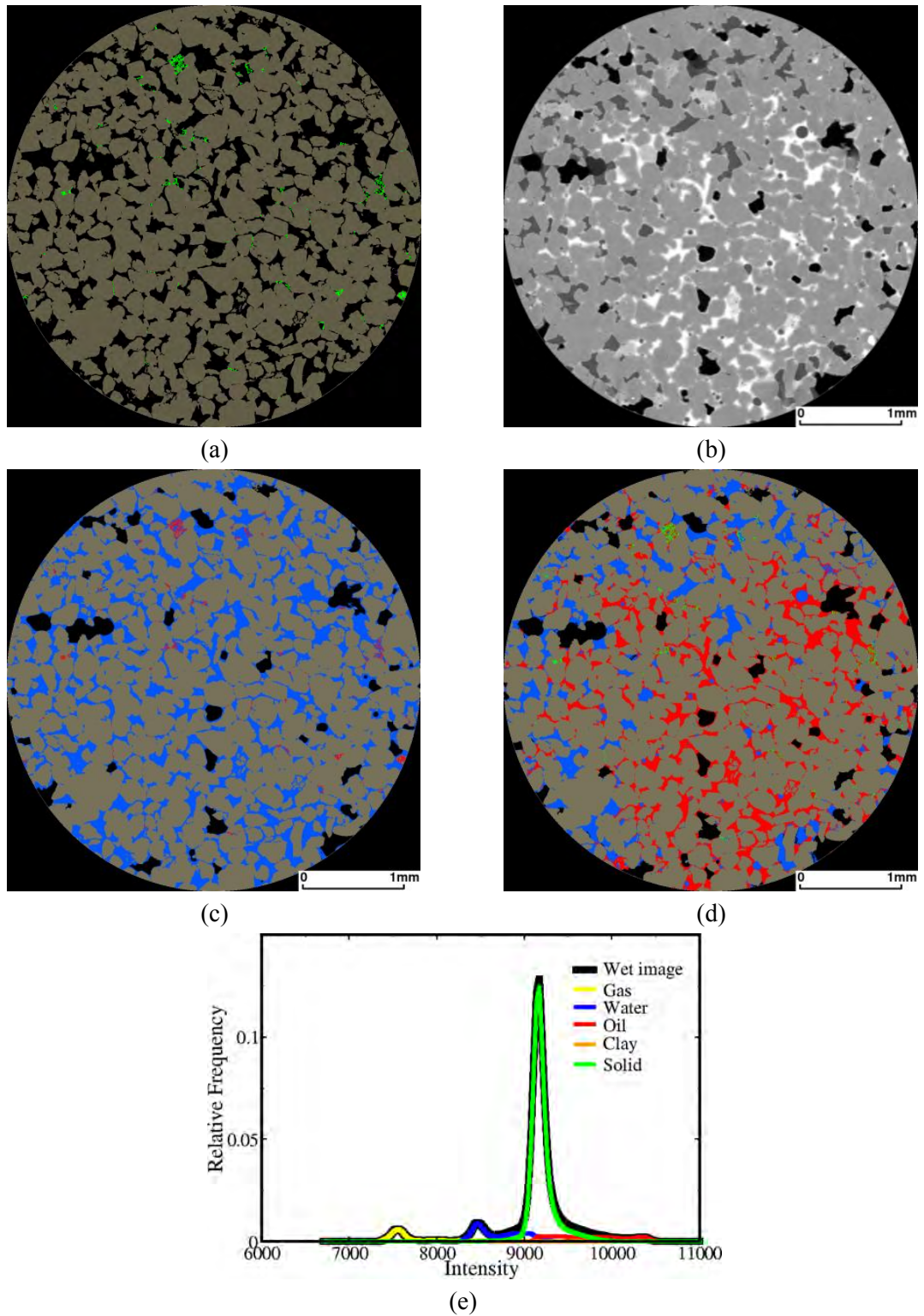


Fig. 3-24, (a) 2D slice of segmented dry image from B1 tomogram where pore is black, clay is green and solid is khaki, (b) 2D slice of wet image where oil, water, gas and solid are bright, dark grey, black and grey, respectively. (c) Solid (khaki) and gas (black) are separated but oil and water are undecided (blue) yet, (d) Final segmented 2D slice showing gas with black, oil with red, water with blue and clay with green. (e) Intensity histogram of original wet tomogram shown with thick black solid and Gaussian fit of intensity values of pore (yellow), water(blue), oil(red), clay(orange) and solid (green) after finalising segmentation of wet tomogram. Spreading coefficient is $C_s = +5.9 \text{mNm}^{-1}$.

3.3.4.4. Segmentation of Sample B2

For the quantitative analysis of sample B2 for the negative spreading system, a similar segmentation workflow described in section 0 was followed to obtain the segmented dry and wet tomograms. A subset of $1,353 \times 1,345 \times 800$ was taken from the registered dry and wet images. The intensity histogram of the dry tomogram is shown in **Fig. 3-25** along with the Gaussian distribution curves for each phase obtained after segmentation. The well match of intensity distribution of the pore and solid with resultant histograms of pore (marked in yellow) and solid (marked in red) shows evidently a good segmentation. The accuracy obtained from acquiring the dry image at the highest possible resolution ($\sim 3.9\mu\text{m}$) allowed the pore-solid regions to be segmented clearly. The dry image after the segmentation of pore, clay and solid is shown in **Fig. 3-26(a)** where pores are shown in black, solid in khaki and clay in green.

The experimental MICP on the sister plug and capillary drainage simulation on the segmented data were compared to ensure the segmentation quality of the 3D dry image. **Fig. 3-26(b)** shows a good match between two approaches. The only significant difference between the experimental MICP and numerical CDT occurs for throat sizes approaching, at, or below the resolution limit (voxel-size) of the image.

Fig. 3-27 shows 2D registered sections through the dry and wet tomograms of sample B2. The segmented dry image was taken away from the porous system of the wet image using the registration technique. This is an accurate approach for two reasons; extreme care was taken to prevent any movement of the sample during the imaging of the wet and dry images, the registration and resampling techniques adjusted the alignments of both dry and wet image to a similar one. After masking the solid phase out of the wet image using the segmented dry image, an additional CAC process was applied with a low

threshold of 5,800 and a high threshold of 5,850. These threshold endpoints provided the oil phase data set and the alignment of the segmented dry image with the wet image prevented any overestimation from occurring. In Fig. **3-27(c)**, a section of the segmented tomogram is shown where the solid and oil phases are represented by khaki and red, respectively. The water and gas phases are yet to be classified and are denoted by black. To finalise wet image partitioning, one more step was carried out to segment the gas phase using the threshold range of 5,070 to 5,200. This was enhanced by adding a gradient threshold of 200 to label voxels at the interface of water and gas to the gas phase.

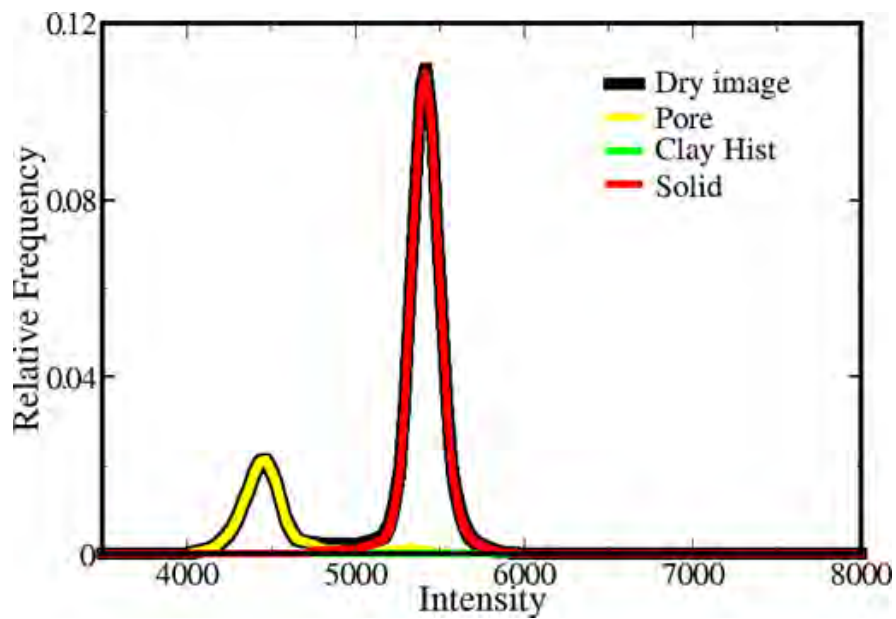


Fig. 3-25, Intensity histogram of dry tomogram (sample B2) displaying with thick solid black line; Gaussian Intensity fits of pore (yellow), clay (green) and solid (red line) after segmentation of dry tomogram.

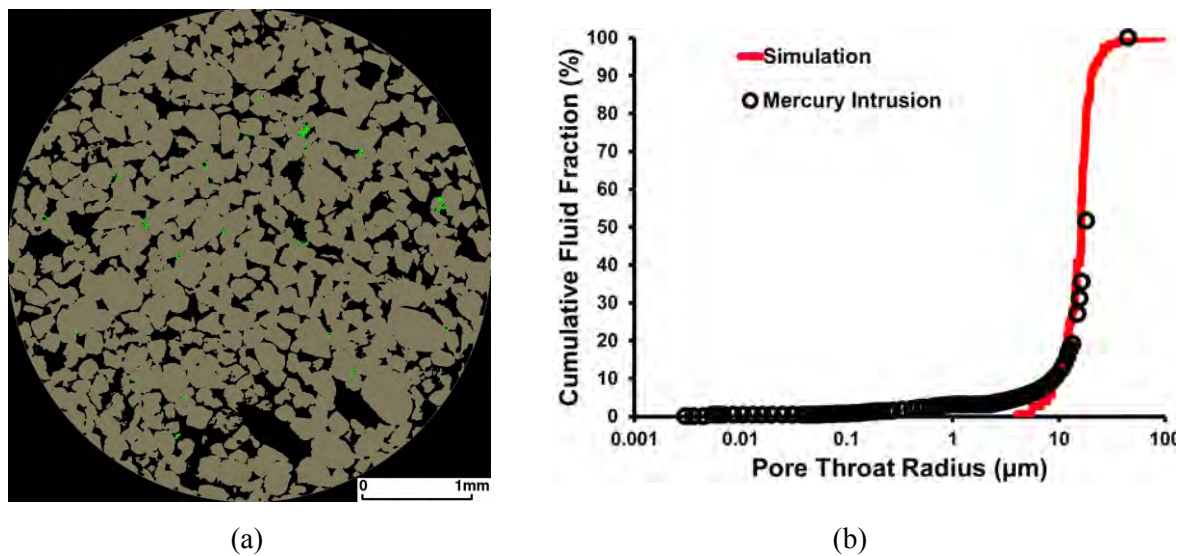


Fig. 3-26, (a) 2D slice of segmented dry tomogram where the pore, solid and clay are denoted by black, khaki and green, respectively. (b) Comparison between measured mercury injection (MICP) and corresponding computations on the dry segmented image.

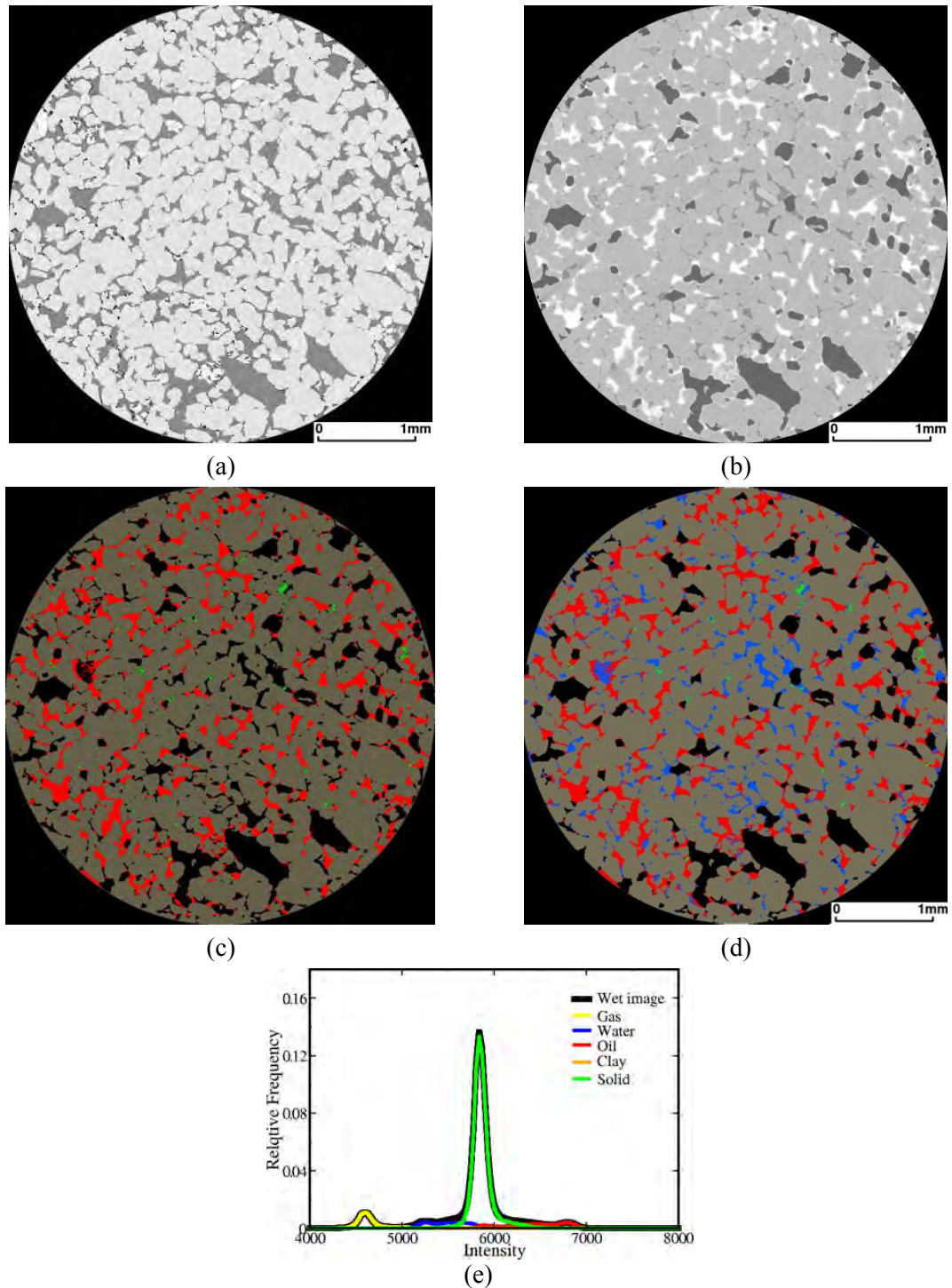


Fig. 3-27, (a) 2D slice of segmented dry image from B2 tomogram where pore is black, clay is green and solid is khaki, (b) 2D slice of wet image where oil, water, gas and solid are bright, dark grey, black and grey, respectively. (c) Solid (khaki) and oil (red) are separated but gas and water are undecided (black) yet, (b) final segmented 2D slice showing gas with black, oil with red, water with blue and clay with green. (e) Intensity histogram of original wet tomogram shown with thick black solid and Gaussian fit of intensity values of pore (yellow), water(blue), oil(red) ,clay(orange) and solid (green) after finalising segmentation of wet tomogram. Spreading coefficient is $C_s = -8.7 \text{ mNm}^{-1}$.

3.3.5. Porosity, Fluid Saturation and Distribution

Once segmentation was completed, estimations of porosity, fluid saturations and their distributions were made from the segmented images. Porosity and saturation are estimated by counting the number of voxels assigned to each phase during segmentation regardless of the number of phases present in the images. Porosity is computed by counting the number of voxels assigned to the pore space across the segmented dry image to the total voxel count of the grain and pore. Saturation is estimated by dividing the voxel count of the individual fluid across the segmented wet image to the summation of voxel count of all fluids. The computed saturation reveals the distribution of the individual fluid across the wet image.

3.4. Spatial Characterisation of Distribution and Connectivity

3.4.1. Generation of Pore-scale Network of Three-phase Fluids

The pore-scale network model of each phase can give quantitative and visual descriptions of spatial occupancy of each phase. This technique can also be used to see how water, oil and gas are distributed in the pore space for positive and negative spreading systems.

The 3D pore-scale network model of each fluid was derived using the segmented image as input data. In order to generate individual network of oil, water and gas from the segmented image, at first place, the Euclidean Distance Transform (EDT) of individual fluid was obtained (Saito and Toriwaki, 1994). The Euclidean distance is the distance of each voxel of a phase from the nearest phase-solid boundary. As the Euclidean distance of a voxel increases, a higher intensity value is assigned to this voxel. Hence, the voxels with

highest intensities indicate the centres of pore space (individual fluid space). The EDT map was used to calculate the maximum covering sphere radius at each point which is the radius of the largest sphere which lies completely within the pore space and covers that point (Silin and Patzek, 2006). Pore centres were also used to skeletonise the network of each phase by applying the Medial Axis (MA) method (Lindquist et al., 1996, Pudney, 1998). A labelling algorithm followed by a region-merging algorithm is then applied to complete pore partitioning (Jones et al., 2009). This pore partitioning scheme allows one to construct pore network models from tomographic images. **Fig. 3-28** shows an illustration of the generation of the medial axis and the resultant pore partitioning on a small 2D and 3D subset presented by Jones et al. (2009). Note that the providing details of algorithms of each step are beyond the scope of this study and details can be found in references (Sheppard et al., 2005, Jones et al., 2009).

Pore partitioning allows us to define a number of statistical parameters that characterize the spatial pore occupancy of the individual fluid (oil, water and gas). The important descriptors include pore radius distribution and pore volume equivalent radius distribution. These parameters show the 3D distribution of the individual fluid throughout the pore space based on its size. Note that, the preferential occupancies of the air, water and oil are determined according to the pore space wettability condition. As Bentheimer sandstone is known to be strongly water-wet, the smallest pores are to be occupied by the wetting phase being the water phase and the largest pores are to be filled by the non-wetting phase being air. The moderate pores are expected to be occupied by the intermediate phase which is the oil phase. The statistical parameters obtained from generated pore network of individual fluids provided the 3D fluid occupancy information.

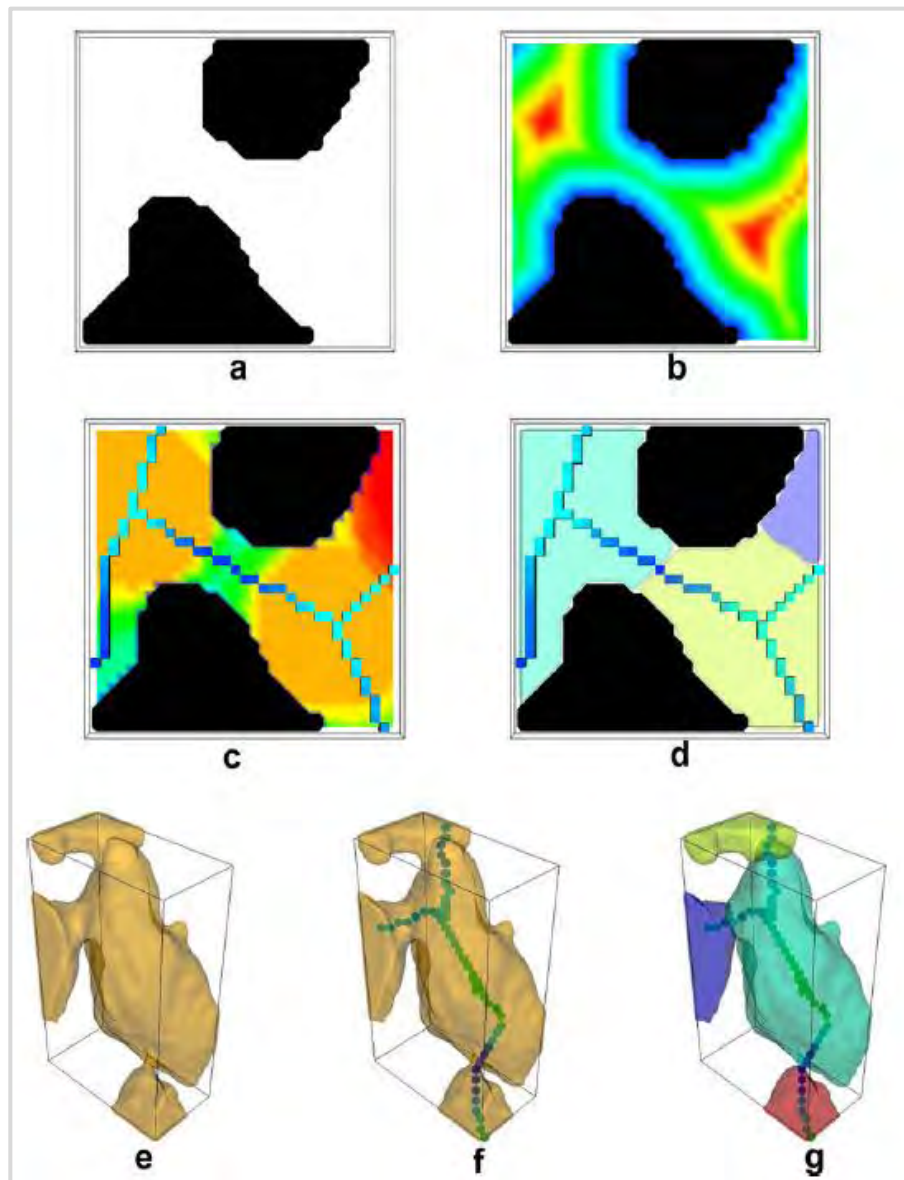


Fig. 3-28, Illustration of pore interconnections and partitioning algorithm (a) segmented pore-throat, pore-white and solid-black (b) calculated Euclidean Distance Map (c) Calculated covering sphere radius, the centre is calculated from maximum covering radius (d) The medial axis junction (e-g) Illustration of generation of the medial axis on a small 3D subset of a porous image by Jones et al. (2009).

3.4.2. Spatial Connectivity Using the Euler Characteristic Method

Quantitative morphological description of the connectivity of the complex fluids in an actual porous medium is difficult. This is mainly because of the inherent complexity of 3D description for any topological structure and anisotropic shapes of the fluids distributed in intricate 3D pore structures. To overcome these difficulties, the Euler characteristic is used as an appropriate measure. Euler characteristic (Mecke and Wagner, 1991) of an object is topological invariant, meaning that it remains unchanged under any continuous deformation of the object. Topological structure is significant due to its close relation to physical properties (Wildenschild and Sheppard, 2013). The Euler number (χ) of a collection of objects is a fundamental mathematical description of the links that occur between the objects (Roberts et al., 1997).

Topological properties, in a three-dimensional porous medium, are based on three factors; the number of isolated elements or isolated convex (N), i.e. oil blobs, the number of enclosed elements or closed concave (C), i.e. trapped oil drop by other fluids and the number of redundant connection (H) between the oil blobs. Based on these parameters, the specific Euler number is defined as follows (Vogel, 2002):

$$\chi = \frac{N - C + H}{V} \quad \text{Eq. 3.8}$$

where V is the volume of the interest. In this study, as the wet image is segmented to numbers of voxels, the Euler number is defined by (Arns et al., 2001):

$$\chi = \# \text{ Vertics} - \# \text{ edges} + \text{faces} - \text{volumes} \quad \text{Eq. 3.9}$$

where \neq means ‘number of’. The Euler characteristic gives a positive value for poorly connected structure where the numbers of isolated convex are greater than the number of redundant connection. In contrast, the Euler number gives a negative value for highly connected phases where numbers of connected objects are greater than isolated ones. The Euler characteristic has previously been used to quantify the continuity of porosity in porous media (Vogel and Roth, 2001, Vogel, 2002), the connectivity of thin films (Jacobs et al., 2000) and the distribution of fluids in porous media (Mecke and Arns, 2005), amongst numerous other applications related to the connectivity of objects. An important advantage of this approach is that it provides an unbiased estimation of connectivity from local measurements on a digitised image for a 3D cut-out of arbitrary shape and volume.

In this study, in order to compare the connectivity and continuity of the three-phase fluids at positive and negative spreading conditions, the Euler characteristic of each of the phases (oil, water and gas) in the digitised segmented image was computed and compared. The Euler characteristics computational aspects and procedure are described elsewhere (Arns et al., 2001). The method algorithm has been implemented in-house built software (Morphi). The further details of the method and examples can be found in (Arns et al., 2001, Arns et al., 2002, Arns et al., 2004, Arns et al., 2010).

3.5. Three-dimensional Visualisation

Once wet images for both positive and negative spreading systems were segmented, they were visualised for a qualitative analysis using the built volume rendering software, Drishti software (Vislab, ANU), developed at ANU. In Drishti software, a transfer function is determined by choosing coordinates on intensity-gradient diagram to a particular colour and transparency. Drishti software can create 3D images from raw tomographic images

and segmented images. In this study, only segmented images were used as input in Drishti for 3D visualisation. Three-phase fluids spatial distributions at spreading and non-spreading systems were generated and compared for qualitative analysis.

Chapter 4

Results and Discussion

This chapter presents results of three-phase flooding experiments and X-ray micro-CT imaging. Most significant findings obtained from the study are (1) the relationship between the spreading characteristic of a three-phase system and the fluid distribution and configuration within a homogeneous sandstone and (2) the evidence for spatial connectivity and continuity of the oil films after tertiary gas flooding.

Fig. 4-1(a) shows a grey scale 2D slice from the dry tomogram of core plug B1. The corresponding registered 2D image for the wet positive spreading system at the completion of the gas flooding is shown in **Fig. 4-1(b)**. The images demonstrate the preferential fluid distribution in the strongly water-wet Bentheimer. The solid regions on the dry and saturated images are grey while the pore and air are black. It can be seen in the wet images that the water (dark grey) is distributed in the small pores and throats. The gas (black) occupies the larger pores and the doped-oil (bright) occupies the intermediate pores and throats.

Fig. 4-1(a)–(b) illustrates that large pores have a higher likelihood to be occupied by gas than oil and water. There are also large pores that are not occupied by gas despite having a magnitude where gas tends to invade. The reason for this apparent contradiction is that a large pore radius is not a sufficient condition for a non-wetting phase to reside. There must be a full neighbourhood to form a non-wetting phase cluster. A visual inspection of dry and wet images shows that the artifacts including strong fringes and beam-hardening have been mostly avoided due to the precautions taken before imaging

(see section 3.3.1.1). As can be seen in Fig. 4-1(b), air bulk interfaces with oil-filled neighbouring pores are bright except two air bulks at the top of the image which are trapped by water phase. In Fig. 4-1(c)–(d), magnified sections from wet image, blurring interfaces with thin bright bands can also be visible. These blurring interfaces represent oil spreading films with thicknesses at or below the resolution (voxel-size) of the images, hence they are rather weak. Strong absorption phase contrast at the doped-oil interfaces results in ‘bleeding’ or spreading of the oil signal at the interfaces and this effect is the key for imaging oil features at the length scales below the image resolution of the imaging system. While it is not possible to estimate the thickness of the films, the signal for some of the thicker films, because of excessively-doped level of oil, appears to be sufficient for their presence to be distinguished.

In this thesis, the attempt was made to image thin wetting and spreading films by doping the water and oil phases to increase their attenuation of X-rays. The difference in attenuations makes it possible to image the network of oil spreading films for the positive spreading system. However, the thickness of the films cannot be resolved. This is not a limitation in this thesis whose objective is to confirm the presence and continuity of the films. The 2D slices of Bentheimer sandstone with localised oil and gas in the presence of water with negative spreading characteristics are shown in **Fig. 4-2** where the oil, water and air are seen in bright, dark grey and black, respectively. The overall distribution of the phases for the negative spreading system in core plug B2 is similar to the distribution observed with corresponding positive spreading system. Water as the wetting phase occupies the smaller pores and throats while oil fills the larger pores as the non-wetting phase. When gas is present, it occupies the largest pores as the most non-wetting phase.

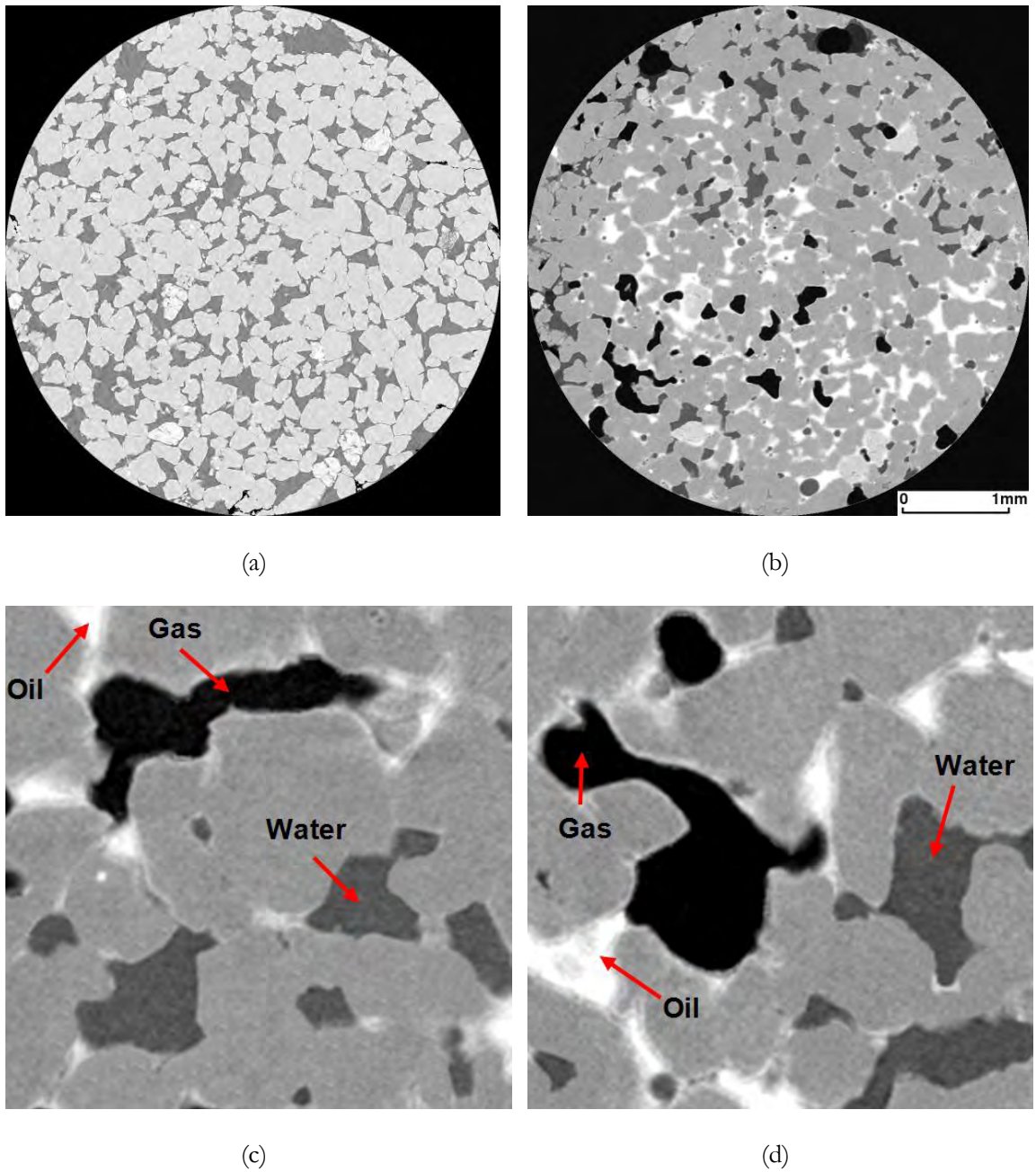


Fig. 4-1, Registered 2D slices from (a) dry tomogram of B1 where pore and solid are black and grey and (b) wet tomogram of B1 containing positive spreading fluids system($C_s = +5.9 \text{mNm}^{-1}$), (c) – (d) Magnified sections from wet tomogram where air, oil, water and solid are black, bright, dark grey and grey.

As shown in Fig. 4-2(b)-(c), the air interfaces are sharp and well defined with no indication of oil spreading films. In contrast, as shown in Fig. 4-1(c)-(d), the air interfaces in the positive spreading system are fuzzy and diffused by the signal from oil films lying between the air and grains even though the thickness of these films is below the resolution of the images. This is a clear indication of the presence of oil spreading films for the positive spreading system (Feali et al., 2012). Since the core plug is strongly water-wet, water films are expected to be seen between the oil and the grains, however, these films are too thin and their attenuations are too low for them to be resolved from the noise and phase contrast effects at the solid boundary. Kumar et al. (2009a), using the same imaging system, arrived at a similar conclusion for imaging two-phase gas-water systems in a strongly water-wet sandstone. A comparison between the wet tomograms for the negative (Fig. 4-2(c)-(d)) and positive spreading systems (Fig. 4-1(c)-(d)) shows that the bulk oil, water and gas phases can be clearly resolved at the pore-scale for both spreading systems.

In the negative spreading system, individual oil films that can be observed around the gas phase (as shown by red circles in Fig. 4-2(b)) do not necessarily suggest the connectivity of the oil bulk through oil films. The stability of the oil films depends on the geometry of the pore space, the thickness of the oil films and the spreading characteristics. The oil film here may remain stable based on its thickness. It should collapse as the thickness falls below a critical thickness (Dong et al., 1995, Keller et al., 1997). Several individual oil lenses (shown by red arrows) can be also observed in Fig. 4-2(b), which are captured between the water and gas phases in the corners of the pores. These oil lenses should be trapped because of the capillary effects and the geometry of the corners (Blunt et al., 1995, Keller et al., 1997, Fenwick and Blunt, 1998).

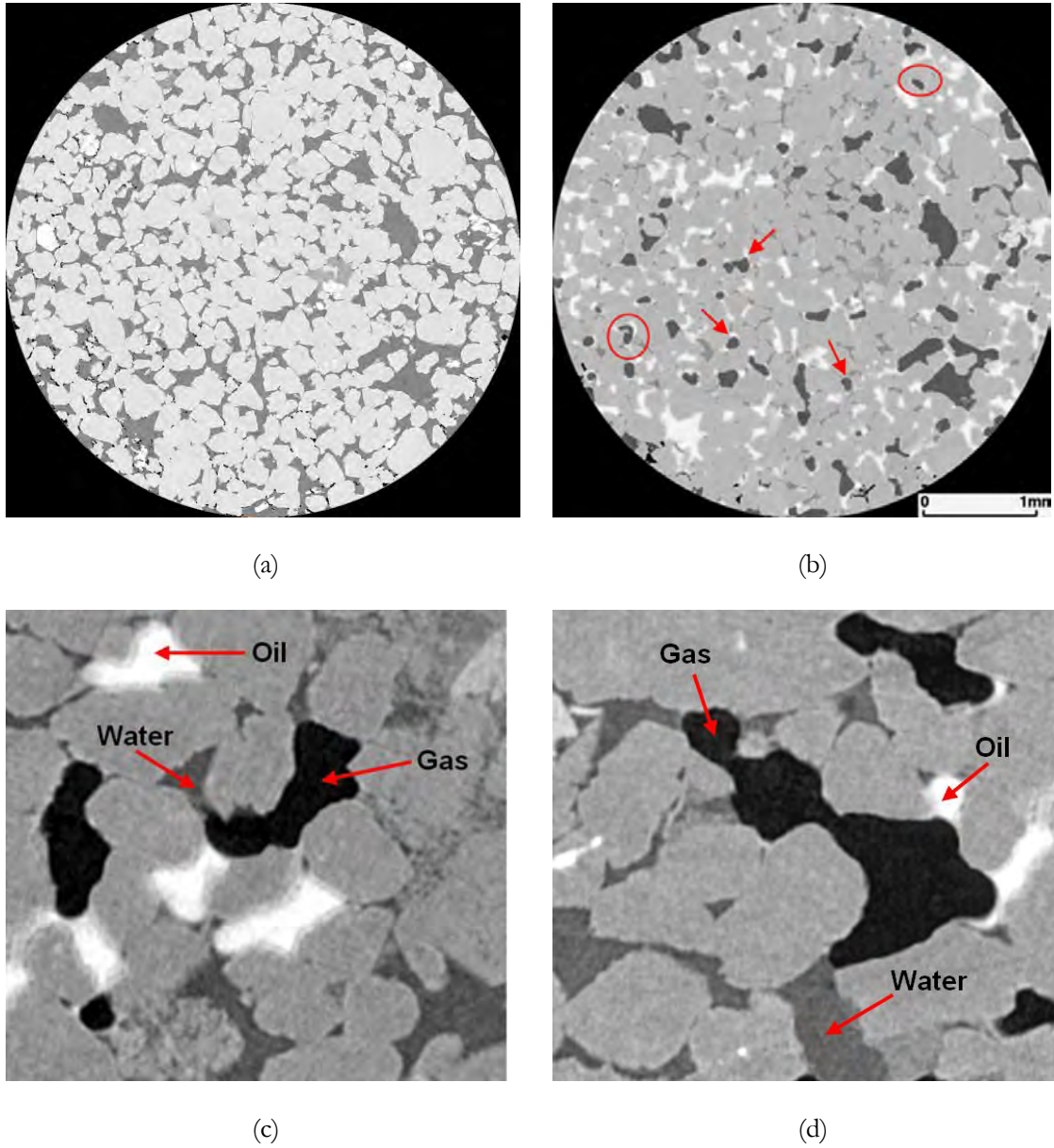


Fig. 4-2, Registered 2D slices from (a) dry tomogram of B2 where pore and solid are black and grey, (b) wet tomogram of B2 containing negative spreading fluids system($C_s = -8.7 \text{ mNm}^{-1}$), (c) - (d) Magnified sections from wet tomograms where air, oil, water and solid are black, bright, dark grey and grey.

Further indirect evidence of the presence of oil films for the positive spreading system can be seen in **Fig. 4-3** where a thin section from the tomogram for the positive spreading system is shown. The section shows what appears to be an ‘intermediate phase’ between the air and the oil phases. This phase is frequently observed in the tomograms of positive spreading system but is never observed in the tomograms of negative spreading system. Based on the attenuation levels, this ‘intermediate phase’ appears to be the result of gas continuing to displace oil during the scanning period of approximately 18hrs. Given the times involved and the relatively low oil saturation it is likely that the redistribution of the oil involves flow through oil spreading films which is expected to be a slow process. For the negative spreading system, there are no oil spreading films and a redistribution of oil and gas occurs relatively fast by flow through fluid filled pores and throats (Feali et al., 2012).

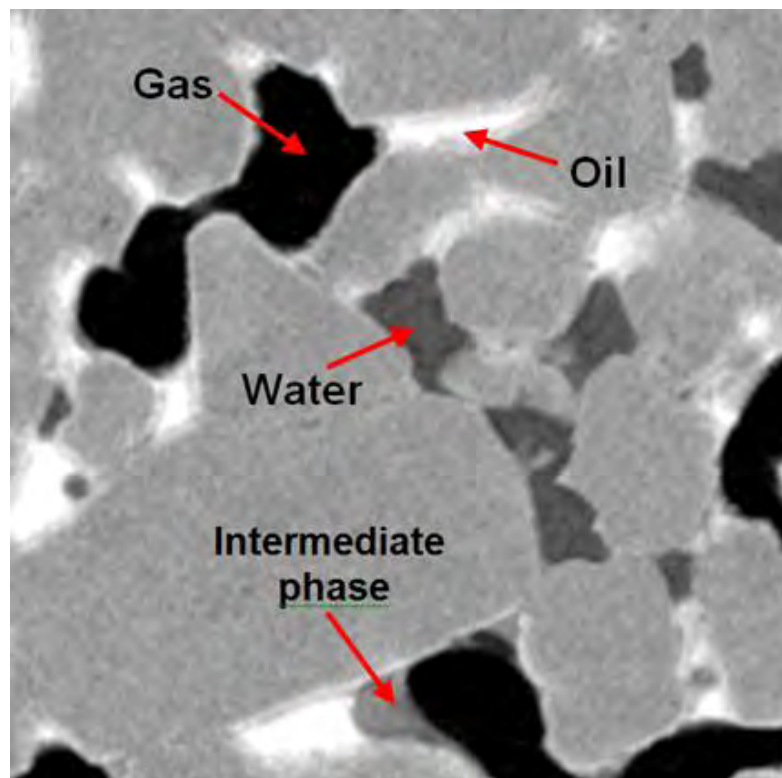


Fig. 4-3, Section from the positive spreading system tomograph showing gas-oil redistribution during the scanning period.

4.1. Analysis of Films for Positive and Negative Systems

In this section the results of analyses of oil and water films and their connectivity at both positive and negative spreading conditions are presented. Subtraction method (see section 3.3.3) was used to extract information of water and oil distributions and their connectivity through films irrespective to the possible images artifacts including phase contrast fringes. This artifact can be interpreted wrongly as the oil films (detailed in section 3.3.1.1). The advantage of this technique is to eliminate the grain and air phases including the grain artifact (phase contrast fringes) from the images leaving with the water and oil phases. This made analysis of the oil and water films possible and simpler with no uncertainty. The segmented images for both fluids systems are also presented.

4.1.1. Spreading System

Fig. 4-4(a) shows a 200×200 slice of a 3D image of core plug B1 in the dry state. **Fig. 4-4(b)** shows the same slice of the core after a three-phase flooding (positive spreading condition) was undertaken into the dry sample under strongly water-wet conditions. The water, oil, solid and air appear as dark grey, bright, grey and black, respectively. A visual inspection of these slices shows bright blurring bands surrounding the gas bulk phase on the air-rock interfaces or even on the water-rock interfaces. These bands are reasonably faint and are likely to be the oil spreading films with a thickness at or below image resolution. The question is whether those bands merely appear to be image artifacts or whether these are in fact oil films spreading on the gas interface.

To avoid any sample movement during the X-ray imaging, extreme care was taken and it can be safely assumed that the solid phase in the dry image is aligned on the solid phase of the wet image. This helps to eliminate the voxels belonging to the solid phase in

the wet image and to extract the voxels in place of the water and oil phases. Fig. 4-4(c) is obtained by the subtraction of the dry image from the wet image. The bright and grey colours indicate the oil and water phases, respectively, while the similar voxels in both dry and wet images turn black. As seen in the subtracted image (see section 3.3.3), the bulk oil adjacent to the gas phase is connected through thin layers which appear to be oil films spreading on the gas and grain interfaces.

Fig. 4-4(d) shows the segmented wet image slice for the positive spreading system where oil, water, gas and solid are denoted by red, blue, black and khaki, respectively. The segmentation approach involves the masking of segmented dry image onto the wet images. It is safe to assume that the pore-grain boundaries are well segmented as the dry image has a very good quality and sharp pore-solid interfaces. The presence of oil films between the gas and oil phases are clearly visible. It may be that the thickness of the films is to some extent overstated both as a result of the inability to visualise water wetting films (which have a length scale well below the resolution of the image) and the contrast introduced at oil interfaces by the high level of doping required to make the oil films visible. The segmentation process is detailed in section 3.3.4.

In order to further confirm the previous qualitative description, another example of a 200×200 slice of dry and wet images through a 3D tomogram was selected and is shown in Fig. 4-5. The existence of contrast bands around the gas interface can be visually verified. Oil bulks are located around the neighbouring gas bulks which appear to be connected through the layers (Fig. 4-5(c)). The thickness of the layers seems to vary depending on the geometry of the corners or the crevices. As the width of the phase contrast fringes is not associated with the geometry of the pores, the layers are in all likelihood spreading oil films. As described before, grey bulks between air and oil bulks can also be seen in Fig. 4-5(b) which is called “intermediate phase” with an attenuation

somewhere between oil and air. This is an oil blob that retreated part way back through acquisition time. This occurred because of redistribution of the oil involves flow through oil spreading films which is expected to be a slow process.

The wet image segmentation is shown in Fig. 4-5(d) where oil, water, gas and solid are denoted by red, blue, black and khaki, respectively. From the segmented image it is noted that the oil film thickness is to some degree overestimated by the same reason mentioned before. A wide range of oil film thicknesses are observed in the total data set. The largest films were estimated to be a couple of microns thick while the smallest films are almost invisible and their thickness is impossible to estimate.

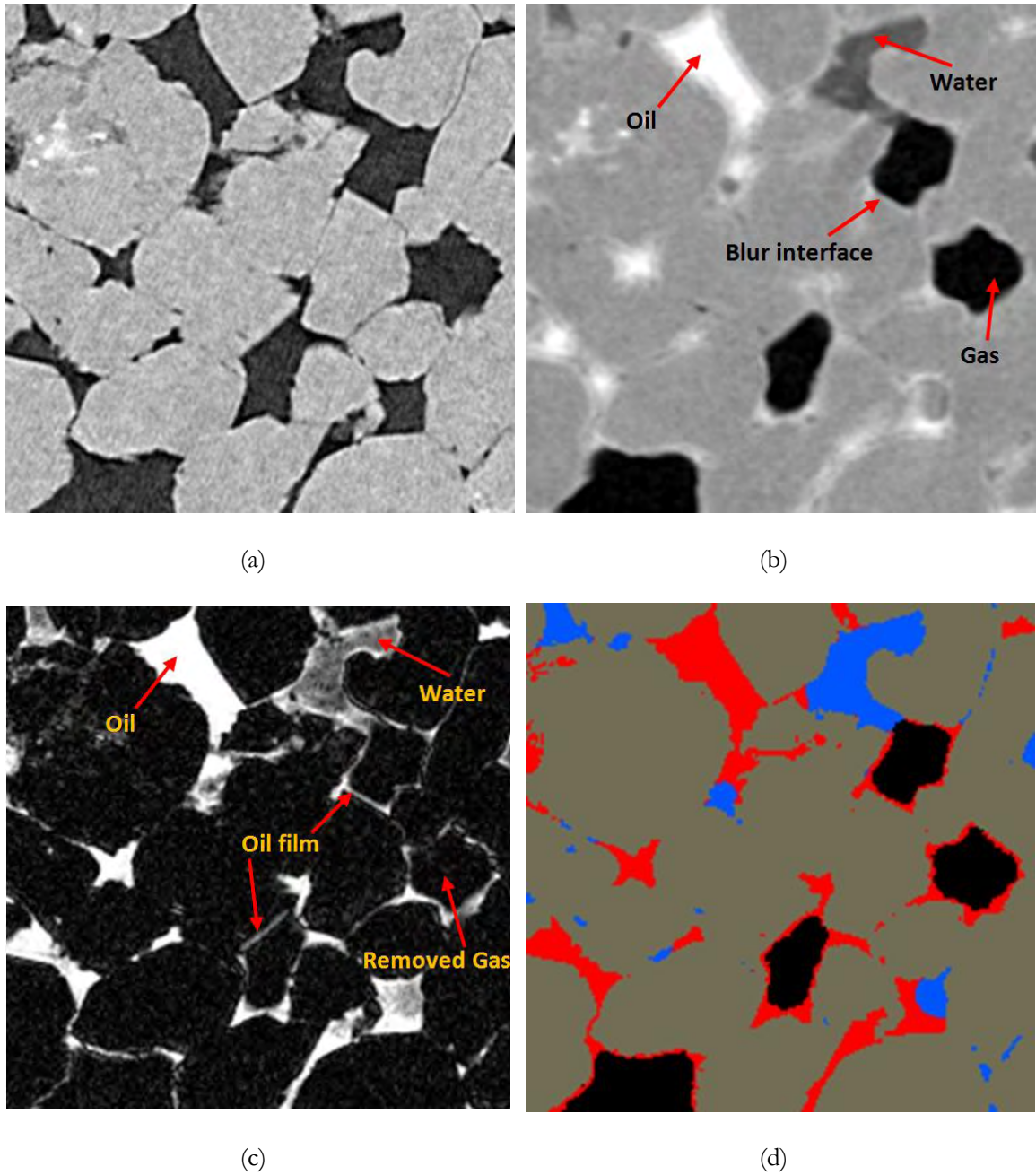


Fig. 4-4, Sections from positive spreading tomograms of core plug B1, $200 \times 200 \times 200$ voxels³ (a) dry, (b) wet. Solid, air, water and oil are grey, black, dark grey and bright, respectively. (c) Section representing subtraction of dry and wet images where oil shown in bright, water in grey and solid-air in black, (d) Segmented subset shows water in blue, air in black, oil in red and solid in khaki.

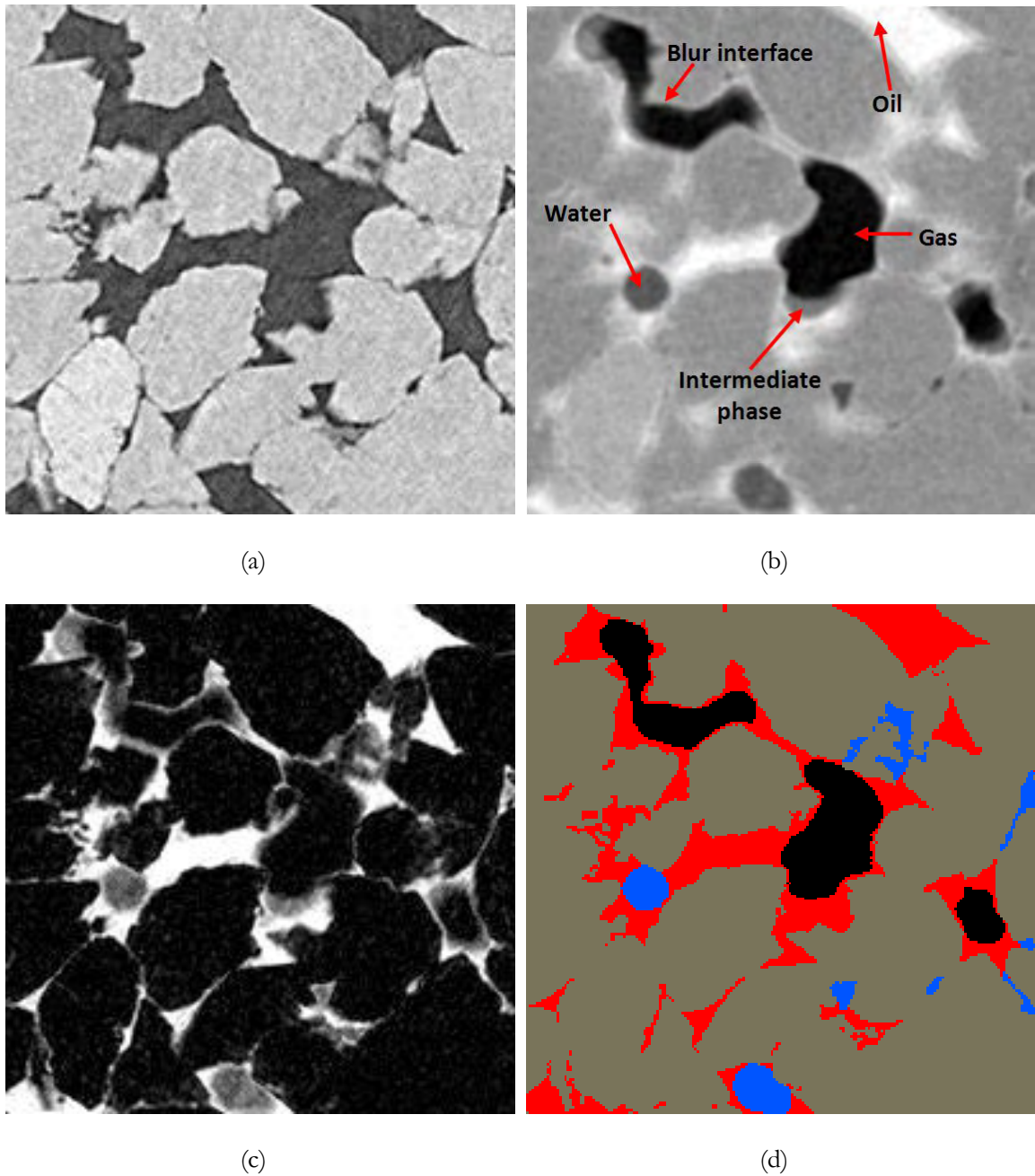


Fig. 4-5, Sections from positive spreading tomograms of core plug B1, $200 \times 200 \times 200$ voxels³ (a) dry, (b) wet. Solid, air, water and oil are grey, black, dark grey and bright, respectively. (c) Section representing subtraction of dry and wet images where oil shown in bright, water in grey and solid-air in black, (d) Segmented subset shows water in blue, air in black, oil in red and solid in khaki.

4.1.2. Non-Spreading System

Fig.4-6(a) shows a 200×200 slice through a 3D image of core plug B2 in the dry state. Fig.4-6(b) shows the same registered slice of the core after the three-phase flooding experiment was carried out using negative-spreading fluids. From a visual inspection of the wet image, the absence of the pronounced contrast bands (blurry interfaces) at the gas-rock interfaces is evident. However, one may question that the very faded and blur interface on the edges of upper right pore may have been caused by oil films. To answer this question, the difference map of the dry and wet images was obtained using the procedure described in section 3.3.2. Fig.4-6(c) exhibits the subtraction image in which the oil and water phases have the highest and lowest intensity values, while the other phases have an intensity value of zero. The oil phase is bright and the water phase is grey. In contrast to the difference map of core plug B1, the bulk oils here are not connected together through any layers. This suggests that the oil blobs are captured between water and gas and they are not connected through the oil films. In addition, the very blur interfaces are to be contrast fringes that have easily been eliminated using renormalisation and subtraction method. As seen in difference image Fig.4-6(c), the water films cannot be seen. Because the core plug was strongly water-wet, water films are expected to be seen at gas-rock or oil-rock interfaces. Nonetheless, these films are so thin and their attenuations are not comparable with oil and rock attenuation which makes it impossible to be resolved. Fig.4-6(d) shows the segmented result of the wet image. The segmentation procedure is described in section 3.3.4. The segmentation process involves masking the dry segmented image onto the wet sample. High quality of the dry image and sharp pores-solid interfaces ensure that the pore-grain boundaries were partitioned with a high level of precision.

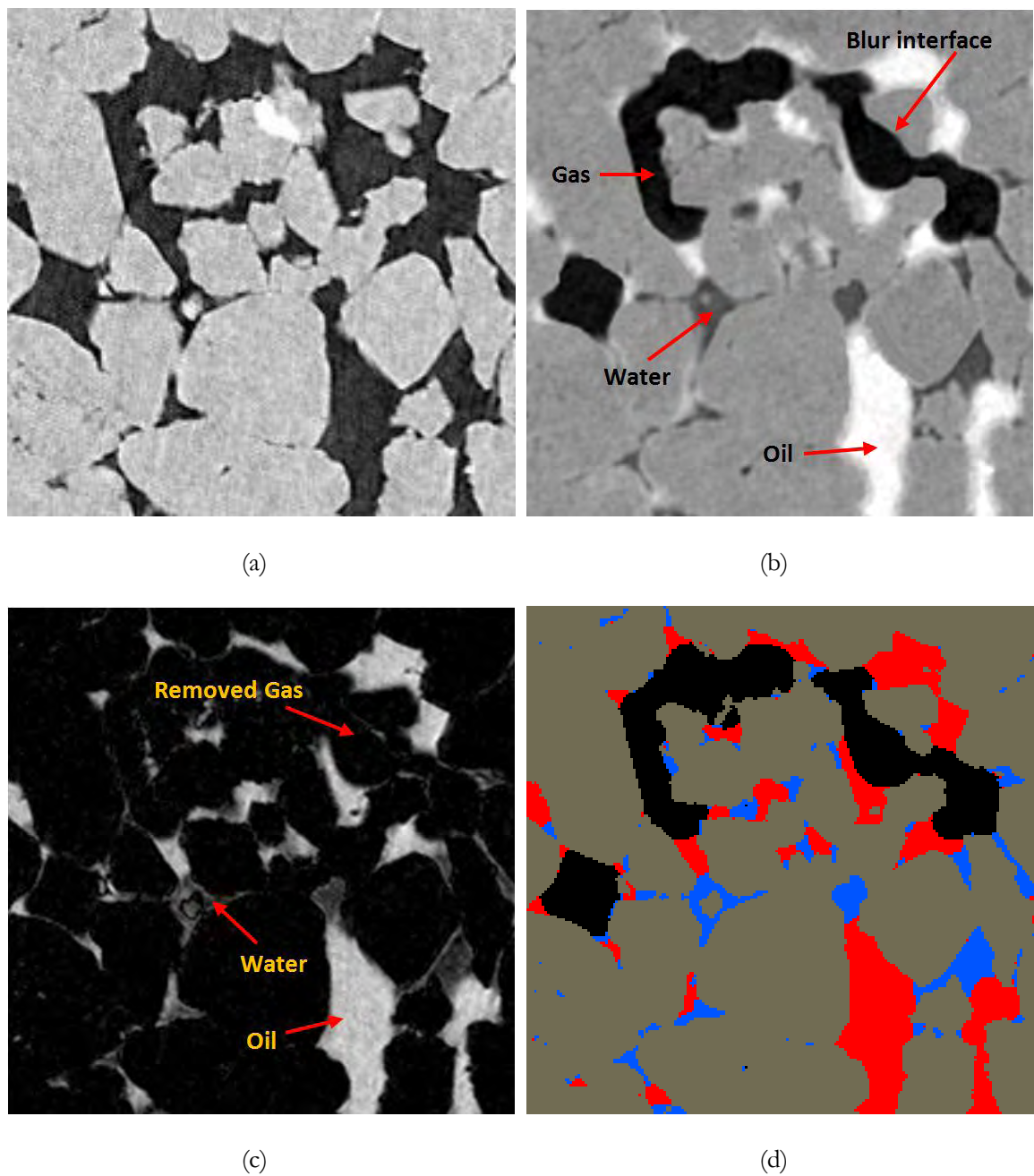


Fig.4-6, Sections from negative spreading tomograms of core plug B2, $200 \times 200 \times 200$ voxels³ (a) dry, (b) wet. Solid, air, water and oil are grey, black, dark grey and bright, respectively. (c) Section representing subtraction of dry and wet images where oil shown in bright, water in grey and solid-air in black, (d) Segmented subset shows water in blue, air in black, oil in red and solid in khaki.

This suggests that, after using the dry image as a mask for the segmentation of the wet image, the regions in the pore space that underwent a change are relabelled as water and oil. Conversely, the regions in the pore space that do not undergo a change are relabelled as air and the remaining regions are relabelled as solid. It is apparent from the image that the oil phase (red) is trapped between gas (black) and water (blue) phases and there is no visual evidence of films. Again, the very faded phase contrast fringes were no more problems for segmentation and in turn image quantification as the segmented solid phase of the dry image was used as the solid phase of wet image.

A more qualitative analysis of oil connectivity was performed on another 200×200 slice through a 3D tomogram of dry and wet cores. **Fig. 4-7(a)** shows a subset of the density map of the dry image and **Fig. 4-7(b)** shows the corresponding registered density map of the wet image. A comparison with **Fig. 4-4** and **Fig. 4-5** suggests that there is no indication of the presence of continuous oil spreading films. However, a question arises when looking at the faded and blur interface of the largest pore in the wet image. The subtraction method had to be repeated again to clarify this doubt.

From the difference map shown in **Fig. 4-7(c)** the disconnected oil (bright) blobs can be observed and the absence of spreading oil films is seen the final segmentation of the wet image is presented in **Fig. 4-7(d)** where red, blue, black and khaki colours indicate oil, water, gas and solid, respectively. In this case, after masking of the segmented dry image onto the wet image, all possible voxels in lieu of the aliasing artifact around the pore edges in the wet image were removed. This suggests that, for a negative spreading system, the chance of oil films on the gas phase may be negligible. A visual inspection of the 3D segmented wet image shows the absence of resolved oil films. These results are in agreement with earlier observations in the micro model and are consistent with those of other studies for the fluids system with negative spreading coefficient (Øren and

Pinczewski, 1995, Vizika et al., 1998). Oil lenses often appear to be trapped among water and air phases through many 2D slides. This suggests that the bulk oil volume could not be hydraulically connected through oil films within the sample. Although few exceptions of oil films around gas blobs were observed, these films would disappear if the sample was given further equilibration time.

In contrast to spreading system, the “intermediate phase” was not observed across the wet tomogram of core plug B2. For non-spreading system there are no connected spreading oil films. Therefore, equilibration time would be shorter as redistribution of oil and gas occurred very fast through filled pore and throats. This resulted in not having interface movement during the image acquisition time.

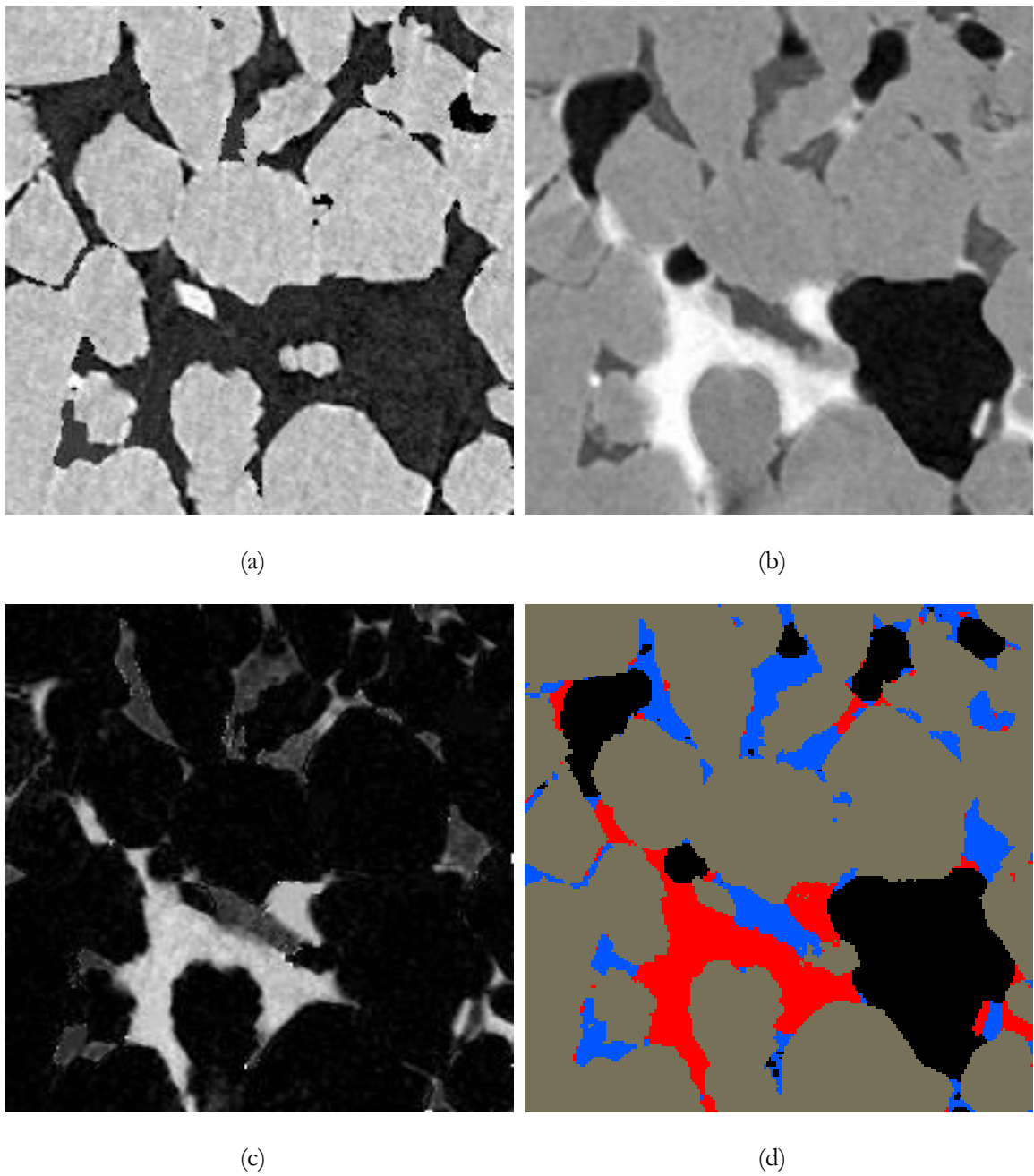


Fig. 4-7, Sections from negative spreading tomograms of core plug B2, $200 \times 200 \times 200$ voxels³ (a) dry, (b) wet. Solid, air, water and oil are grey, black, dark grey and bright, respectively. (c) Section representing subtraction of dry and wet images where oil shown in bright, water in grey and solid-air in black, (d) Segmented subset shows water in blue, air in black, oil in red and solid in khaki.

4.2. Characterisation of Three-Phase Fluids

The first purpose of quantitative analysis is to determine the 3D structural and topological information of the oil-water-gas system at different spreading conditions. The second purpose is to determine the 3D variations in spatial distribution and arrangement of each phase at both fluid sets. The third purpose is to visualise the spatial structures of the phases using the Drishti software. These are described in the subsequent sections.

4.2.1. Quantification of Spreading and Non-Spreading Systems

Table 4-1 gives the information of the samples used in this thesis. Core plug B1 has a measured porosity of 21.3 %, an imaged-based porosity of 24.5 %, and a measured permeability of 396mD. Core plug B2 has a measured porosity of 21.0 %, an imaged-based porosity of 24.1 %, and a measured permeability of 367mD (the experimental data is obtained from the MICP experiment on sister subsamples from original core samples (see section 3.2.1)).

Table 4-1, Rock Properties of the Core Plug Used and Imaged Saturation after Three-Phase Flood.							
Core Plug	Spreading Coefficient	Porosity(%)		Perm (md)	Average Saturation Across the imaged section		
		Exp	Image		Oil (%)	Water (%)	Gas (%)
B1	Positive	21.3	24.5	396	33	39	28
B2	Negative	21.0	24.1	367	35	26	40

The individual fluid saturations across the 2.5-mm central section of core plug B1 are computed by voxel counting. **Fig. 4-8** shows the saturation profiles of oil, water and gas across the imaged volume. The image analysis shows that average water saturation of (S_w^{image}) 0.4, oil saturation of 0.33 and gas saturation of 0.28. It can be observed that, while the variation of the gas saturation across the sample is fairly uniform, the oil and water saturations fluctuate considerably. This suggests that the gas phase occupied the largest pores and then broke through rapidly from the sample. The different water saturation suggests the different displacement mechanisms between oil and gas under different spreading conditions across the sample.

The individual fluid saturations across a 2.5-mm central section of core plug B2 were computed by voxel counting and these are shown in **Fig. 4-9**. The average saturations over the section for both positive and negative systems are given in **Table 4-1**. The oil saturations for the positive and negative spreading systems are almost similar, 0.33 and 0.35, respectively. However, the gas saturations are very different, 0.28 and 0.39. The positive spreading system required significantly less gas to reduce the oil saturation to a level similar to that of the negative spreading system. The corresponding difference in water saturations 0.4 and 0.26 for the positive and negative spreading systems suggest that gas-oil displacements were much more frequent for the positive spreading system. These observations are all consistent with the presence of spreading films for the positive spreading system and the absence of such films for the negative spreading system (Kalaydjian, 1992, Kalaydjian et al., 1993, Øren, 1993, Øren and Pinczewski, 1994, Blunt, 2000).

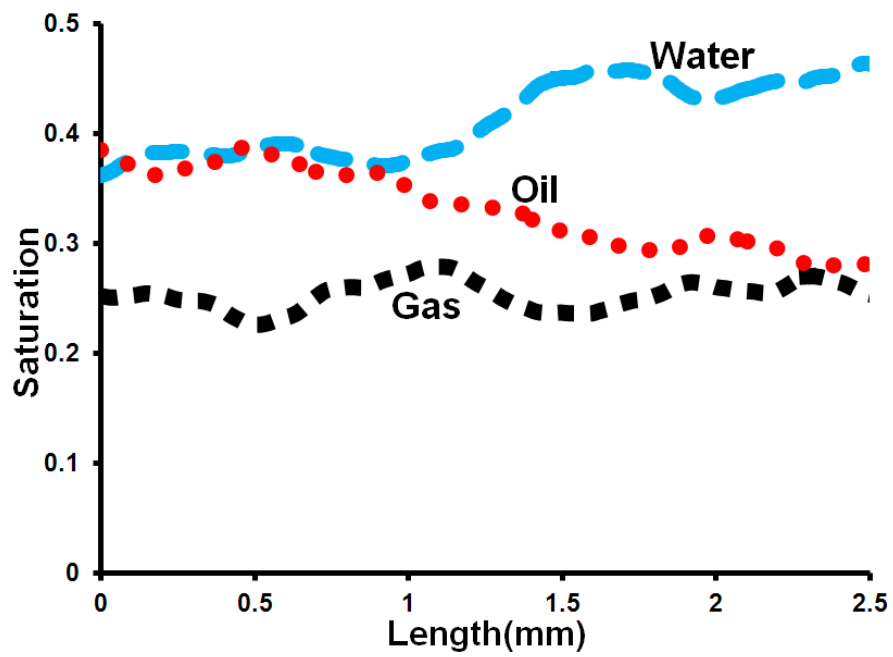


Fig. 4-8, A measure is made of the saturation of the oil, water and gas across the imaged section. The spreading coefficient was $+5.9\text{mNm}^{-1}$.

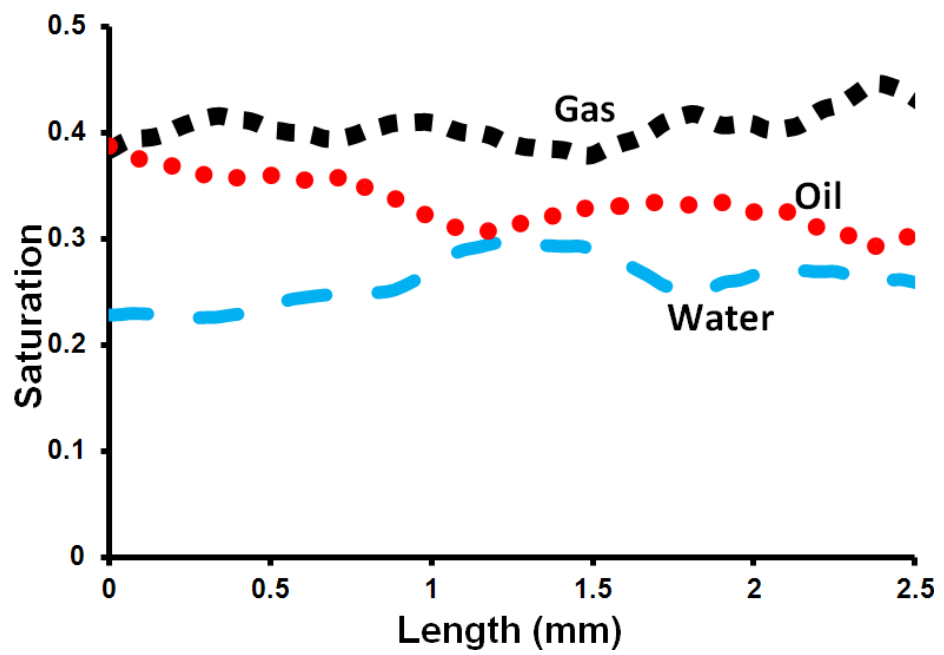
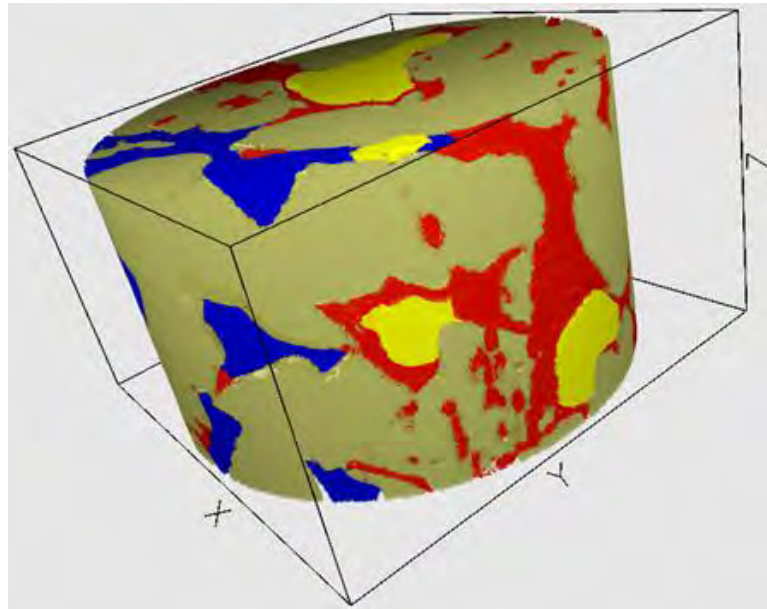


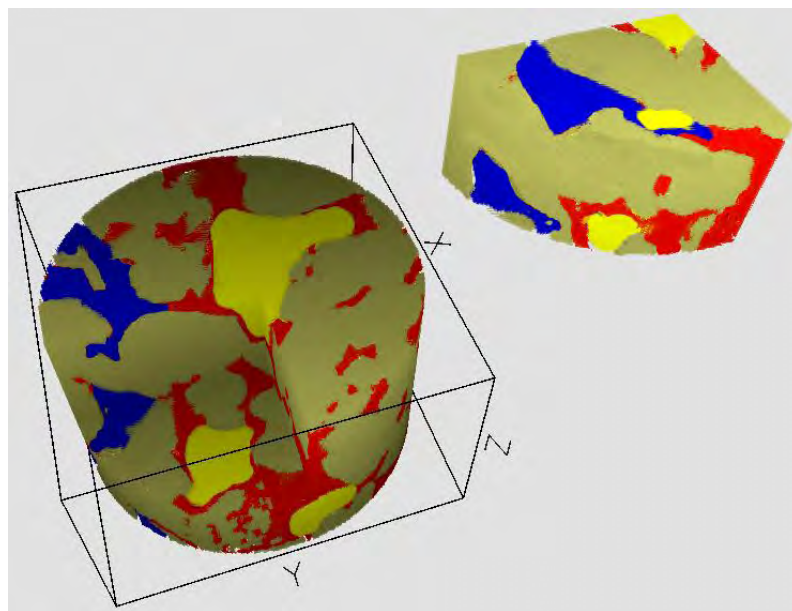
Fig. 4-9, A measure is made of the saturation of the oil, water and gas across the imaged section. The spreading coefficient was of -8.7 mNm^{-1} .

4.2.2. Three-dimensional Visualisation of Three-Phase Fluids

The segmented data was visualised for a qualitative analysis using Drishti (see section 3.5). **Fig. 4-10** represents 3D images (200^3 voxels) of water, oil and gas at the end of tertiary gas flooding for the positive spreading system. **Fig. 4-11** shows 3D images (200^3 voxels) of the same phases at the end of tertiary gas flooding for the negative spreading system. The oil is in red, water in blue and gas in yellow. A comparison of **Fig. 4-10** with **Fig. 4-11**, although thin oil films could not be resolved using Drishti, can visually show that, in the positive spreading system, the oil phase is spatially and hydraulically more connected than that in the negative spreading system. It can be seen that the non-wetting phase (air) resides in the larger pores and the wetting phase (water) in the smaller pores. The intermediate phase (oil) occupies the medium-size pores. However, this does not always occur without any full neighbourhood of the phases. Note that the Drishti software works as a transfer function by choosing the coordinate on intensity diagrams and transferring them to colours. The coordinates were chosen coarsely and not precise enough for small features such as oil films to be resolved and coloured.

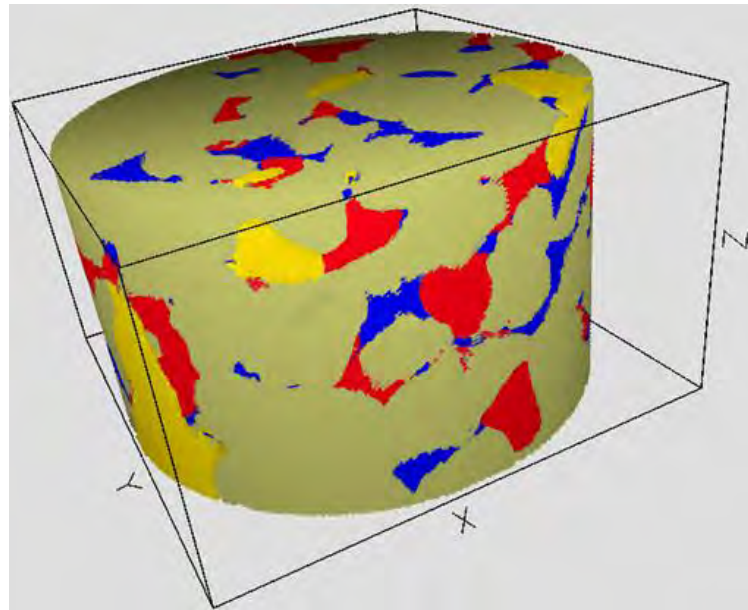


(a)

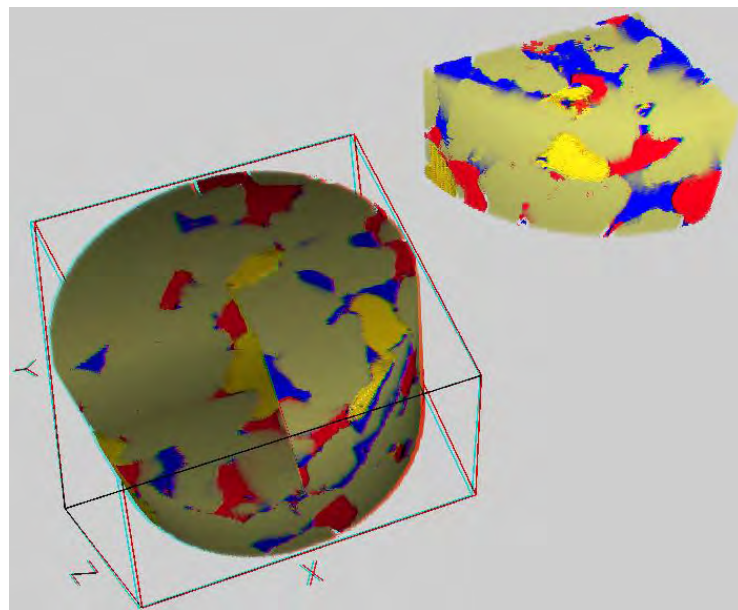


(b)

Fig. 4-10, Three-dimensional visualisation of oil (red), water (blue) and gas (yellow) for positive spreading system. The oil film (red) is spatially connected through thin films surrounded the gas phase (yellow). The oil film did form when the oil and gas phases have contacted to each other.



(a)



(b)

Fig. 4-11, Three-dimensional visualisation of oil (red), water (blue) and gas (yellow) for negative spreading system. The oil phase (red) is not spatially connected through oil film where it contacts the gas phase (yellow). As the spreading coefficient is negative, the oil phase did not form oil film around the gas phase which make the oil phase more disconnected compared to the system with positive spreading coefficient.

4.2.3. Analysis of Spatial Distribution of Fluids Using Network Model

A further statistical analysis of the spatial pore occupancy of the fluids for positive and negative spreading conditions was conducted by constructing the fluids network model and measurement of their characteristics using the segmented data. The procedure of the generation of the network model is described in section 3.4.1. This allows representing a set of statistics of each phase including the local pore volume equivalent radius (PVER) and pore radius (PR) to characterise the structure and topology of the oil, water and gas phases in the pore network. The PR represents the radius of the maximum Euclidean distance within the partitioned pore and gives an indication of the pore size based on spheres. Alternatively, pore size can be measured as the radius of a sphere which is equivalent to the pore volume and is denoted by the pore volume equivalent radius. The discrepancy between the sphere based pore radius and the volume based radius indicates the divergence of pore shape away from sphericity (Ghous, 2010).

Fig. 4-12 shows the volume-weighted characteristic plots of PR and PVER for water, gas and oil distributed within core plug B1. **Fig. 4-12(a)** shows PR of water in a range of 0.45-96 μm with a mean value of 10.5 μm whereas the PVER of water gives a range of 0.26-99 μm with a mean value of 13.0 μm (**Fig. 4-12(b)**). As expected, the gas phase occupied the larger pores with a PR distribution ranging between 4.3-118.4 μm and a mean value of 18.4 μm . The PVER for the gas distribution ranged between 2.5-148 μm with a mean of 21.8 μm . Contrary to expectation that the oil phase should occupy medium-size pore, the oil phase resided in the pores of the same size as water. The oil phase occupied the pores of radii varying between 4.3-87.3 μm with a mean of 9.6 μm . The PVER mean value for oil was 12.2 μm . This may be explained by a higher saturation of water (~39%) than oil (~ 33%).

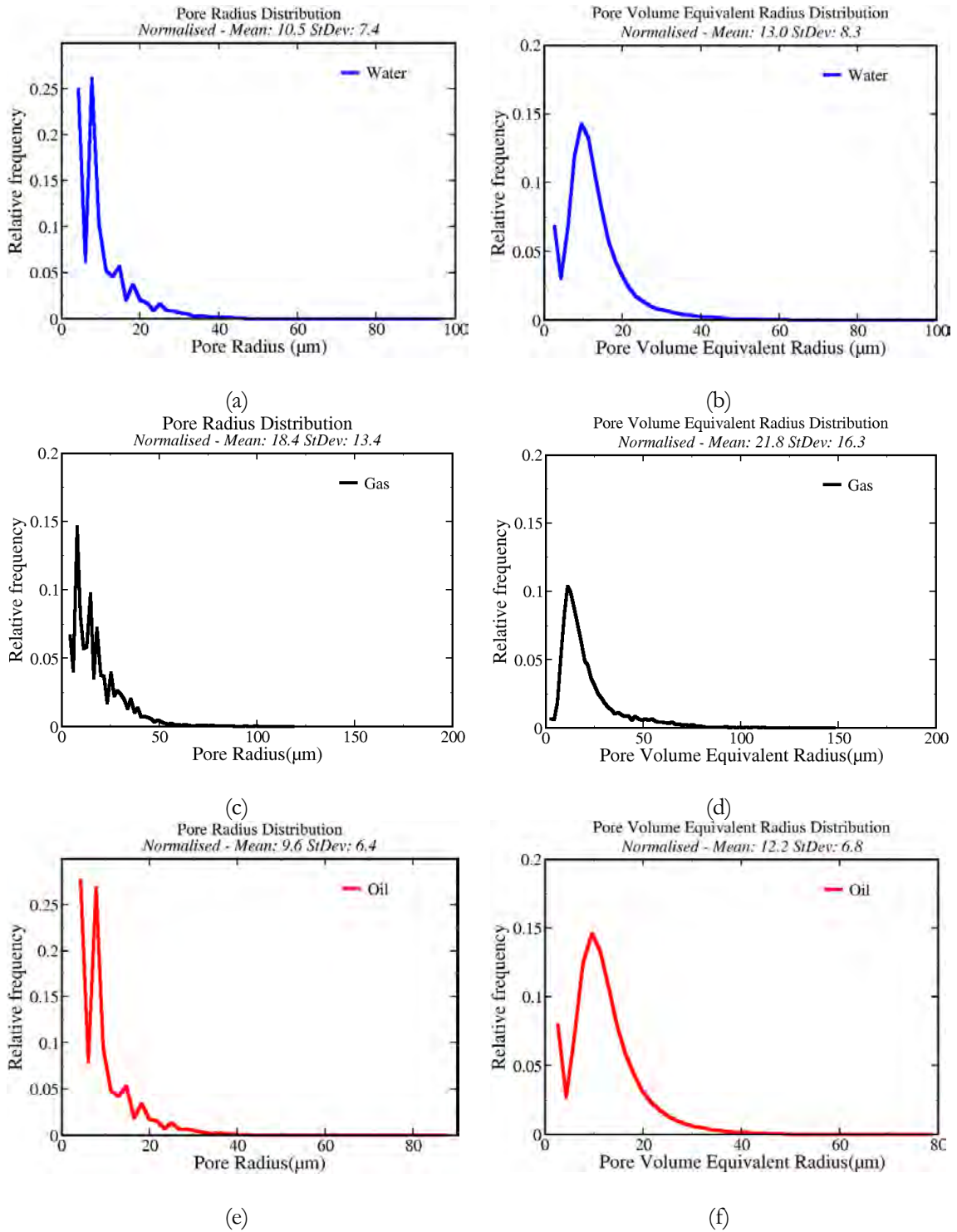


Fig. 4-12, Quantitative characteristics of water, gas and oil spatial distributions across 3D imaged volume of B1: pore radius and pore volume equivalent radius distributions of (a)-(b): water, (c)-(d): gas, and (e)-(f): oil. The fluids displayed a positive spreading coefficient ($C_s = + 5.9 \text{ mNm}^{-1}$).

These characteristic plots indicate that the largest pores are most likely occupied by gas as compared with water and oil. However, the preference of distribution could be affected by fluid fractions in the sample.

Volume-weighted network properties for the imaged volume of core plug B2 is shown in **Fig. 4-13**. As shown, according to PR (mean value 11.1 μm) and PVER (mean value 15.7 μm), water distributed in the smallest pores of the 3D pore network. In contrast, as shown in Fig. 4-13(c), the gas phase occupied the largest pores with a PR ranging from 7-162 μm and with a mean of 20.0 μm . Although, the range of PVER for the gas phase is approximately similar to the range of its PR, it has a greater mean of 26.7 μm (see Fig. 4-13(d)). The PR plot for oil, Fig. 4-13(e), indicates that oil distributed in the pores with a radius ranging from 4.95 μm to 68 μm with a mean of 14.0 μm . The PVER mean value for the oil phase is 17.8 μm . This means that the oil phase occupied the larger pores compared to water.

These measurements of the 3D fluid distribution revealed the tendency of the gas phase, as the most non-wetting phase, to occupy the largest pores, the tendency of the water phase, as the most wetting phase, to occupy the smallest pores and the tendency of the oil phase, as the intermediate phase, to occupy the pores of the intermediate size in 3D. These are consistent with past work of 2D visualisation of oil, water and gas in glass micro models (Øren and Pinczewski, 1995).

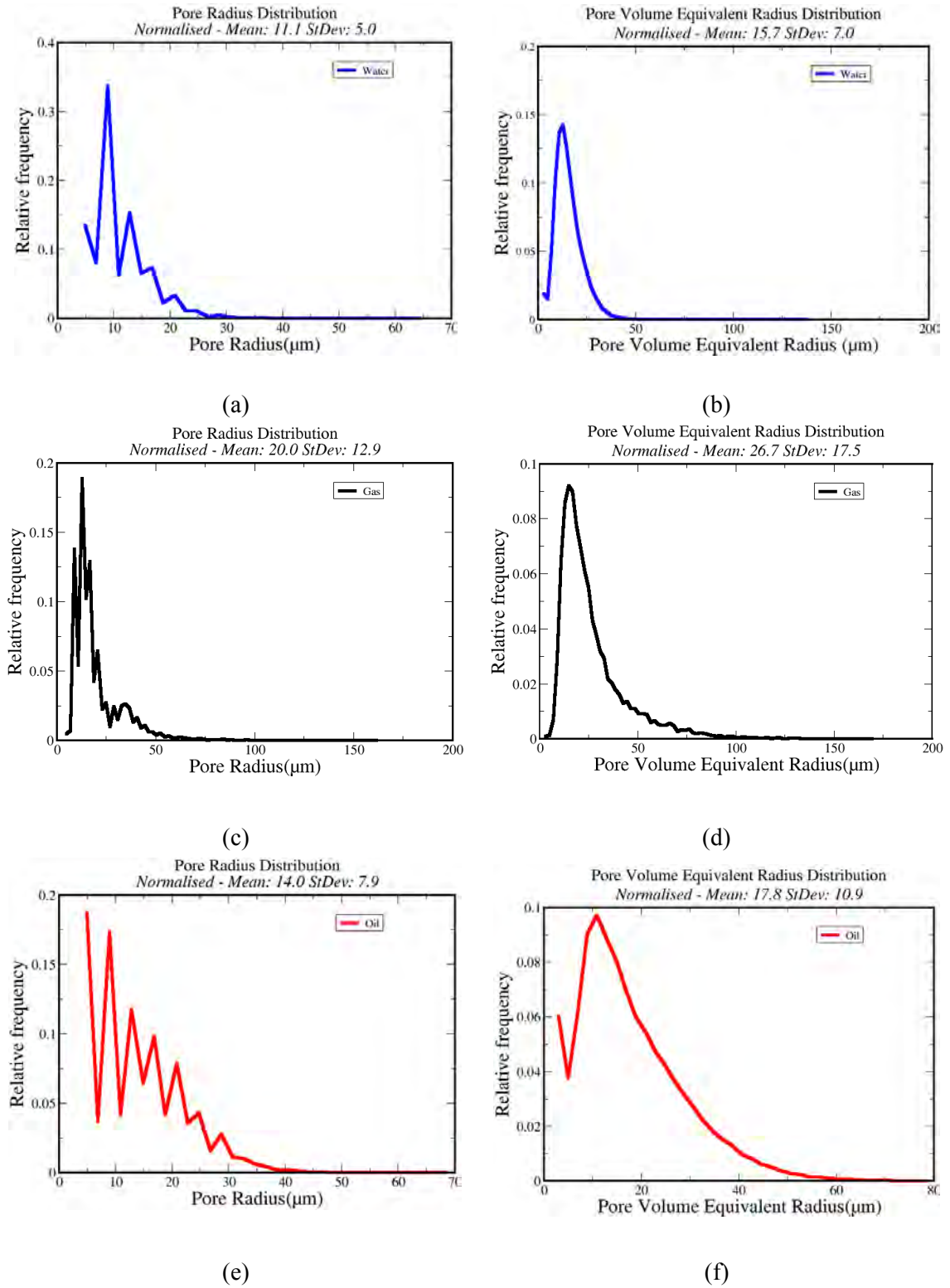


Fig. 4-13, Quantitative characteristics of water, gas and oil spatial distributions across 3D imaged volume of B2: pore radius and pore volume equivalent radius distributions of (a)-(b): water, (c)-(d): gas, and (e)-(f): oil. The fluids displayed a negative spreading coefficient ($C_s = -8.7 \text{ mNm}^{-1}$).

4.3. Computational Analysis of Connectivity for Three-Phase Fluids

To obtain a quantitative measure of spatial connectivity and continuity of the oil, water and gas phases in the pore space after the tertiary gas flooding, the Euler characteristic (described in section 3.4.2) was computed for each of the phases on the segmented images (subset of $700 \times 700 \times 700$ voxels³) using the procedure described in section 3.4.2. The Euler characteristic quantifies the connectivity of elements in a network. It is negative for highly connected networks and positive for a network of isolated elements. An important advantage of this approach is that it provides an unbiased estimation of connectivity from local measurements on a digitised image (Mecke and Wagner, 1991).

Table 4-2 presents the computed Euler characteristics for the positive and negative spreading systems. During the time of imaging (approximately 4 hours after the completion of the tertiary gas flooding experiments) the only phase to remain connected is the oil phase for the positive spreading system. Although both systems are strongly water-wet the computed Euler characteristics for the water phase are positive for both positive and negative spreading systems because the wetting films which connect the water phase are too thin to be resolved by the imaging system used. The Euler characteristics for the gas phase are also positive for both spreading systems indicating that the gas phase is also disconnected. Since gas is the injected phase it was expected to be continuous throughout the sample. However, in the time between the removal of the plug from the flooding apparatus and the commencement of scanning, the fluids relaxed and re-distributed. The gas phase became disconnected as a result of snap-off at pore throats. This is what is expected for the non-wetting fluid in a strongly water-wet medium.

The Euler characteristics for the oil phase are negative for the positive spreading system indicating continuity of the oil phase throughout the imaged volume and positive

for the negative spreading system indicating a disconnected oil phase. This confirms the previously discussed image-based observations of the presence of oil spreading films for the positive spreading system and the absence of films for the negative spreading system.

In order to examine the connectivity of the phases in a smaller imaged volume (block of 350^3 voxels), the imaged volumes of 700^3 voxels were divided into eight blocks of 350^3 voxels and their corresponding Euler number was computed for each of the phases. **Table 4-3** compares the Euler characteristics for each of the blocks for the gas, oil and water phases for the positive and negative spreading systems. The Euler characteristic's numbers for the oil phase was negative for the spreading system and was positive for the non-spreading system for all blocks. This indicates the continuity of the oil phase at different locations when the spreading coefficient was positive and the discontinuity of the oil phase when the spreading coefficient was negative even in smaller volumes. The continuity of the oil phase in the spreading system suggests the presence of the oil films throughout the sample. Table 4-3 exhibits that the gas and water phases are still disconnected even in a smaller block of the imaged volume. As it has been discussed above, the gas phase became disconnected during the period of relaxation as a result of snap-off occurred at pore throats. Although, the water phase is expected to be continuous in a strongly water-wet medium, the water films which connect the water bulks are too thin to be resolved using this image system.

Table 4-2, Euler Characteristics (μm^{-3})

	Oil	Water	Gas
Positive Spreading System	-6.7×10^{-6}	2.0×10^{-6}	4.8×10^{-8}
Negative Spreading System	1.1×10^{-6}	8.9×10^{-7}	2.2×10^{-6}

Table 4-3, Euler Characteristics (μm^{-3})

Cube No.	Spreading Coefficients	Oil	Water	Gas
1	$S > 0$	-8.4×10^{-6}	3.2×10^{-6}	6.1×10^{-8}
1	$S < 0$	2.3×10^{-6}	1.4×10^{-6}	7.9×10^{-7}
2	$S > 0$	-6.4×10^{-6}	7.6×10^{-7}	9.5×10^{-8}
2	$S < 0$	2.1×10^{-6}	1.2×10^{-6}	6.1×10^{-7}
3	$S > 0$	-6.9×10^{-6}	1.7×10^{-6}	6.0×10^{-8}
3	$S < 0$	1.9×10^{-6}	7.3×10^{-7}	1.2×10^{-7}
4	$S > 0$	-7.6×10^{-6}	1.7×10^{-6}	1.0×10^{-7}
4	$S < 0$	2.5×10^{-6}	6.8×10^{-7}	1.5×10^{-6}
5	$S > 0$	-5.7×10^{-6}	2.3×10^{-6}	9.2×10^{-9}
5	$S < 0$	2.4×10^{-6}	5.6×10^{-7}	1.3×10^{-6}
6	$S > 0$	-5.0×10^{-6}	1.6×10^{-6}	2.1×10^{-8}
6	$S < 0$	2.6×10^{-6}	5.7×10^{-7}	1.3×10^{-6}
7	$S > 0$	-6.6×10^{-6}	2.4×10^{-6}	2.3×10^{-8}
7	$S < 0$	2.1×10^{-6}	4.2×10^{-7}	1.3×10^{-6}
8	$S > 0$	-7.2×10^{-6}	2.6×10^{-6}	1.1×10^{-8}
8	$S < 0$	1.8×10^{-6}	3.6×10^{-7}	1.3×10^{-6}

Chapter 5

Conclusions and Recommendations

This thesis has demonstrated for the first time that three-phase fluids distributed in an actual porous medium could be imaged using a high resolution X-ray micro tomography and detailed three-dimensional distributions of three-phase fluids in the porous system could be obtained. This is something that has never been done before at a very high resolution of imaging ($\sim 3\mu\text{m}$).

Experimental and numerical results indicated that it is possible to visualise and characterise the complex three-dimensional morphology of the oil, water and gas distributions and their connectivity and continuity in the actual rock from X-ray micro-CT images. Findings from this thesis could contribute to enhance the current three-dimensional three-phase network models of capillary-driven flow which are now used to estimate three-phase relative permeabilities, residual saturations and the pore-scale distribution of fluids in porous systems.

The thesis leads to the following conclusions:

1. Positive spreading oil, water and gas systems which clearly display oil spreading behaviour in strongly water-wet two-dimensional glass micromodels also display this behaviour in strongly water-wet actual porous rock (Bentheimer sandstone).

2. Negative spreading oil, water and gas systems which display no oil spreading behaviour in strongly water wet two-dimensional glass micromodels also display this behaviour in strongly water-wet Bentheimer sandstone.
3. The subtraction method of registered normalised dry and wet images proved the existence of the oil films in Bentheimer sandstone for positive spreading system and absence of such films for negative spreading system.
4. Topological measures such as the Euler characteristic which are readily computed from segmented three-dimensional tomographic image data confirm the existence of continuous oil films in strongly water-wet Bentheimer sandstone for positive spreading systems. They also confirm the absence of such films for negative spreading systems.
5. There is a strong correspondence between fluid distribution and geometry and topology of the porous system. The non-wetting phase tends to occupy the largest pores, while the wetting phase occupies the smallest pores. The intermediate phase tends to occupy the pores of the intermediate size where all the phases are present.
6. Although large pores have a higher likelihood to be occupied by the most non-wetting phase than wetting and intermediate phases, it is likely that the large pores not to be occupied by the non-wetting phase. The reason is that pore size magnitude is not a sufficient condition for the non-wetting phase to reside. There must be a full neighbourhood to form a non-wetting phase cluster.
7. The positive spreading system required significantly less gas to reduce the oil saturation to a level similar to that of the negative spreading system. The corresponding difference in water saturations for the positive and negative systems

suggests that gas-oil displacements were much more frequent for the positive spreading system.

While methodologies and workflows have been developed, the data collected can only be considered the start of a large scale study of tertiary gas flooding of reservoir rocks under various conditions at the pore scale. The following recommendations are made for potential future research:

1. The role of spreading oil films in ultimate oil recovery should be examined in actual porous media by the quantification of three-phase fluid distribution over subsequent gas tertiary injections for both positive and negative spreading systems.
2. The experimental setup and X-ray facility should be integrated so that the rock can be imaged while flooding takes place. This will prevent the phases from redistributing and relaxing during X-ray imaging. Imaging of the three-phase fluid system on these conditions will also help to visualise the spatial displacement mechanisms in actual porous media.
3. Direct imaging of three-phase fluids in strongly water-wet sandstone porous media can be extended to weak water-wet and mixed-wet rock samples.
4. Fluid distributions and displacement mechanisms in actual porous media during water-alternating-gas injection (WAG) can also be investigated using the X-ray micro-CT technology.
5. The ability to accurately visualise and resolve the oil films with thin thickness and three-phase fluid distributions through the porous rock at static points after three-phase immiscible displacement was a great step forward in micro-CT imaging

analysis. This has provided the ability to extend two-phase relative permeability measurement using micro-CT imaging to three-phase relative permeability. To measure two-phase relative permeability, lattice-Boltzmann (Martys, and Chen (1996); Arns et al (2003, 2004)) method has been used because it is a mesoscopic approach to computational fluid dynamics and has found much success in fluid-flow applications of porous media. It is simple in form, can be adapted to complex flow geometries and can incorporate complex fluid-solid, fluid-gas and fluid-fluid interfaces. The discretised microstructure of the oil films defined by a micro-CT image can also incorporate in the numerical computation (lattice-Boltzmann). The physical boundary condition at solid-fluid and fluid-fluid interfaces in numerical computation can be either considered or not. Three-phase relative permeability is out of scope of this study; however, the findings from this study can be used as initial materials for further work on computation of three-phase flow permeability using micro-CT imaging.

References

- Adamson, A. W. 1990 *Physical Chemistry of Surfaces*, New York : Wiley
- Alvarado, F. E., Grader, A. S., Karacan, O. and Halleck, P. M. 2004. Visualization of three phases in porous media using micro computed tomography. *Petrophysics*, 45, 490-498.
- Arhatari, B. D., Mancuso, A. P., Peele, A. G. and Nugent, K. A., 2004. Phase contrast radiography: Image modeling and optimization. *Review of Scientific Instruments*, 75, 5271-5276.
- Arhatari, B. D., Nugent, K. A., Peele, A. G. and Thornton, J., 2005. Phase contrast radiography. II. Imaging of complex objects. *Review of Scientific Instruments*, 76, 113704-6.
- Arns, C. H., Knackstedt, M., Pinczewski, W. V. and Mecke, K. R., 2001. Euler-Poincaré characteristics of classes of disordered media. *Physical Review E*, 63, 031112.
- Arns, C. H., Knackstedt, M. A. and Pinczewski, W. V., 2002. Accurate Vp:Vs relationship for dry consolidated sandstones. *Geophys. Res. Lett.*, 29, 1202.
- Arns, C. H., Knackstedt, M. A. and Mecke, K. R., 2004. Characterisation of irregular spatial structures by parallel sets and integral geometric measures. *Colloids and Surfaces A: Physicochemical and Engineering Aspects*, 241, 351-372.
- Arns, C. H., Knackstedt, M. A. and Mecke, K., 2010. 3D structural analysis: sensitivity of Minkowski functionals. *Journal of Microscopy*, 240, 181-196.
- Arns, J.Y., et al., *Relative permeability from tomographic images; effect of correlated heterogeneity*. Journal of Petroleum Science and Engineering, 2003. 39(3): p. 247-259.
- Arns, C.H., et al., *Virtual permeametry on microtomographic images*. Journal of Petroleum Science and Engineering, 2004. 45(1-2): p. 41-46.
- Blunt, M. J., Fenwick, D. H. and Zhou, D. 1994. What Determines Residual Oil Saturation in Three-Phase Flow? *SPE/DOE Improved Oil Recovery Symposium*. Tulsa, Oklahoma: 1994 Copyright 1994, Society of Petroleum Engineers, Inc.
- Blunt, M., , Z., Dengen and Fenwick, D., 1995. Three-phase flow and gravity drainage in porous media. *Transport in Porous Media*, 20, 77-103.
- Blunt, M. J. 2000. An empirical model for three-phase relative permeability. *SPE Journal*, 5. Page 435-445.
- Candès, E. J. and Donoho, D. L. 1999. Ridgelets: a key to higher-dimensional intermittency. *Philos. Trans. R. Soc. Lond. Ser. A-Math. Phys. Eng. Sci.* 357 (1999), 2495-2509.
- Caselles, V., Kimmel, R. and Sapiro, G., 1997. Geodesic Active Contours. *International Journal of Computer Vision*, 22, 61-79.
- Chatzis, I. and Dullien, F. a. L. 1985. The modeling of mercury porosimetry and the relative permeability of mercury in sandstones using percolation theory. *Journal Name: Int. Chem. Eng.; (United States); Journal Volume: 25:1, Medium: X; Size: Pages: 47-66.*

- Chatzis, I., Kantzas, A. and Dullien, F. a. L., 1988. On the Investigation of Gravity-Assisted Inert Gas Injection Using Micromodels, Long Berea Sandstone Cores, and Computer-Assisted Tomography. *SPE Annual Technical Conference and Exhibition*. Houston, Texas: 1988.
- Coifman, R. R. and Donoho, D. L., 1995. Translation-invariant de-noising. *LECTURE NOTES IN STATISTICS-NEW YORK-SPRINGER VERLAG*, 125-125.
- Creagh, D. C. and Hubbell, J. H., 1990. Problems associated with the measurement of X-ray attenuation coefficients. II. Carbon. Report on the International Union of Crystallography X-ray Attenuation Project. *Acta Crystallographica Section A*, 46, 402-408.
- Culligan, K. A., Wildenschild, D., Christensen, B. S. B., Gray, W. G. and Rivers, M. L., 2006. Pore-scale characteristics of multiphase flow in porous media: A comparison of air-water and oil-water experiments. *Advances in Water Resources*, 29, 227-238.
- De Witte, Y., Boone, M., Vlassenbroeck, J., Dierick, M., Masschaele, B., Van Hoorebeke, L. and Cnudde, V. Correcting phase contrast artefacts in X-ray CT imaging. *Biomedical Imaging: From Nano to Macro, 2009. ISBI '09. IEEE International Symposium on, June 28 -July 1 2009 2009*. 574-577.
- Dong, M., Dullien, F. a. L. and Chatzis, I., 1995. Imbibition of Oil in Film Form over Water Present in Edges of Capillaries with an Angular Cross Section. *Journal of Colloid and Interface Science*, 172, 21-36.
- Dumore, J. M. and Schols, R. S., 1974. Drainage Capillary-Pressure Functions and the Influence of Connate Water. *Society of Petroleum Engineers Journal*, 14, 437-444.
- Feali, M., Pinczewski, W., Cinar, Y., Arns, C. H., Arns, J.-Y., Francois, N., Turner, M. L., Senden, T. and Knackstedt, M. A. 2012. Qualitative and Quantitative Analyses of the Three-Phase Distribution of Oil, Water, and Gas in Bentheimer Sandstone by Use of Micro-CT Imaging. *SPE Reservoir Evaluation & Engineering*, 15, pp. 706-711.
- Feldkamp, L. A., Davis, L. C. and Kress, J. W., 1984. Practical cone-beam algorithm. *J. Opt. Soc. Am. A*, 1, 612-619.
- Fenwick, D. H. and Blunt, M. J., 1998. Three-dimensional modeling of three phase imbibition and drainage. *Advances in Water Resources*, 21, 121-143.
- Frangakis, A. S., Stoschek, A. and Hegerl, R., 2001. Wavelet transform filtering and nonlinear anisotropic diffusion assessed for signal reconstruction performance on multidimensional biomedical data. *Biomedical Engineering, IEEE Transactions on*, 48, 213-222.
- Ghous, A. 2010. *3D imaging and modeling of carbonate core at multiple scales*. University of New South Wales. Petroleum Engineering , 2010.
- Hagoort, J., 1980. Oil Recovery by Gravity Drainage. *Society of Petroleum Engineers Journal*, 20, 139-150.
- Helland, J. O. and Skjæveland, S. M., 2006. Three-phase mixed-wet capillary pressure curves from a bundle of triangular tubes model. *Journal of Petroleum Science and Engineering*, 52, 100-130.
- Hilpert, M. and Miller, C. T., 2001. Pore-morphology-based simulation of drainage in totally wetting porous media. *Advances in Water Resources*, 24, 243-255.

- Hirasaki, G. J. 1993. Structural interactions in the wetting and spreading of van der Waals fluids. *Journal of Adhesion Science and Technology* [Online], 7. Available: <http://booksandjournals.brillonline.com/content/10.1163/156856193x00718>.
- Iassonov, P., Gebrenegus, T. and Tuller, M., 2009. Segmentation of X-ray computed tomography images of porous materials: A crucial step for characterization and quantitative analysis of pore structures. *Water Resources Research*, 45, W09415.
- Iglauer, S., Paluszny, A. and Blunt, M. J., 2013. Simultaneous oil recovery and residual gas storage: A pore-level analysis using in situ X-ray micro-tomography. *Fuel*, 103, 905-914.
- Jacobs, K., Seemann, R. and Mecke, K., 2000. Dynamics of Structure Formation in Thin Liquid Films: A Special Spatial Analysis. *Statistical Physics and Spatial Statistics*. In: MECKE, K. & STOYAN, D. (eds.). Springer Berlin / Heidelberg.
- Jones, A. C., A., Christoph H., H., Dietmar W., M., Bruce K., S., Adrian P. and K., Mark A., 2009. The correlation of pore morphology, interconnectivity and physical properties of 3D ceramic scaffolds with bone ingrowth. *Biomaterials*, 30, 1440-1451.
- Kalaydjian, F. J.-M., 1992. Performance and Analysis of Three-Phase Capillary Pressure Curves for Drainage and Imbibition in Porous Media. *SPE Annual Technical Conference and Exhibition*. Washington, D.C.
- Kalaydjian, F. J.-M., Moulu, J. C., Vizika, O. and Mungerud, P. K., 1993. Three-Phase Flow in Water-Wet Porous Media: Determination of Gas/Oil Relative Permeabilities Under Various Spreading Conditions. *SPE Annual Technical Conference and Exhibition*. Houston, Texas: 1993 Copyright 1993, Society of Petroleum Engineers, Inc.
- Kantzas, A., Chatzis, I. and Dullien, F. a. L., 1988a. Enhanced Oil Recovery by Inert Gas Injection. *SPE Enhanced Oil Recovery Symposium*. Tulsa, Oklahoma: 1988.
- Kantzas, A., Chatzis, I. and Dullien, F. a. L., 1988b. Mechanisms of Capillary Displacement of Residual Oil by Gravity-Assisted Inert Gas Injection. *SPE Rocky Mountain Regional Meeting*. Casper, Wyoming: 1988 Copyright 1988, Society of Petroleum Engineers, Inc.
- Karpyn, Z. T., Piri, M. and Gurpreet, S., 2010. Experimental investigation of trapped oil clusters in a water-wet bead pack using X-ray microtomography. *Water Resour. Res.*, 46, W04510.
- Katsevich, A., 2002a. Analysis of an exact inversion algorithm for spiral cone-beam CT. *2002 Phys. Med. Biol.* 47 2583.
- Katsevich, A., 2002b. Theoretically Exact Filtered Backprojection-Type Inversion Algorithm for Spiral CT. *SIAM Journal on Applied Mathematics*, 62, 2012-2026.
- Keller, A. A., Blunt, M. J. and Roberts, A. P. V., 1997. Micromodel Observation of the Role of Oil Layers in Three-Phase Flow. *Transport in Porous Media*, 26, 277-297.
- Ketcham, R. A. and Carlson, W. D., 2001. Acquisition, optimization and interpretation of X-ray computed tomographic imagery: applications to the geosciences. *Computers & Geosciences*, 27, 381-400.
- Kumar, M., 2009. *Multiphase Flow in Reservoir Cores Using Digital Core Analysis*. Australian National University, PhD Dissertation.
- Kumar, M. and Fogden, A., 2009. Patterned Wettability of Oil and Water in Porous Media. *Langmuir*, 26, 4036-4047.

- Kumar, M., Senden, S., T., Knackstedt, M. A., Latham, S., Pinczewski, W. V., Sok, R. M., Sheppard, A. P. and Turner, M. L., 2009b. Imaging of pore scale distribution of fluids and wettability. *Petrophysics*, 50, 311-321.
- Kumar, M., Sok, R. M., Knackstedt, M., Latham, S., Senden, T. J., Sheppard, A. P., Varslot, T. and Arns, C. H., 2009a. Mapping Fluid Distributions In 3D At the Pore Scale: Quantifying the Influence of Wettability And Saturation History On Rock Resistivity. *SPWLA 50th Annual Logging Symposium*. The Woodlands, Texas: 2009, held jointly by the Society of Petrophysicists and Well Log Analysts (SPWLA) and the submitting authors.
- Landry, C. J., Karpyn.Z.T and Piri.M., 2011. Pore-Scale analysis of trapped immiscible fluid structures and fluid interfacial areas in oil-wet and water-wet packs. *GEofluids(2001)11,209-227*.
- Latham, S., Varslot, T. and Sheppard, A. P., 2008. Image Registration: Enhancing and calibrating X-ray Micro-CT Imaging, *International Symposium of the Society of Core Analysts held in Abu Dhabi, UAE 29 October-2 November, 2008*.
- Lerdahl, T. R., Oren, P. E. and Bakke, S., 2000. A Predictive Network Model for Three-Phase Flow in Porous Media. *SPE/DOE Improved Oil Recovery Symposium*. Tulsa, Oklahoma.
- Lindquist, W., Lee, S., Coker, D., Jones, K. and Spanne, P., 1996. Medial axis analysis of void structure in three-dimensional tomographic images of porous media. *J Geophys Res* 1996;101(B4):8297-310.
- Mallat, S. G., 1989. A theory for multiresolution signal decomposition: the wavelet representation. *Pattern Analysis and Machine Intelligence, IEEE Transactions on*, 11, 674-693.
- Mayo, S., Davis, T., Gureyev, T., Miller, P., Paganin, D., Pogany, A., Stevenson, A. and Wilkins, S., 2003. X-ray phase-contrast microscopy and microtomography. *Opt. Express*, 11, 2289-2302.
- Martys, N.S. and H. Chen, *Simulation of multicomponent fluids in complex three-dimensional geometries by the lattice Boltzmann method*. Physical Review E, 1996. **53**(1): p. 743-750.
- Mecke, K. and Arns, C. H., 2005. Fluids in porous media: A morphometric approach. *Journal of Physics Condensed Matter*, 17, S503-S534.
- Mecke, K. R. and Wagner, H., 1991. Euler characteristic and related measures for random geometric sets. *Journal of Statistical Physics*, 64, 843-850.
- Øren, P. E. 1993. *Recovery of waterflood residual oil by immiscible gas flooding*, The University of New South Wales, School of Petroleum Engineering, PhD Dissertation.
- Øren, P. E., Billiotte, J. and Pinczewski, W. V., 1992. Mobilization of Waterflood Residual Oil by Gas Injection for Water-Wet Conditions. *SPE Formation Evaluation*, 7, 70-78.
- Øren, P. E. and Pinczewski, W. V., 1992. The Effect of Wettability and Spreading Coefficients on the Recovery of Waterflood Residual Oil by Miscible Gasflooding. *SPE 24881 Presented at the 67th Annual Technical Conference and Exhibition*
- Øren, P. E. and Pinczewski, W. V. 1994. The Effect of Wettability and Spreading Coefficients on the Recovery of Waterflood Residual Oil by Miscible Gasflooding. *SPE Formation Evaluation*, 9, Page 149-156.

- Øren, P. E. and Pinczewski, W. V., 1995. Fluid distribution and pore-scale displacement mechanisms in drainage dominated three-phase flow. *Transport in Porous Media*, 20, 105-133.
- Pereira, G. G., Pinczewski, W. V., Chan, Y. C., Paterson, L. and Øren, P. E., 1996. Pore-scale network model for drainage-dominated three-phase flow in porous media. *Transport in Porous Media*, 24, 167-201.
- Perona, P. and Malik, J., 1990. Scale-space and edge detection using anisotropic diffusion. *Pattern Analysis and Machine Intelligence, IEEE Transactions on*, 12, 629-639.
- Piri, M., 2003. *Pore-Scale Modelling of Three-Phase Flow*. Department of Earth Science and Engineering, Imperial College London, PhD Dissertation.
- Piri, M. and Blunt, M. J., 2002. Pore-scale modeling of three-phase flow in mixed-wet systems. *SPE Annual Technical Conference and Exhibition*. San Antonio, Texas: Copyright 2002, Society of Petroleum Engineers Inc.
- Piri, M. and Blunt, M. J., 2004. Three-phase threshold capillary pressures in noncircular capillary tubes with different wettabilities including contact angle hysteresis. *Physical Review E*, 70, 061603.
- Piri, M. and Blunt, M. J., 2005. Three-dimensional mixed-wet random pore-scale network modeling of two- and three-phase flow in porous media. II. Results. *Physical Review E*, 71, 026302.
- Pudney, C., 1998. Distance-Ordered Homotopic Thinning: A Skeletonization Algorithm for 3D Digital Images. *Computer Vision and Image Understanding*, 72, 404-413.
- Reddinger, W., 1998. *CT Image Quality*. Available from: http://www.e-radiography.net/merit/CT_IQ.pdf
- Roberts, N., Reed, M. and Nesbitt, G., 1997. Estimation of the connectivity of a synthetic porous medium. *Journal of Microscopy*, 187, 110-118.
- Saito, T. and Toriwaki, J.-I. 1994. New algorithms for euclidean distance transformation of an n-dimensional digitized picture with applications. *Pattern Recognition*, 27, 1551-1565.
- Sakellariou, A., Sawkins, T. J., Senden, T. J. and Limaye, A., 2004a. X-ray tomography for mesoscale physics applications. *Physica A: Statistical Mechanics and its Applications*, 339, 152-158.
- Sakellariou, A., Senden, T. J., Sawkins, T. J., Knackstedt, M. A., Turner, M. L., Jones, A. C., Saadatfar, M., Roberts, R. J., Limaye, A., Arns, C. H., Sheppard, A. P. and Sok, R. M., 2004b. An x-ray tomography facility for quantitative prediction of mechanical and transport properties in geological, biological and synthetic systems. 473-484.
- Schnaar, G. and Brusseau, M. L., 2005. Pore-Scale Characterization of Organic Immiscible-Liquid Morphology in Natural Porous Media Using Synchrotron X-ray Microtomography. *Environmental Science & Technology*, 39, 8403-8410.
- Schnaar, G. and Brusseau, M. L., 2006. Characterizing pore-scale configuration of organic immiscible liquid in multiphase systems with synchrotron X-Ray microtomography. *Vadose Zone Journal*, 5, 641-648.
- Sheppard, A. P., Sok, R. M. and Holger, A., 2004. Techniques for image enhancement and segmentation of tomographic images of porous materials. *Physica A: Statistical Mechanics and its Applications*, 339, 145-151.

- Sheppard, A. P., Sok.M.R and Averdunk.H., 2005. International Symposium of the Society of Core Analysts held in Toronto, 21-25 August 2005
- Silin, D. and Patzek, T., 2006. Pore space morphology analysis using maximal inscribed spheres. *Physica A: Statistical Mechanics and its Applications*, 371, 336-360.
- Soll, W. E., , C., M. A. and , W., J. L., 1993. Micromodel studies of three-fluid porous media systems: Pore-scale processes relating to capillary pressure-saturation relationships. *Water Resour. Res.*, 29, 2963-2974.
- Valvatne, P., Piri, M., Lopez, X. and Blunt, M., 2005. Predictive Pore-Scale Modeling of Single and Multiphase Flow. *Transport in Porous Media*, 58, 23-41.
- Varslot, T., Kingston, A., Latham, S., Knackstadt, M. and Sheppard, A., 2011a. Combining High-Fidelity Helical Microtomography With Region-of-Interest Scanning for Improved Core Characterisation, *International Symposium of the Society of Core Analysts 2011*, ed. SCA, Society of Core Analysts, USA.
- Varslot, T., Kingston, A., Myers, G. and Sheppard, A., 2011b. High-resolution helical cone-beam micro-CT with theoretically-exact reconstruction from experimental data. *Medical Physics*, 38, 5459-5476.
- Varslot, T., Kingston, A., Sheppard, A. and Sakellariou, A.,2010. Fast high-resolution micro-CT with exact reconstruction methods. *In: STUART, R. S., ed., 2010. SPIE*, 780413.
- Vincent, L. and Soille, P., 1991. Watersheds in Digital Spaces: An Efficient Algorithm Based on Immersion Simulations. *IEEE Trans. Pattern Anal. Mach. Intell.*, 13, 583-598.
- Vizika, O., 1993. Effect of the spreading coefficient on the efficiency of oil recovery with gravity drainage. *Proceedings of the Symposium on Enhanced Oil Recovery, presented before the Division of Petroleum Chemistry, Inc., American Chemical Society, Denver, Colorado, 1993*. 380.
- Vizika, O. and Lombard, J.-M., 1996. Wettability and Spreading: Two key Parameters in Oil Recovery With Three-Phase Gravity Drainage. *SPE Reservoir Engineering*, 11, Page 56-60.
- Vizika, O., Rosenberg, E. and Kalaydjian, F., 1998. Study of wettability and spreading impact in three-phase gas injection by cryo-scanning electron microscopy. *Journal of Petroleum Science and Engineering*, 20, 189-202.
- Vogel, H.-J., 2002. Topological Characterization of Porous Media, Morphology of Condensed Matter. *In: MECKE, K. & STOYAN, D. (eds.)*. Springer Berlin / Heidelberg.
- Vogel, H. J. and Roth, K., 2001. Quantitative morphology and network representation of soil pore structure. *Advances in Water Resources*, 24, 233-242.
- Weickert, J., 1999. Coherence-Enhancing Diffusion Filtering. *International Journal of Computer Vision*, 31, 111-127.
- Wildenschild, D. and Sheppard, A. P., 2013. X-ray imaging and analysis techniques for quantifying pore-scale structure and processes in subsurface porous medium systems. *Advances in Water Resources*, 51, 217-246.

References

Youssef, S., Bauer, D., S, B., Rosenberg, E. and O, V., 2010. 3D In-Situ Fluid Distribution Imaging at the Pore Scale as a New Tool For Multiphase Flow Studies. *SPE Annual Technical Conference and Exhibition*. Florence, Italy.